CONTROLLING OPTICAL TRANSPORT IN LUMINESCENT SOLAR CONCENTRATORS

A THESIS SUBMITTED TO THE FACULTY OF THE UNIVERSITY OF MINNESOTA BY

Ryan Louis Connell

IN PARTIAL FULFILLMENT OF THE REQUIREMENTS FOR THE DEGREE OF DOCTOR OF PHILOSOPHY

Vivian E. Ferry, Advisor

May, 2019

© Ryan Louis Connell 2019

Acknowledgements

During my graduate work at the University of Minnesota I have been fortunate to receive support and guidance from a number of faculty, staff, and students. I am grateful for the opportunity that the U has provided to work with and learn from world-class colleagues.

First, I would like to thank my advisor Vivian Ferry. Her drive, passion, and inquisitive nature provide a terrific model for an effective scientist. Vivian's support and scientific vision have not only been instrumental for my work, but also for growing the Ferry group from just the three of us to an amazing group of researchers. In addition, I am also grateful for the support and guidance from our collaborators Uwe Kortshagen, Marc Hillmyer, and Lorraine Francis. I would also like to thank Dave Flannigan, Uwe Kortshagen, and Lorraine Francis for their guidance as committee members for my doctoral final exam.

I have been very fortunate to work with an impressive group of graduate students in the Ferry, Hillmyer, and Kortshagen groups. I would like to especially thank Samantha Hill for her collaboration, scientific discussions, and fabrication of Si/polymer composites for our Si LSC project as well as the DOW sustainability challenge. I would also like to thank Colin Peterson for support and discussions about polymer composites. In the Ferry group I would like to thank Dana Dement for her assistance with the ellipsometry modeling used in this work as well as her support as a fellow first student. I am grateful that for the past six years I have been able to turn around and have a conversation about research or a new graduate school deadline that one of us has found in order to make sure that we are both progressing to our goals. I would also like to thank Mayank Puri for his synthetic chemistry help and synthesis of the quantum dots used in this work as well as John Keil and Christian Pinnell for their help in the modeling and characterization of LSCs. In addition, I am grateful to Matt Quan for his training in steady-state and time-resolved photoluminescence as well as monthly trips to taste the new burger of the month and Ian Slauch for his calculation of solar flux in Minneapolis. I have also been fortunate to work

with and mentor a number of promising undergraduate researchers such as Willa Mihalyi-Koch and Will Broomhead, who worked with quantum dot synthesis, and Sydney Jones, who worked on fabricating titania films for nanophotonic stacks. While these members of the Ferry group have directly impacted the work in this thesis, I am grateful to all of the members of the Ferry group including Pavlos Pachidis, Bryan Cote, Eleanor Mayes, John Caputo, Sihoon Moon, Jessica Chiu, Katie Vlasic, Ben Jones, Karsten Poulsen, and Shahrzod Latifi for their feedback during presentations and scientific discussions.

At the University of Minnesota I have also used many of the research facilities on campus. I would like to acknowledge the Characterization Facility for ellipsometry characterization, the Minnesota Nano Center for spin coating and profilometry, and the Minnesota Supercomputing Institute for computational resources. In addition, I would like to thank the wonderful staff in the CEMS department especially Julie Prince and Teresa Bredahl for guidance through the administrative hurdles during the graduate school process.

I am also very grateful for the support and encouragement from my family and friends in Minnesota and throughout the country. I have been very fortunate to have strong group of friends in the cities that are capable of helping with research or bringing by a board game and recharging for it. I would also like to thank my mom, dad, and my sisters, Jordan and Sarah for their love, support, and encouragement during this process and all of the steps that lead up to now. In addition, I would like to thank my extended family for their love and hospitality during holidays even if they had to watch me write half of the time. Finally, I would also like to thank my new family, Christie and Mac, Tom and Suzanne, Amanda, Rhiannon and Rhindee, who have accepted me as their own and provided great times in Chicago, Port A, Austin, and San Antonio.

Last but not least I am grateful for the love, support, and encouragement provided by my wife Erica during this time. I am thankful for her cheerleading, pep talks, and desire to find adventures to recharge, which has enriched the graduate school process.

Abstract

Luminescent solar concentrators (LSCs) improve solar cell performance by transforming the spectrally broad and partially diffuse solar spectrum into a spectrally narrow and focused light source, which is then concentrated onto a small-area solar cell. However, LSCs do not currently reach their full concentrating potential due to losses in the system that prevent luminescent light from reaching the edge of the concentrator, including light scattering and coupling to the escape cone.

In order to reduce escape cone losses within LSCs, nanophotonic structures were designed for concentrators with CdSe/CdS core/shell nanocrystals. Using a combination of Monte Carlo ray-tracing simulations and FDTD simulations we show that concentration factor improvements of 3.7 times the standard concentrator are achievable when spectrally-selective mirrors are placed on top of the LSC. Further enhancements to the optical efficiency are possible when the emitted light is controlled either by a phase gradient metasurface or the directional emission of a nanophotonic stack of alternating high and low refractive index layers. Finally, we show that directional emission is also expected for a nanoscale thin film LSC on glass, which can also be fabricated by embedding CdSe/CdS in poly (cyclohexylethylene), a new polymer for LSC applications.

To reduce scattering losses for LSCs, new surface ligands have been proposed for Si nanocrystals that improve dispersion in polymer matrices. In this collaboration, I characterized Si/poly (methyl methacrylate) composites and showed that the scattering losses are reduced by six fold using these new surface ligands when compared to previous methods.

The design criteria established in this work demonstrate that nanophotonic structures can control the optical transport in LSCs, and that low scattering quantum dot/polymer composites are essential to realize high performance. The ability to control the light guiding properties in LSCs is crucial for high quality LSCs and future commercial implementation.

Contents

List of Figures

List of Tables

Chapter 1

Introduction

1.1 Motivation

Solar energy is currently experiencing a boom in implementation in the United States. It is estimated that 10.6 gigawatts of solar capacity was installed in 2018 bringing the total solar capacity installed in the US to 64.2 GW [3]. However, even with this dramatic increase in capacity, solar energy still only produces approximately 2% of the total electricity generated in the United States. Further deployment of solar harvesting technology can be realized with designs that reduce the cost to performance ratio, and allow for installation in non-traditional areas such as cloudy locations or the vertical facades of buildings.

One of the challenges to improving the cost to performance ratio of solar energy conversion is inherent to sunlight: 3 - 5% of the incident solar spectrum consists of ultraviolet radiation that is not converted efficiently by the solar cell, and between 15 and 100% of the sunlight is diffuse (Figure 1.1), meaning that it hits the solar cell at all angles of incidence. As the incidence angle of sunlight increases more of the light is reflected off of the top surface of the solar cell and not converted to electricity. Therefore, broadband and broad angle solar illumination places significant constraints on solar cell design, performance, and installation. For example, a photovoltaic panel would not efficiently convert incident solar energy when installed on the side of a building without a device that tracks the position of the sun.

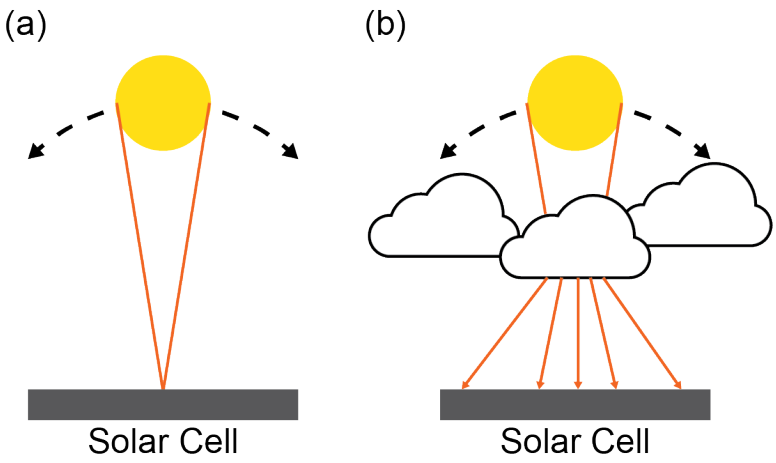

Figure 1.1: Schematic of direct (a) and diffuse (b) solar radiation

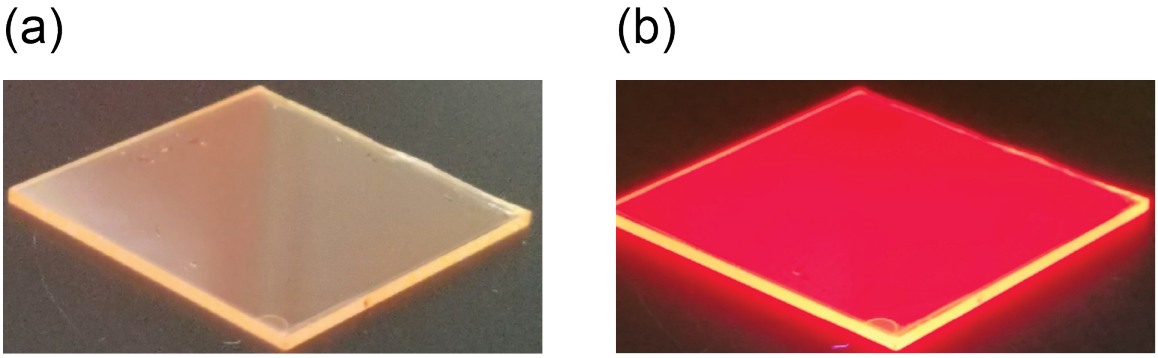

Figure 1.2: Photograph of LSC under visible (a) and ultraviolet (b) illumination.

Luminescent solar concentrators (LSCs) are an alternative solar cell concept that addresses these challenges. LSCs transform the spectrally broad and diffuse solar spectrum into a spectrally narrow and focused light source that couples sunlight onto a small solar cell [4–10]. In this way, the LSC collects sunlight over many wavelengths and more incident angles due to the lower refractive index of the LSC compared to the solar cell. However, the solar cell only has to operate over a restricted range of colors and angles, thereby increasing the conversion efficiency [11, 12]. A photograph of the light guiding properties of LSCs is shown in Figure 1.2.

The LSC consists of a polymer matrix with an embedded luminophore typically fabricated as a bulk composite [13,14] or a thin film on glass [15,16]. The luminophore absorbs

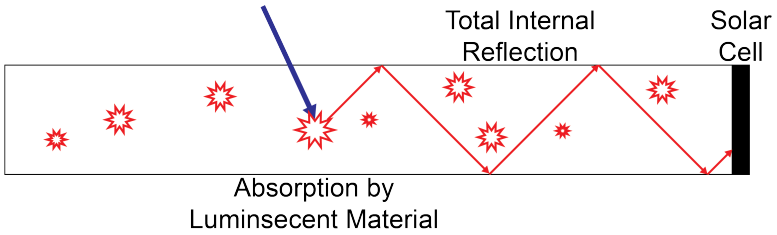

Figure 1.3: Schematic luminescent solar concentrator operation.

incident sunlight and subsequently emits light at a longer wavelength. This luminescent light propagates through the waveguide via total internal reflection to an edge-mounted solar cell. A schematic of the mechanism of light concentration for a LSC is shown in Figure 1.3. The LSC holds many advantages over traditional photovoltaic panels, including colorful and transparent form factors for building integrated photovoltaics and operation under both direct and diffuse illumination conditions [17, 18]. Although LSCs have been studied for many years, recent performance advances have been largely driven by the development of new and tunable luminescent materials [1, 13, 14, 19–27].

The geometry of a LSC allows for the collection of sunlight over a large area, but only uses the small area on the edge for solar conversion to electricity. This significantly decreases cost, as the polymer waveguide is much less expensive to manufacture than the solar cell semiconductor. In addition to decreasing cost, the LSC also increases performance of the solar cell, as the light interacting with the solar cell has an intensity greater than incident sunlight. This leads to an increase in short circuit current density and open circuit voltage, which increases the total power that can be extracted from the solar cell [28].

1.2 LSC Impact

1.2.1 Solar Cell Performance

Luminescent solar concentrators increase the flux on the solar cell through absorption and re-emission of incident sunlight into a polymer waveguide. The increased solar cell flux increases the short circuit current density as a larger number of photons are incident on the solar cell as compared to the flux it would observe normally. Along with an increase in short circuit density the open circuit voltage is increased [29].

$$V'_{OC} = V_{OC} + \frac{nkT}{q}\ln X$$

In this equation V_{OC} is the open circuit voltage, n is an ideality factor corresponding to the main type of recombination in the solar cell, and $\frac{kT}{q}$ is the thermal voltage. The thermal voltage is made up of k, Planck's constant, T, the temperature of the cell, and q, the elementary charge. Finally X is the concentration factor. Therefore, as the concentration factor is increased the short circuit current density and the open circuit voltage will be increased, which will also increase the maximum power that can be extracted from the solar cell [29].

$$P_{max} = V_{OC} I_{SC} FF$$

In the above equation P_{max} is the maximum power that outputted from the cell, I_{SC} is the short circuit current, and FF is the fill factor, which is a factor that accounts for how much of the theoretical maximum power is extractable in a given solar cell. This increase in P_{max} also allows for an improvement in the overall solar efficiency η [30].

$$\eta = \frac{V_{OC} I_{SC} FF}{P_{in}}$$

Where P_{in} is the power put into the solar cell. This increase in efficiency does not break the limits defined for a single junction solar cell by Shockley-Queisser as concentration of incident sunlight is a term used in their initial calculation [30]. The efficiency limit of a single junction solar cell increases to 40% for a 45,900 concentration factor [31].

Along with concentrating the incident light onto the solar cell mounted at the edge. LSCs also downshift the incident solar spectrum into a light source that can be absorbed by the solar cell with reduced thermalization losses [32]. These thermalization losses usually contribute to heat in the solar cell, which reduces overall efficiency through the following equation [33].

$$\eta = \eta_0 \cdot \big(1 + \beta\,(T - T_0)\big)$$

Where η is the efficiency of the solar cell, η_0 is the initial efficiency at a given temperature, and β is constant dependent on the solar cell material. For crystalline silicon solar cells β is approximately $-0.4\%\frac{1}{K}$. Finally T and T_0 are the current and initial cell temperatures respectively. For example, a back-of-the-envelope calculation shows that using Si as a luminophore in a luminescent solar concentrator will significantly modify the spectral characteristic of the light shining on the solar cell to better match the spectral response of the silicon solar cell. This modification, seen in Figure 1.4, is predicted to improve the solar cell efficiency by 33% due to the improved spectral matching and reduced thermalization losses [34].

1.2.2 Harvesting Sunlight from Vertical Facades

Traditional solar cell modules are opaque slabs that are best suited for installation in large solar fields or on roofs of commercial and residential buildings. While, this is useful for large scale distributed power systems, this may be a major issue for onsite and integrated power collection. Many onsite power collection applications have aesthetic or size

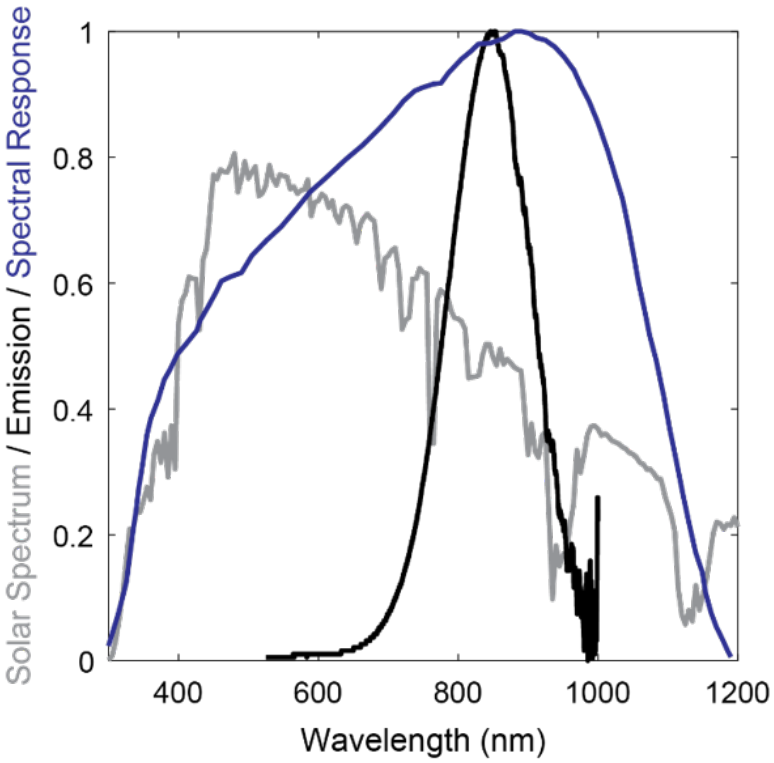

Figure 1.4: Utilizing Si luminescent nanocrystals modifies the light source on the silicon solar cell from the incident solar spectrum (gray) to the emitted light from the Si nanocrystals (black), which better matches the spectral response of the silicon solar cell (blue).

constraints that make traditional solar panels undesirable for the design [35–39].

Of these onsite applications, developing technologies that can be integrated into new and existing building materials would produce the greatest amount of energy and increase the likelihood of widespread solar adoption. If solar harvesting designs can be created using translucent or transparent materials then building-integrated photovoltaic (BIPV) technologies can be utilized in more than just rooftop installations. For buildings of even a modest height, this will increase the solar harvesting area without dedicating any extra land. This would be especially attractive for urban areas as much of the land is dominated by tall buildings with small roof areas, but large facade areas. In order to implement solar harvesting technology on the vertical facades of building we must have a design that has tunable transparency as windows cover a significant fraction of the sides.

LSCs would have a large impact in this application as the separation of incident light

absorption and electron-hole pair generation means that the doped polymer can be used as the visibly transparent sunlight harvester while the solar cells can be mounted in the window sills to produce electricity. With a judicious choice of luminophore the transparency of the window harvester can be tuned in order to effectively produce electricity without blocking resident's views.

As a case study, a series of back-of-the-envelope calculations were performed for LSCs using Si NCs as these non-toxic nanocrystals have an absorption spectrum well-suited for a visibly transparent harvester. Even in the modest case where the LSC only guides 3% of the incident light due to a non-unity quantum yield, a window with a visible transparency of 65% can produce 5.5 kWh/m^2 per year, enough to power a light bulb by itself. However, if optical and synthetic techniques are used to improve the quantum efficiency of the nanoparticle and trap the emitted light then a power output up to 47 kWh/m^2 could be achieved in this design. A schematic of these different window scale concentrators are shown in Figure 1.5.

This could have a large impact on energy consumption needs in the US as if these windows were used to cover the vertical areas of commercial buildings in the US, then the energy produced would be enough to power up to 12 million homes and reduce CO_2 production by 3.6% from electricity generation [40].

1.2.3 Thermodynamic Concentration Factor Limit

LSCs have the capability to usher in a new era of cheap concentrated photovoltaic technology. In the thermodynamic limit the concentration of a LSC depends on the Stokes shift of the luminophore, which is the difference in energy between the maxima of the absorption and emission spectra. This relationship means that LSCs have the capability to achieve higher concentration factors than even current direct concentrating technology [8].

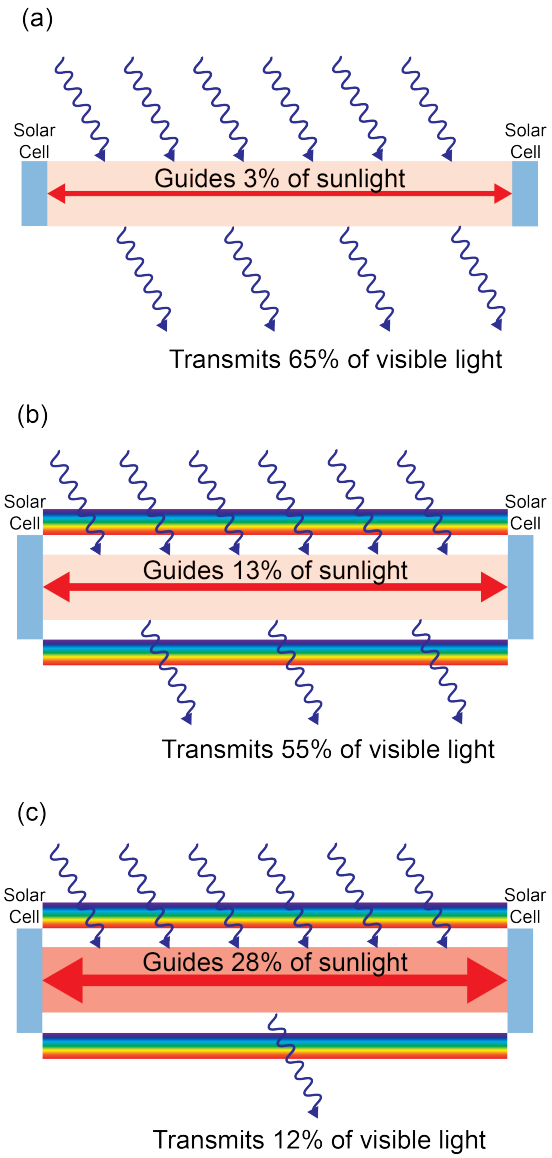

Figure 1.5: Schematic demonstrating the light guiding and visible transparency predicted for our current best Si LSC (a) without optical designs to improve performance. (b) shows the improvement to light guiding predicted by improving the quantum yield of the luminophore and adding nanophotonic designs to improve trapping. (c) predicts the further increase in power that can be gained by increasing the loading fraction of the luminophores in the LSC.

$$C = \frac{\nu_2^2}{\nu_1^2} e^{\frac{h(\nu_1 - \nu_2)}{KT}}$$

In this equation C is the concentration factor, ν_1 and ν_2 are the frequency of absorption and emission respectively, T is temperature, h is Planck's constant, and K is Boltzmann's

constant. As seen in this equation large concentration factors are achievable if the incident sunlight is sufficiently downshifted by the luminophore. However, to date best concentration factors are limited to approximately 30x due to the loss mechanisms in the system, which will be discussed in further detail in Section 1.5.

1.3 Components of LSC Operation

1.3.1 Absorption and Emission by Luminophores

Incident sunlight that reaches the luminescent volume of the LSC may be absorbed by the luminophores embedded within the polymer matrix. The fraction of light that is absorbed by the luminophores depends on the absorption spectrum of the luminophores chosen and the loading fraction within the polymer composite. More detail on luminophores used in LSCs will be given in Chapter 2. Quantitatively the fraction of light absorbed by the luminescent volume is given by Beer's law [41].

$$A(\lambda) = 1 - e^{-\epsilon(\lambda)tc}$$

Where $\epsilon(\lambda)$ is the absorptivity of the luminophore, c is the concentration of the luminophore within the polymer, and t is the thickness of the luminescent layer.

If the light is absorbed by the luminophore it promotes electrons in the ground state of the luminophore into one of excited states. Electrons in this excited state can then relax to the lowest level of the excited state after which they relax to the ground state either through a radiative transition, which produces a photon at a longer wavelength than the photon absorbed or through a non-radiative transition due to possible defects in the material [42, 43].

Light that is emitted from the luminophore is emitted isotropically. Therefore, a portion of the emitted light escapes out the top or the bottom face of the LSC, but a majority of it

is trapped within the polymer waveguide due to total internal reflection. The expected light trapped by total internal reflection is dependent on the refractive index of the waveguide [44].

$$F_{TIR} = \cos \sin^{-1} \left(\frac{1}{n} \right)$$

1.3.2 Interaction with Waveguide Interfaces

Light that is emitted into the total internal reflection modes has a unity coefficient of reflection when it interacts with the polymer/air interfaces of the waveguide. In this way, all the incoming light is reflected back into the waveguide and continues to propagate towards the solar cell. For light that is not emitted into the total internal reflection modes a fraction of the incoming light is refracted into air and a fraction is reflected back into the waveguide. These fractions are calculated using Fresnel equations.

$$R_s = \left| \frac{n_1 \cos \theta_i - n_2 \cos \theta_t}{n_1 \cos \theta_i + n_2 \cos \theta_t} \right|^2$$

$$R_p = \left| \frac{n_1 \cos \theta_t - n_2 \cos \theta_i}{n_1 \cos \theta_t + n_2 \cos \theta_i} \right|^2$$

In these equations, n_1 and n_2 are the refractive indices of the old and new media respectively, θ_i is the angle that the incident ray makes relative to the normal of the interface, and θ_t is the angle that the transmitted ray makes relative to the normal of the interface. This is calculated using Snells law [45].

$$n_1 \sin \theta_i = n_2 \sin \theta_2$$

1.3.3 Interaction with Mirrors

Sometimes mirrors are placed on the non-solar cell interfaces of the LSC in order to better trap light within the concentrator. In addition, a diffuse mirror is commonly placed on the back side of the mirror with an air gap between the LSC and mirror. The diffuse mirror scatters incident light back towards the LSC with a Lambertian angular distribution, such that the surface has an equal radiance as a function of observer angle. The radiance in this case at is equal to [46]

$$I_0 = \frac{I d\Omega dA}{d\Omega_0 dA_0} \text{photons/(s m}^2 \text{ sr)}$$

where $d\Omega$ is an arbitrarily chosen range of solid angles, dA is an area element, dA_0 is the observing aperture, which subtends a solid angle $d\Omega_0$. Finally I is the radiance and I_0 is the observed radiance at a given viewing angle. At a non-normal incidence the photons emitted into a range of solid angles $d\Omega$ will be equal to $I\cos(\theta)d\Omega dA$. Therefore, the radiance observed at a non-normal angle of incidence will be equal to:

$$I_0 = \frac{I\cos(\theta)d\Omega dA}{d\Omega_0\cos(\theta)dA_0} = \frac{I d\Omega dA}{d\Omega_0 dA_0}$$

which is equal to the radiance of the observer at normal incidence.

The incorporation of a diffuse scatterer on the back of a LSC has multiple effects on light concentration. The incident light will be scattered into a Lambertian angular distribution, which will increase the path length within the luminescent volume. This will increase the likelihood that the incident sunlight will be absorbed by the LSC, which will subsequently increase the fraction of incident light that is eventually collected by the solar cell. There is also a small fraction of both incident light and emitted light that will be directly scattered into the solar cell. However, based on the angular distribution of the mirror there is an equal likelihood that emitted light that would reach the solar cell if a specular mir-

ror was placed on the bottom is scattered out of the LSC. In most LSCs the scattering of emitted light into the solar cell and out of the LSC cancels out, but the direct scattering of incident light has been observed to slightly improve light collection for small area LSCs.

For the bottom surface mirror as well as any other mirrors that are desired an air gap between the LSC and the mirror is required for optimum performance [47]. Most mirrors do not have perfect reflectance of incident light. A portion of the light is absorbed and lost to heat. If the mirrors are placed directly onto the surface of the LSC then they will reflect and absorb light that is in the total internal reflection modes as well as light that would escape the LSC. On the other hand, total internal reflection perfectly reflects light without losses to absorption. Therefore, if an air gap is placed between the LSC and the mirror then total internal reflection will perfectly reflect light trapped within the LSC and the mirrors will reflect only the light that was going to escape the concentrator already, improving overall performance.

The air gap between the LSC and the mirror should be as small as feasible as it is possible for light to escape out of the side of the LSC, reflect off of the mirror, and not return to the LSC if the trajectory in the z direction takes the photon out of the LSC. Mathematically this can be seen by the following equation derived from the geometry of the air gap.

$$T_z = \frac{2t_a\nu_z}{\nu_{x,y}}$$

In this equation ν is the normalized velocity of the photon, t_a is the thickness of the air gap, and T_z is the translation of the photon in z. Therefore, there are a range of locations where the photon can exit the LSCs, based on the thickness of the air gap, where the translation in z of the photon will lead to the photon returning above the top interface of the LSC and escaping. Because of this, it is important to reduce the size of the air gap when possible in order to improve LSC light trapping.

1.4 LSC Performance Metrics

The performance of a LSC is often characterized by its concentration factor or the ratio of the emitted flux onto the solar cell and the sunlight flux onto the top face of the LSC [44].

$$C = \frac{\Phi_{SC}}{\Phi_{LSC}} = G\eta_{opt}$$

Where C is concentration factor, Φ_{SC} is emitted flux on the solar cell, and Φ_{LSC} is incident solar flux onto the top face of the LSC. This can also be written as the product of the geometric ratio, G, and the optical efficiency, η_{opt}. G is the ratio of the solar cell and LSC top face areas and η_{opt} is the fraction of incident photons that reach the solar cell. The optical efficiency can be further broken down as the efficiency of step in the concentration process [44].

$$\eta_{opt} = \eta_{abs}\eta_{QY}\eta_{trap}\eta_{wg}$$

η_{abs} is the absorption efficiency of the LSC or the fraction of the incident light that is absorbed by the luminophores. η_{QY} is the emission efficiency or the fraction of absorbed light that is emitted radiatively. η_{trap} is the fraction of emitted light trapped by total internal reflection. η_{wg} is the fraction of emitted light that reaches the solar cell.

1.5 LSC Losses

While LSCs have the potential to inexpensively improve solar cell performance and utilization, a number of loss mechanisms keep them from fulfilling that potential. The common loss mechanisms that limit the concentration factor of LSCs are shown in Figure 1.6. Losses due to non-unity quantum yield arise when luminophores in a LSC do not emit every photon that is absorbed. This can occur due to defects in the material, interaction

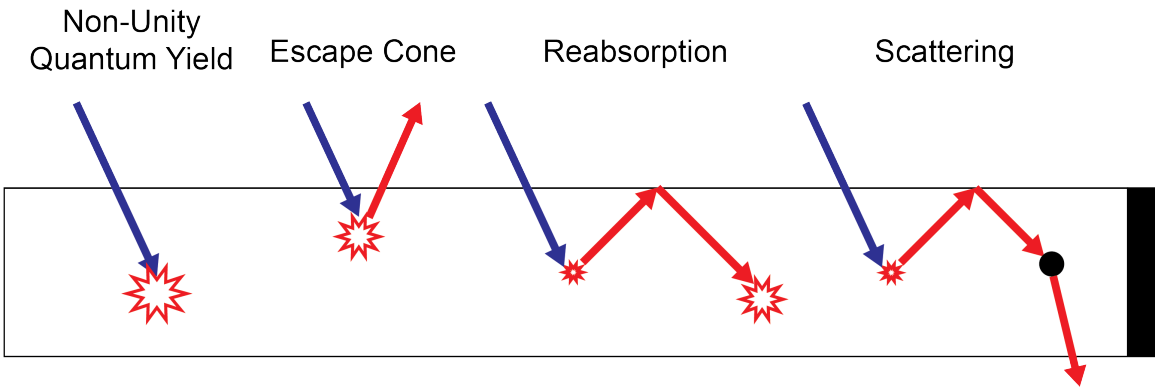

Figure 1.6: Schematic of common LSC loss mechanisms.

of the carriers with the surface of the luminophore, or transfer of energy to another nearby particle [48]. These non-radiative transitions will decrease the quantum yield, or emission efficiency, of the particle and can lead to significant losses in the concentrator.

Escape cone losses occur when the luminophore emits light that travels out of the top or bottom face. The emission of light into an isotropic distribution is what allows for the light guiding process within the LSC, but only a faction of the emitted light will be at an angle that will be trapped by total internal reflection. The angle with respect to the top face of the LSC is shown in Figure 1.7. In most polymer systems where the refractive index of the waveguide is approximately 1.5, the critical angle of total internal reflection is approximately 43°. This will trap 74% of the emitted light within the waveguide after each emission event, but 26% of the emitted light will escape out of the top and bottom face.

Reabsorption losses are defined as incident sunlight that is absorbed and emitted by a luminophore, but then absorbed by another luminophore and lost through a non-radiative transition [49, 50]. This loss mechanism is not only mediated by the non-unity quantum yield of the luminophore but also by the overlap between the absorption and emission spectra. While reabsorption losses are specifically defined as the non-radiative loss of the reabsorbed light, reabsorption affects escape cone losses as well. If the reabsorbed light is successfully re-emitted then the emission angle is once again randomized within the isotropic distribution. This means that only 74% of the reabsorbed and re-emitted light will

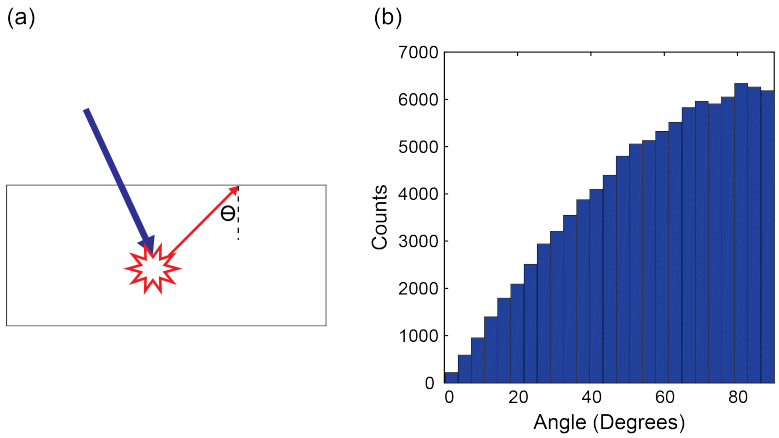

Figure 1.7: (a) Schematic showing angle that emitted photons make with top face. (b) Histogram of angle with respect to the top face of the concentrator for 100,000 isotropically emitted photons.

be trapped within the waveguide. This is particularly detrimental for LSC performance as reabsorption of emitted light will more preferentially occur for light that is trapped within the waveguide as it will take a longer path through the luminophore composite. Therefore, reabsorption decreases LSC performance not only through non-radiative relaxation, but also randomization of waveguided photons.

Finally scattering losses occur when light trapped within the waveguide scatters off of a luminophore or defect in the polymer waveguide [51, 52]. Similarly to the process of reabsorption and re-emission, scattering will randomize the direction of the trapped light. This will increase the chance that the light will escape out of the top or bottom of the LSC before it reaches the solar cells on the edge.

In the following chapters we will focus on a number of nanophotonic designs in order to reduce the escape cone losses of LSCs. However, through our simulation methods we will also explore and track the impact that these designs have on all of the different loss mechanisms. In our experimental work we will explore how the surface of the luminophore and its interaction with the polymer matrix affects the scattering losses within the concentrator.

1.6 Nanophotonic Designs for LSCs

Photonic designs have been proposed and experimentally fabricated to trap emitted light and control the angular profile of emission, which may significantly decrease escape cone losses. These photonic designs can be thought of as an optical analog to a semiconductor or crystal lattice. Instead of atoms or molecules inhabiting each lattice site, materials of different dielectric constant are arranged in a periodic pattern yielding a periodic dielectric function. Much like a crystal lattice, photonic designs can also be designed to have a photonic band gap, which prevents light of specific wavelengths from passing through the crystal [53]. In this way it is possible to design a photonic mirror that allows light into the concentrator to be absorbed by the luminophore but reflects the emitted light that would travel into the the escape cone.

One of the most common photonic designs is the 1D crystal or Bragg stack in which layers of different dielectric constants are stacked in a periodic pattern. This design has been used in multiple experiments and simulations as a photonic band stop filter on top of an existing solar concentrator [17, 54–57]. A simple schematic of this set up is shown in Figure 1.8. One downside of these photonic designs is that the spectral region of high reflectivity shifts blue as a function of incidence angle, which requires careful design of the photonic band gap [58] in order to effectively reflect all of the emitted light in the escape cone. 3D crystals have also been proposed with applications to LSCs. Utilizing a 3D crystal, Goldschmidt et al. as well as Joannopoulos et al. predicted that with a diamond structured photonic crystal, the reflection of structure does not change significantly with angle of incidence unlike the 1D Bragg stack design. This increases the light guiding of the structure allowing for more of the quantum dot emission to fall into the reflection conditions of the photonic design [53, 54].

In addition to the use of top mirrors to trap the emitted light within the concentrator

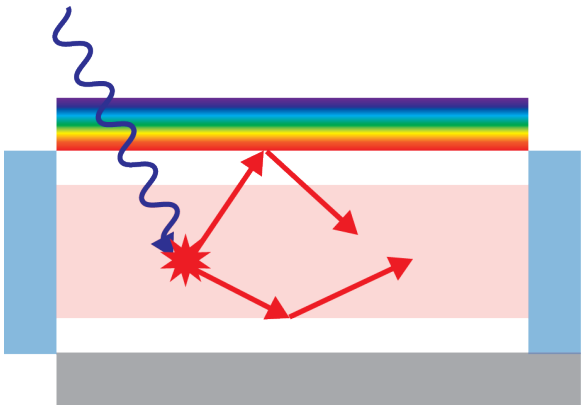

Figure 1.8: Schematic of trapping mechanism for photonic band stop filter.

LSCs have been embedded in the geometry of 1D photonic designs. These "photonic" LSCs modify the local photonic density of states surrounding the luminophores, which affect the radiative rates of emission as well as the angular distribution [59, 60]. This has been shown to improve the light guiding capabilities of the LSC as well as reduce reabsorption losses [2, 61].

1.7 Thesis Outline

This thesis will cover the design, simulation, fabrication, and characterization of LSCs as well as nanophotonic designs to control the optical transport to improve performance. Chapter 2 will focus on the different luminophores for LSCs and provide more detail on the specific quantum dots that were used in this work. Chapter 3 will provide details on the two algorithms that are used to simulate the results in the first half of this thesis. Then Chapters 4, 5, and 6 will discuss the nanophotonic designs that have been designed and simulated to improve the concentration factor of LSCs. Chapter 4 will discuss work performed to design spectrally selective top mirrors and explain how the design is affected by different LSC properties. Chapter 5 will then compare how spectrally selective mirrors affect the performance of the concentrator when compared to other designs such as a phase-shifting metasurface placed on the back surface of the LSC and a theoretical design that forces all

emission into the total internal reflection angles. Finally Chapter 6 will show design and simulation work that has been done to modify the angular distribution of emission from the luminophores to achieve highly directional emission into total internal reflection modes.

The second part of this thesis will then focus on experimentally fabricated LSCs using both Si and CdSe/CdS core/shell quantum dots. Chapter 7 will present progress in fabricating nanoscale CdSe/CdS polymer composite thin films using a new polymer, poly (cyclohexylethylene). Then Chapter 8 shows how modifying the surface functionalization of the Si quantum dot with ligands that better match the repeat unit of the poly(methyl methacrylate) (PMMA) matrix will produce QD/PMMA composites with significantly less scattering over a wide range of quantum dot loading fractions.

Chapter 2

Luminophores for Luminescent Solar Concentrators

2.1 Introduction

As discussed in Section 1.3.1 luminophores absorb incident sunlight and emit that light into the waveguide to be collected by the solar cell. Therefore, a high quality luminophore is crucial for fabricating a LSC that effectively guides incident sunlight. The ideal luminophore has unity quantum yield such that all of absorbed photons are emitted into the waveguide. It has no overlap between the absorption and emission spectra, which eliminates the likelihood that emitted light within the waveguide is reabsorbed by another luminophore. The emission from the luminophore should match with the spectral conversion efficiency of the solar cell, which will eliminate losses due to thermalization in the electricity generation process. It should also have perfect absorption over the rest of the solar spectrum so that all incident light is absorbed and emitted into the waveguide. Finally, the perfect luminophore's optical properties should not change under exposure to UV, air, water, or weathering. However, in practice, there are no ideal luminophores that meet all of these criteria. In this chapter, different luminophores used in LSC designs will be discussed and compared to the ideal luminophore.

2.2 Dyes

LSC designs have used organic dyes due to their high solubility in polymer matrices, high quantum yield, and large absorption efficiency. Unfortunately they also have a low absorption range [62], have a decreased quantum yield for emission where silicon solar cells absorb most efficiently [63], and undergo photodegredation when exposed to sunlight for long periods of time [64]. Under UV illumination the dyes can undergo photoreduction or photooxidation, which will create a nonradiative cation or anion respectively and quench fluorescence. Even if the fluorescence is not quenched completely under UV illumination the spectral properties can blue-shift and the fluorescence can be reduced [65]. Significant improvements in the photostability of dyes have been made using the Lumogen series of dyes, which have found application in many LSCs [54, 56, 66–68], but they still begin the process of degradation after 80 days and require significant fabrications controls so that they do not interact with contaminants that quench fluorescence [69].

2.3 Quantum Dots

Luminescent quantum dots are semiconducting nanoparticles with a particle size that is on the order of the de Broglie wavelength of the electron [17]. These quantum confined particles exhibit unique optical and electrical properties not found in bulk semiconductors due to a change in the band structure at this small size. Figure 2.1 shows the band structure of a bulk semiconductor, a quantum dot, and a molecule. The discrete energy levels in the quantum dot band structure allow for absorption and emission processes that resemble the fluorescent dyes discussed in Section 2.2.

Quantum dots have many beneficial properties that make them advantageous for LSC applications. Quantum dots, in general, have well-established synthesis methods, high quantum yield, broad absorption, large absorption cross sections, absorption and emission

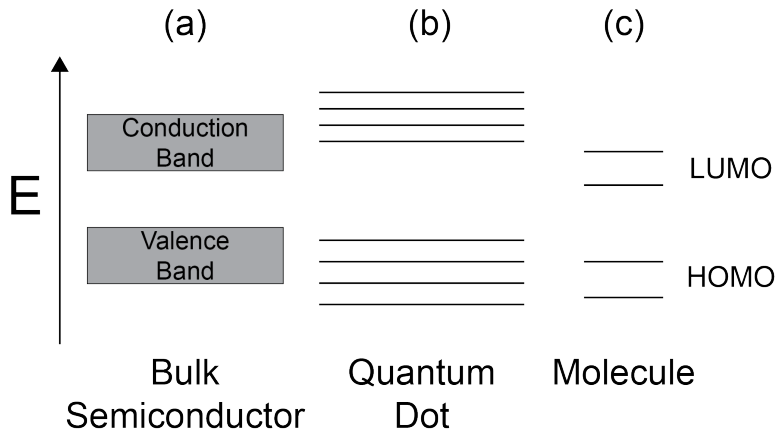

Figure 2.1: Band structure of bulk semiconductor (a), quantum dot (b), and molecule (c)

spectra that are tunable based on the size, and improved photostability compared to organic dyes [70, 71]. However, they are still susceptible to non-radiative losses due to surface trap states and incorporation into the polymer matrix. In order to reduce these losses, some quantum dots are passivated with a semiconductor shell, which can improve fluorescence as well as further tune the absorption and emission properties of the quantum dot [72–77]. This shell is often produced using a successive ionic layer adsorption reaction (SILAR), which allows for synthesis of QDs with very large shells that can be controlled in monolayer steps [78]. However, as the QD shell increases the scattering cross section of the particles also increases, which will be detrimental for LSC performance. Therefore, it is often important to balance the benefits gained by shelling the QD material with the increase in scattering of larger particles.

Many different quantum dots have been utilized to fabricate LSCs. These are summarized in Table 2.1 with their relevant properties. In this work luminescent solar concentrators are simulated and fabricated using CdSe/CdS core-shell quantum dots as well as Si quantum dots. Sections 2.3.1 and 2.3.2 give a brief description on each of the QDs.

Quantum Dot	Absorption Range (nm)	Quantum Yield	FWHM (nm)	Emission Range (nm)
CdSe/CdS [79]	400 - 600	99%	30	550 - 650
Si (Plasma) [14]	400 - 950	50%	140	700 - 1000
Si (Colloidal) [80]	300 - 550	90%	40	525 - 650
CuInSeS/ZnS [13, 81]	400 - 950	73%	215	750 - 1200
$CuInS_2$/ZnS [82]	300 - 450	81%	140	450 - 750
Mo_6Cl_{12} or Br_{12} [83]	300 - 450	78%	175	600 - 900
$Zn_{1-x-y}Cd_xMn_ySe$/ZnS [20]	350 - 450	88%	100	550 - 700
PbS/CdS [84]	600 - 1000	70%	100	900 - 1000

Table 2.1: Summary of some of the QDs used in LSCs

2.3.1 CdSe/CdS Core-Shell Quantum Dots

CdSe/CdS quantum dots consist of a cadmium selenide semiconducting core and a cadmium sulfide shell. This forms a quantum dot heterostructure with a quasi-type II band alignment as seen in Figure 2.2 (c). This type of alignment is very attractive for the fabrication of large area LSCs as the holes are delocalized over the structure while the electrons are localized to the CdSe core. This means that the carriers are significantly less likely to leak to the surface as in a Type 2 alignment (Figure 2.2 (b)), which will reduce quantum yield and photostability [73, 74, 85]. Quasi-type II heterostrucutres also have a significantly larger Stokes shift than type I aligned heterostructures (Figure 2.2 (a)), as electrons and holes are confined in the core of the material for type 1 aligned bands [77, 78, 86]. CdSe/CdS quantum dots in particular have been synthesized with quantum yields up to 99% for thin shell heterostructures [79]. These quantum dots have also been synthesized with large Stokes shifts and low overlap between the absorption and emission spectra using up to 16 layers of CdS, which retain a quantum yield of 86% [24].

The thickness of the CdS shell also affects the spectral properties of the absorption and emission spectra. A visual representation of the change in absorption and emission is shown in Figure 2.3. As the thickness of the shell increases the absorption is dominated by the features of the CdS. This causes the absorption of higher energy light to increase

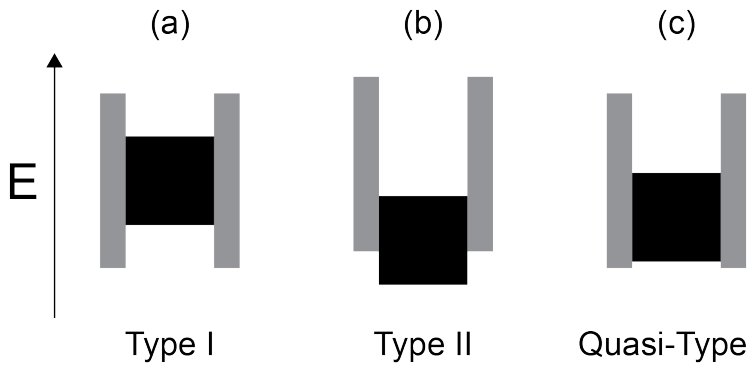

Figure 2.2: Schematic of bands for core/shell quantum dots with Type I (a), Type II (b), and Quasi-Type II(c) band alignments.

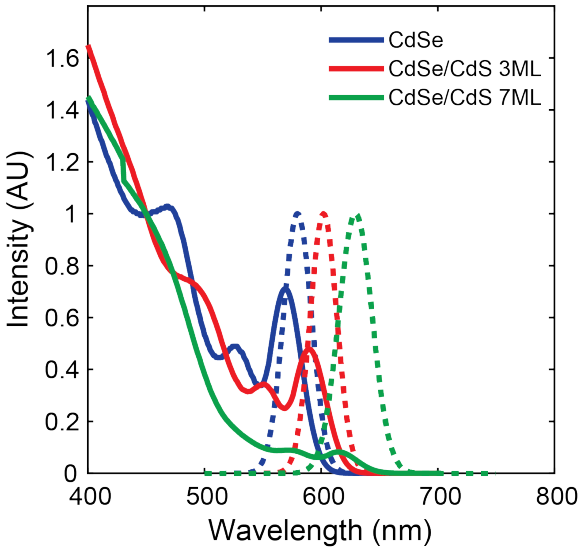

Figure 2.3: Absorption (solid) and emission (dashed) spectra for CdSe/CdS QDs with a 0 (blue), 3 (red), or 7 (green) monolayer shell.

relative to the absorption due to the CdSe excitonic features. In addition, the emission of the CdSe/CdS QD redshifts as the thickness of the CdS shell increases. Therefore, as the thickness of the shell increases the overlap between the absorption and emission spectra decreases due to these two factors. For this reason, we use CdSe/CdS core/shell with a 7 monolayer shell for most of the work in Chapters 4, 6, and 7.

The CdSe/CdS quantum dots used for these studies were synthesized by Mayank Puri following the synthesis procedures in [87, 88]. Briefly, 1-octadecene, cadmium myristate, and of selenium dioxide were added to a 3-neck round bottom flask and brought to a tem-

perature of 240 °C under nitrogen. This causes the mixture to change to a dark red color. After this color change oleic acid was added dropwise and held at a temperature of 240 °C for 30 minutes while the color of the solution became almost black. Then the reaction was brought to room temperature and the CdSe quantum were cleaned using a combination of centrifugation and filtering.

Then the shelling process was begun by determining the concentration and size of the CdSe cores. This was accomplished using a sizing curve in [89] and measuring the absorbance of the CdSe cores. This will return a volume required of the precursor CdSe solution to add 3×10^{-7} mol of CdSe to the shelling reaction. The precursor CdSe solution was made by adding the appropriate amount of CdSe quantum dots with dodecane and oleylamine and degassed. Then the CdS-precursor solution was prepared using a 4:1 molar mixture of $Cd(DDTC)_2$:$Cd(oleate)_2$.

To synthesize the shell the CdSe cores were heated to 80 °C, after which the appropriate volume of CdS-precursor for one monolayer was added to the vial. This appropriate amount was again calculated based on the size of the CdSe core and number of CdSe nanoparticles in the solution. After the CdS-precursor was added the temperature was brought to 160 °C for 20 minutes and then cooled back to 80 °C. Then the shelling procedure can be repeated for the number of monolayers required.

To improve the QY of the synthesized CdSe/CdS QDs the solution was bubbled with nitrogen for 15 minutes and an additional ”monolayer” of cadmium chloride was used to treat the surface. Following all of the surface treatments the CdSe/CdS core shell quantum dots were cleaned again using a combination of centrifugation and filtering. This synthesis process produced high quality quantum dots with a measured quantum yield of 77% and a low overlap between the absorption and emission spectrum.

2.3.2 Si Quantum Dots

Si quantum dots are also attractive for large area luminscent solar concentrator applications as they emit in the near-infrared, which is well matched to the silicon solar cell band gap [90] and they have a low overlap of the absorption and emission spectra due to their indirect character [14]. Si nanoparticles are still indirect semiconductors like their bulk counterparts, which means that the absorption spectrum of the Si quantum dots does not show excitonic features associated with specific transitions like seen in CdSe/CdS QDs. This significantly decreases the overlap between the absorption and emission spectra, which makes the Si quantum dots attractive for large area LSCs. Along with these optical properties, Si also has low toxicity and widespread elemental abundance, which make them attractive for BIPV applications [14, 35, 91–93]. The Si quantum dots characterized in Chapter 8 are synthesized by Samantha Hill following the procedure in [90].

Chapter 3

Modeling Methodology

3.1 Monte Carlo Algorithm

Monte Carlo models are commonly used to model LSCs and are an effective tool for tracing the path of photons within a LSC when the wave effects of light are negligible [94]. The Monte Carlo model used in this work is home-written to analyze each of the layers of the LSC separately and trace the path of the photon as it travels through these layers. This type of model operates by defining probability functions for the different possible interactions between the photon and the LSC geometry and then produces a random number at each interaction to determine the behavior of the photon. In this way, if multiple millions of photons are injected into the LSC then the average behavior can be determined without many of the assumptions required for analytical models.

Figure 3.1 gives an overview of the Monte Carlo ray-tracing algorithm that is used to model the LSCs in Chapters 4 and 5. The wavelength range of the simulation is set to match the wavelength range of the absorption spectrum. This model can be extended to model sunlight on the LSC by weighting the final results by the AM 1.5 solar spectrum. At each given position and wavelength, one photon is injected into the top face of the LSC structure with a normalized velocity. Next, the photon propagates through the LSC with a direction determined by the normalized velocity of the photon. While the photon propagates, the position is tracked to determine if it interacts with an element of the LSC

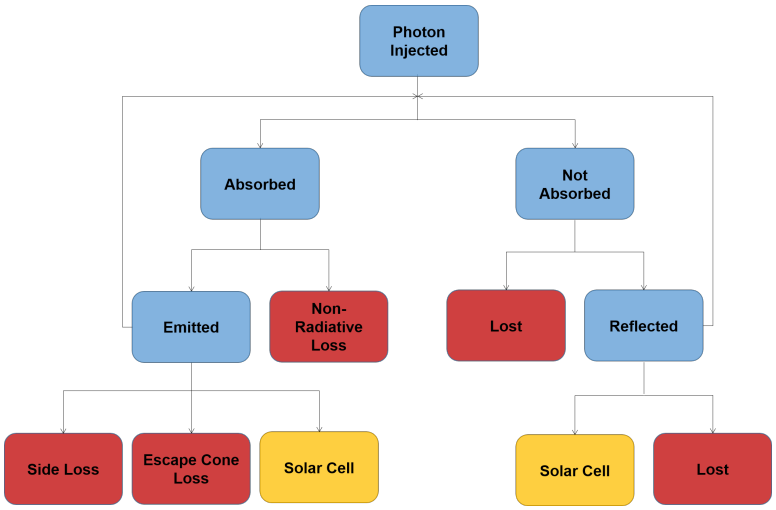

Figure 3.1: Schematic of Monte Carlo ray-tracing algorithm.

and which final collection mechanism it reaches. These elements include absorption in the luminescent layer, refraction from the interfaces between different layers, and reflection off of the mirrored surfaces.

To determine whether or not a photon is absorbed by the luminescent layer, a random number between zero and one is generated anytime the photon is located in the layer. This random number is compared to the transmission probability for the photon at its wavelength. If it is larger than the probability of transmission, the photon is absorbed by a luminophore at the photons current location. The probability of transmission is calculated using Beers law [41].

$$T(\lambda) = \frac{I}{I_0} = e^{-\epsilon(\lambda) l c}$$

Where $\epsilon(\lambda)$ is the absorptivity of the luminescent material, l is the length of the move step of the photon which has a default of 5μm, and c is the optical density of the quantum dots in the layer. The absorptivity of the luminophore is calculated by multiplying an experimentally measured absorption spectrum for the luminophore by a thickness factor to account for the difference between the solution measured absorption data and the performance of

the solid sample [57].

$$\epsilon(\lambda) = A(\lambda) f_T$$

Where $A(\lambda)$ is the absorption measured as a function of wavelength and f_T is the thickness factor

$$f_T = \frac{t_{UV}}{t_L A(\lambda_d)}$$

where t_{UV} is the thickness of the sample measured in the UV-Vis, t_L is the thickness of the LSC, and $A(\lambda_d)$ is the intensity of the absorption at the band edge of the luminophore.

After the photon is absorbed, the quantum yield is used to determine if the photon is emitted at a new wavelength or lost to a non-radiative pathway. If a random number generated by the code is greater than the quantum yield of the particle it is assumed to have relaxed through a non-radiative pathway. Otherwise, it has been emitted as a photon with a wavelength drawn from the emission data for the luminophore and given a new normalized velocity sampled from a constant spherical distribution to ensure isotropic emission. The quantum yield of a luminophore is defined as the ratio between the number of photons emitted from the particle and the total number of absorbed photons [95, 96].

$$QY = \frac{I_F}{I_A} = \frac{k_r}{k_r + k_{nr}}$$

Where k_r is the radiative rate constant and k_{nr} is the non-radiative rate constant, which are inversely related to the lifetimes of the radiative and non-radiative processes respectively. In this work the quantum yield is measured for the luminophores by dividing the integrated emission power by a well-known excitation power [97].

As the photon continues to propagate through the LSC, the position is monitored to determine when it passes an interface, interacts with a mirror, or is collected. To deter-

mine whether or not the photon has crossed through an interface the refractive index at the current position and previous position is monitored. When a change in refractive index is determined then it preforms calculations to determine which interface was crossed and applies Fresnel equations appropriately. Fresnel equations calculate the probability that a photon is transmitted or reflected for a given change in refractive index.

$$R_s = \left| \frac{n_1 \cos\theta_i - n_2 \cos\theta_t}{n_1 \cos\theta_i + n_2 \cos\theta_t} \right|^2$$

$$R_p = \left| \frac{n_1 \cos\theta_t - n_2 \cos\theta_i}{n_1 \cos\theta_t + n_2 \cos\theta_i} \right|^2$$

In these equations, n_1 and n_2 are the refractive indices of the old and new positions respectively, θ_i is the angle that the incident ray makes relative to the normal of the interface, and θ_t is the angle that the transmitted ray makes relative to the normal of the interface. This is calculated using Snells law [45].

$$n_1 \sin\theta_i = n_2 \sin\theta_2$$

If a calculation using Snells law produces a θ_t that is not defined then the photon is incident on the interface at an angle greater than the critical angle. In this case, the photon experiences total internal reflection, which means that R_s and R_p are set to one yielding no transmitted light through the interface.

3.1.1 Monte Carlo Ray-Tracing Model Assumptions

The main advantage of a Monte Carlo ray-tracing model compared to analytical models is the ability to model a solution with fewer assumptions. However, there are still some assumptions made to increase the speed of the calculation that are important to keep in mind.

The Monte Carlo ray-tracing models assumes that all materials and interfaces can be characterized using a geometric optics approach. This assumes that the photons can be assumed to travel as particles and the wave properties of light such as diffraction and interference can be neglected [45]. This assumption is appropriate for modeling the interfaces between air and polymers of different refractive indices when the layers are of a thickness much greater than the wavelength of light. However, this assumption breaks down when the layer is significantly thinner and not indexed matched to the polymer. In this case, it is necessary to use a wave optics approach to correctly model all the relevant phenomena [98].

The Monte Carlo model also assumes that the emitted photon is chosen from a random distribution of wavelengths over the entire emission spectrum unaffected by the wavelength of absorption. This could lead to possible non-physical phenomena where the photon is absorbed at a lower energy than it is emitted at. However, in this work, the intensity of both the absorption and emission spectrum at the wavelengths where they overlap is quite small, which will not lead to significant uncertainty in the simulation of the LSC. If there is a large overlap between the absorption and emission spectra, such as can be found in dyes, a more accurate simulation in this case could characterize the emission as a function of excitation wavelength in order to effectively model the shift in emission as a function of absorbed wavelength.

3.2 Finite Difference Time Domain Method

While Monte Carlo models effectively characterize the performance of LSCs in the ray-optics limit, they are unable to model the behavior of the LSC when the wave-like nature of light contributes to the behavior of the system. In this thesis this occurs when structures are implemented that have sizes on the order of the wavelength of light. In this regime, Finite Difference Time Domain (FDTD) modeling can be used to characterize the system.

FDTD modeling is performed by solving Maxwell's equations over a given volume

space [99].

$$\Delta \times \vec{E}(t) = -\frac{\delta \vec{B}(t)}{\delta t}$$

$$\vec{B}(t) = \mu(t) \cdot \vec{H}(t)$$

$$\Delta \times \vec{H}(t) = \frac{\delta \vec{D}(t)}{\delta t}$$

$$\vec{D}(t) = \epsilon(t) \cdot \vec{E}(t)$$

Where $\vec{E}$ is electric field, $\vec{B}$ is magnetic flux density, μ is magnetic permeability, $\vec{H}$ is magnetic field strength, ϵ is electric permittivity, and $\vec{D}$ is electric displacement.

In this thesis the FDTD calculation is performed using the software package Lumerical FDTD Solutions. To design the simulation for the FDTD method we use the CAD software in this package to build the geometry of the structure by defining the size and the refractive index of each component. The refractive index of the component may be taken from literature or we may measure it ourselves using spectroscopic ellipsometry. After defining the geometry we include light sources and monitors to observe how light interacts with our nanostructured design. Finally a simulation region is defined, a meshing size is determined, and boundaries are chosen for the edges of the simulation region.

The FDTD method can be used to effectively calculate a number of different properties for LSC systems. It can be used to calculate the interaction of incident sunlight with nanostructured LSCs including transmission, reflection, and absorption. To fully understand the performance of a nanoscale LSC, FDTD modeling can also calculate the propagation of the emitted light as well as the farfield emission angle from the nanoscale LSCs. This is used in Chapter 6 and 7 to model the propagation of emission and can also be integrated into

a Monte Carlo ray-tracing model to fully simulate a nanoscale LSC. We also use FDTD modeling in Chapter 5 to calculate the angle of reflection for a nanostructured mirror that is designed as a bottom surface mirror for a LSC.

3.2.1 FDTD Assumptions

In FDTD calculations the computational domain is gridded with a spacing determined by the mesh size defined. In this way, we assume that our structures can be effectively defined using a rectangular grid. In the case of structures that have a rectangular geometry this is a good assumption as the gridded domain will only change the size of the structures slightly to accommodate the grid. However, for non-rectangular structures this can be a bad assumption as the gridded domain will change both the size and the shape of the structures, which could significantly change how light interacts with them. In this case a very small mesh can be used to approximate the non-rectangular geometry but this can also come with significantly longer computational times.

In the calculations performed in this thesis we also assume that the nanostructures we use are perfectly smooth. This assumption allows us to successfully calculate the expected phenomena of the different mirrors and LSCs used in this thesis but it likely does not perfectly model the behavior of an experimentally fabricated system. Most fabrication methods have some amount of variability in the size and shape of the structures fabricated that is not currently captured by the model. Even if non-standard shapes are imported into FDTD software, they will still be limited by the rectangular grid.

Chapter 4

Designing Spectrally-Selective Mirrors for Use in Luminescent Solar Concentrators

4.1 Introduction

As discussed in Section 1.5 escape cone losses have a significant impact on the light guiding of the LSC by emitting light out of the top or bottom of the LSC. This corresponds to a loss of 26% of the emitted light after every absorption and emission event for a luminophore embedded in a polymer with a refractive index of 1.49. While this is a relatively small amount of loss for one emission event it quickly compounds due to reabsorption in the LSC. It is predicted that nearly 78% of the guided light will be lost to the escape cone after just 4 reabsorption events.

In order to reduce escape cone losses and reach their full operating efficiency, LSCs may utilize a spectrally-selective mirror above the top surface that transmits sunlight over the absorption band of the luminophore and traps the luminescent light within the concentrator [55]. The mirror must therefore have high transmission across the absorption band of the luminophore while also exhibiting high reflectivity across the emission band of the luminophore. One-dimensional mirrors with a reflection band are often used for this purpose, but can be challenging to design as the reflectivity band blue-shifts as the angle of

incidence increases away from normal incidence [54–56, 58, 66, 100–106]. While often made by thin film deposition, these mirrors could be made cost-effectively via spin coating or printing [58, 107, 108].

In this chapter, we show how the design of the top surface mirror changes for LSCs with varying luminophore concentration, luminophore re-absorption, quantum yield, LSC lateral size, and type of back mirror. We use CdSe/CdS core/shell nanocrystals as the luminophore, as these materials have been used in many LSC designs to date due to their tunable optical properties, high quantum yields, and resistance to photobleaching [1, 22–25, 77, 109–112]. The combination of high quantum yield, narrow emission spectrum, and tunable Stokes shift based on varying the thickness of the shell make the CdSe/CdS system an interesting case for studying the influence of luminophore properties on mirror design. However, this study should also provide insight into the design of top-surface mirrors for a variety of other candidate luminophores, including non-Cd based nanocrystals and rare-earth emitters [13, 113].

4.2 Methods

4.2.1 LSC Geometry

The simulated LSC design consists of a 3 mm thick polymerized PMMA slab with a refractive index of 1.49 and an embedded luminophore with a loading fraction that gives a variable optical density at 450 nm. A perfectly reflecting mirror is placed on the bottom of the LSC (either diffuse or specular), with an air gap between the mirror and polymer waveguide. An aperiodic spectrally-selective mirror is placed on the top of the LSC, also with an air gap. Alternatively, the top of the LSC can be open. Solar cells are mounted on all four sides of the LSC that capture the light that reaches the edge. Perfect coupling from the polymer slab to the solar cell is assumed, based on the assumption that antireflection coatings are present on the solar cell and index-matching layers are included between the

solar cell and the polymer slab [14, 114]. The chosen luminophores consist of a CdSe core with a CdS shell of varying thickness (0 monolayers, 3 monolayers, or 7 monolayers). The absorption and emission spectra are taken from experimental measurements of synthesized nanocrystals following the methods referenced [77,87,88,111]. Unless otherwise specified, calculations are shown using CdSe/CdS nanocrystals with a 7 monolayer CdS shell, with an optical density of 0.5 at 450 nm, and for LSC lateral dimensions of 1 m x 1 m.

Two related figures of merit are used to describe LSC performance: concentration factor and optical efficiency. The concentration factor is defined as:

$$C = \frac{\Phi_{solar}}{\Phi_{inc}} = \eta_{opt} G$$

where Φ_{solar} and Φ_{inc} are the flux into the solar cell and the flux into the top face respectively. The concentration factor can also be defined as the optical efficiency $\left(\eta_{opt}\right)$ times the geometric ratio (G), where the geometric ratio is the area of the top face divided by the areas of the solar cells. The optical efficiency is the fraction of incident photons that reach the edge of the concentrator and are assumed to be collected.

4.2.2 Ray-tracing Monte Carlo model

A ray-tracing Monte Carlo model was used to predict the performance of the LSCs. This modeling algorithm has been utilized often to predict the performance of LSCs with different operating conditions [1, 21, 23, 24, 44, 94, 104, 115, 116]. The ray-tracing model uses the angle-dependent reflectivity of the aperiodic mirror, the geometry of the LSC, the optical properties of the luminophore and polymer, and the reflectivity and scattering properties of the back reflector as input parameters. Photons are injected normal to the LSC surface and tracked as they are absorbed by the luminophores, emitted, reflected off of the mirrors, and refracted through the interfaces of the concentrator. Absorption by the luminophores is determined using the absorption spectrum of the luminophore and Beers

law, and the properties at interfaces are determined using Fresnel's equations [117, 118].

The number of photons collected by the solar cell or lost to various processes are explicitly tracked during the simulation. Photons that reach the edge of the concentrator are counted as collected. Lost photons include photons that are absorbed and lost non-radiatively, photons that are reabsorbed and then lost non-radiatively, photons that are lost to the escape cone, and photons that are not absorbed and escape the LSC. The first two loss mechanisms distinguish between losses from the first absorption event and losses that result from subsequent absorption events arising from the spectral overlap between luminophore absorption and emission.

The calculations are performed at every wavelength, and then weighted by the AM1.5 G solar spectrum.

$$\eta_i = \frac{\int_{\lambda_1}^{\lambda_2} \eta_i(\lambda) P_{ss}(\lambda) d\lambda}{\int_{\lambda_1}^{\lambda_2} P_{ss}(\lambda) d\lambda}$$

Here η_i is the fraction of light collected or lost, P_{ss} is the power in the AM1.5G solar spectrum as a function of wavelength, λ_1 is the start of the integration, which was taken to be 400 nm for these calculations, and λ_2 is the end of the integration, which is taken to be the wavelength where $\alpha(\lambda) = 0.01$ cm^{-1}. This is dependent on the absorption spectrum of the luminophore. Running the simulations for identical conditions multiple times results in less than 0.5% relative difference in the weighted optical efficiency.

4.2.3 Model for light absorption and propagation within the luminescent solar concentrator

An additional model was also used to verify the Monte Carlo model and to predict the fraction of incident light absorbed on each pass through the concentrator. This model takes the angle-dependent reflectivity of the aperiodic mirror and the absorption spectrum of the luminophore as input parameters, then calculates the fraction of photons absorbed and lost

on each pass. The fraction absorbed is given as

$$F_{abs} = 1 - 10^{-\alpha(\lambda)ct}$$

where $\alpha\left(\lambda\right)$ is the molar absorptivity coefficient in units of $\frac{\text{L}}{\text{mol cm}}$, c is concentration in units of $\frac{\text{mol}}{\text{L}}$, and t is the distance in units of cm.

On the first pass, the incident photons may be reflected off the top mirror, reflected off the polymer/air interface between the LSC and the mirror and transmitted back out of the LSC through the mirror, or transmitted into the concentrator where they may be absorbed. The fraction of the total photons lost to the first two pathways is given by

$$F_{lost,1}\left(\lambda\right) = R_{TopMirror}\left(\theta = 0, \lambda\right) + R_{air,LSC}\left(\theta = 0, \lambda\right)\left(1 - R_{TopMirror}\left(\theta = 0, \lambda\right)\right)$$

where $R_{TopMirror}$ is the reflectance of unpolarized light for the spectrally-selective mirror at normal incidence and as a function of wavelength, and $R_{air,LSC}$ is the reflectance of unpolarized light for the air/LSC interface as calculated by Fresnel equations at normal incidence.

The photons that are absorbed in the first pass are therefore those that transmit through the top surface mirror and are absorbed within the first pass through the concentrator, which depends on the thickness t and the molar absorption coefficient of the polymer/luminophore composite, α.

$$F_{abs,1}\left(\lambda\right) = \left(1 - F_{lost,1}\right)\left(1 - 10^{-\alpha(\lambda)ct}\right)$$

After the first pass the remaining photons reflect off the back mirror, which may be diffuse or specular. The diffuse mirror hemispherically scatters the incident photons, giving the reflected photons the angular distribution

$$I(\theta) = 2\sin\theta\cos\theta$$

where θ is the angle with respect to normal that the reflected photon makes with the top spectrally-selective mirror. After reflection from the diffuse mirror the calculation for multiple passes is split up into even and odd passes.

Even passes correspond to photons that travel from the diffuse mirror to the top mirror. For even passes the photons that are absorbed are those that have not been absorbed or lost previously, and are absorbed as the travel from the bottom to the top of the concentrator.

$$F_{abs,2i}(\lambda) = F_{remain,2i-1}(\lambda)\left(1 - \frac{\int_0^{\pi/2} 10^{\frac{-\alpha(\lambda)ct}{\cos\theta_p(\theta)}} 2\sin\theta\cos\theta d\theta}{\int_0^{\pi/2} 2\sin\theta\cos\theta d\theta}\right)$$

where $F_{remain,2i-1}$ is the fraction of photons that have not been absorbed or lost up to the current pass through the concentrator, and θ_p is the angle of reflected photons in the concentrator. This angle is used to calculate the effective path length of the light for Beers law. The photons that are lost on the even passes are those that are not absorbed as they travel from the bottom to the top of the concentrator and are transmitted through the top wavelength-selective mirror. This model neglects the additional reflection off the top polymer/air interface.

$$F_{lost,2i}(\lambda) = \left(F_{remain,2i-1}(\lambda) - F_{abs,2i}(\lambda)\right)\left(1 - \frac{\int_0^{\pi/2} R_{TopMirror}(\theta,\lambda)\, 2\sin\theta\cos\theta d\theta}{\int_0^{\pi/2} 2\sin\theta\cos\theta d\theta}\right)$$

Odd passes correspond to photons that travel from the top wavelength-selective mirror to the diffuse mirror. The photons that are absorbed are those that are transmitted into the concentrator on this pass and absorbed by the luminophores in the concentrator.

$$F_{abs,2i+1}(\lambda) = \left(F_{remain,2i}(\lambda) - F_{lost,2i+1}(\lambda)\right)\left(1 - \frac{\int_0^{\pi/2} 10^{\frac{-\alpha(\lambda)ct}{\cos\theta_p(\theta)}} 2\sin\theta\cos\theta d\theta}{\int_0^{\pi/2} 2\sin\theta\cos\theta d\theta}\right)$$

The photons that are lost on odd passes are those that have not been absorbed or lost on any previous pass, reflect off the top air/polymer interface, and transmit out of the top wavelength-selective mirror.

$$F_{lost,2i+1}(\lambda) = F_{remain,2i}(\lambda)\frac{\int_0^{\pi/2} R_{air,LSC}(\theta)\, 2\sin\theta\cos\theta d\theta}{\int_0^{\pi/2} 2\sin\theta\cos\theta d\theta}$$
$$\left(1 - \frac{\int_0^{\pi/2} R_{TopMirror}(\theta,\lambda)\, 2\sin\theta\cos\theta d\theta}{\int_0^{\pi/2} 2\sin\theta\cos\theta d\theta}\right)$$

The fraction absorbed and lost for a concentrator with a specular back reflector are calculated in a similar way. However, instead of integrating the reflectivity and Beers law with respect to angle the calculation is done at normal incidence. The fractions of photons absorbed and lost on each pass for either mirror case form a converging series. The sum of the terms in this series converges to the approximate fraction of incident light absorbed by the luminophores.

The largest source of error in these calculations derives from the neglected additional reflections off the top polymer/air interface on even passes. By comparing this model to the absorption values extracted from the Monte Carlo model, we find approximately 1% difference between the two calculations.

4.2.4 Designing spectrally-selective mirrors

A series of spectrally-selective mirrors were designed to improve the performance of the LSC. These mirrors consist of alternating layers of refractive index 2.53 and 1.45,

which creates a photonic bandgap where light transmission is forbidden. The location of this photonic bandgap is determined by the thickness of the mirror layers and the refractive index of the dielectric material.

The thicknesses of the layers in the spectrally-selective mirror were determined using an optimization method in MATLAB [119]. This method uses the refractive index of the layers, the absorption spectrum of the luminophore, the emission spectrum of the luminophore, and an initial guess for the thickness of each layer in the mirror as input parameters. A periodic 1D Bragg stack was used as an initial guess where the thickness of each layer is the peak of the emission spectrum divided by four times the refractive index of the layer.

Optimum thicknesses for the layers are calculated by minimizing the reflection that spectrally overlaps with the absorption spectrum and maximizing the reflection over the emission band.

$$FOM = \left(\frac{1}{A}\right)^{W_a} \left(\frac{1}{E}\right)^{W_e}$$

A and E are the figures of merit related to the reflection over the absorption band and emission band, respectively. W_a and W_e are the weighting terms for the absorption and emission term. The weighting terms thus give optical transmission or trapping of emission more weight.

The A figure of merit is calculated by integrating the transmission of the top mirror at normal incidence over the absorption band and weighting it by the solar spectrum.

$$A = \frac{\int_{\lambda_{A,min}}^{\lambda_{A,max}} \left(1 - R_{TopMirror}\left(\theta = 0, \lambda\right)\right) \alpha\left(\lambda\right) P_{ss}\left(\lambda\right) d\lambda}{\int_{\lambda_{A,min}}^{\lambda_{A,max}} \alpha(\lambda) P_{ss}(\lambda) d\lambda}$$

The E figure of merit is calculated by integrating the reflection of the top mirror over the emission band and the emitted angles

$$E = \frac{\int_{\lambda_{E,min}}^{\lambda_{E,max}} \int_0^{\frac{\pi}{2}} PL\left(\lambda\right) R_{TopMirror}\left(\theta, \lambda\right) d\theta d\lambda}{\int_{\lambda_{E,min}}^{\lambda_{E,max}} \int_0^{\frac{\pi}{2}} PL\left(\lambda\right) \sin\theta d\theta d\lambda}$$

where PL is the emission spectrum of the luminophore, and θ is the angle of emission from the luminophore. The optimum design is then used to calculate the reflectivity of the mirror as a function of polarization, wavelength, and angle, which can be integrated into the Monte Carlo calculation. This procedure was used to design a series of different spectrally-selective mirrors.

4.3 Results and Discussion

There are several important differences in LSC operation between the case with an open top and one with a spectrally-selective mirror on the top surface. To quantify these differences, we describe the optical efficiency of a LSC as the product of the absorption efficiency (η_{abs}), the emission efficiency $\left(\eta_{QY}\right)$, the trapping efficiency $\left(\eta_{trap}\right)$, and the waveguide efficiency $\left(\eta_{wg}\right)$ as discussed in Section 1.4 [44].

$$\eta_{opt} = \eta_{abs}\eta_{QY}\eta_{trap}\eta_{wg}$$

When a spectrally-selective mirror is introduced on the front surface, the efficiencies of η_{abs}, η_{trap}, and η_{wg} change. The quantum yield η_{QY} does not because it is assumed to be independent of the mirrors, and is therefore only a property of the luminophore-polymer composite. As seen from the absorption efficiency η_{abs} expression above, the presence of a spectrally-selective mirror on the top surface changes the front interface reflectivity R, which now exhibits both more spectral dependence and is generally increased over an open top concentrator. This prevents some light from entering the concentrator but also traps weakly absorbed photons within the concentrator, allowing for increased path lengths and larger multi-pass absorption over some wavelengths (Figure 4.1).

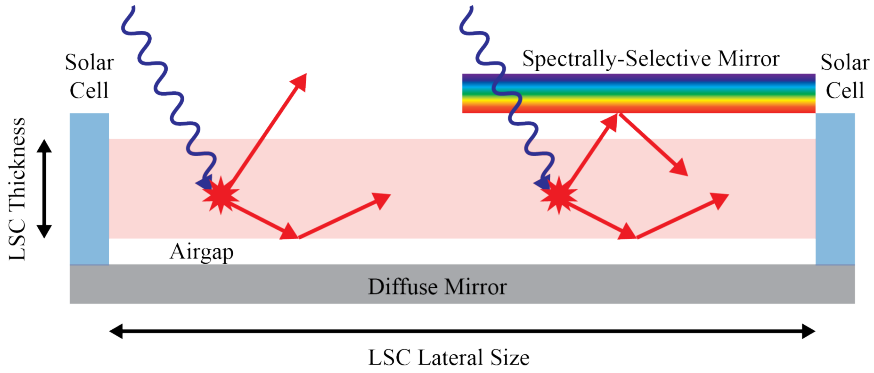

Figure 4.1: Schematic showing the benefits of a spectrally-selective top mirror on a luminescent solar concentrator. The red layer in the LSC is embedded with CdSe/CdS quantum dots. Solar cells are mounted to the left, right, front, and back faces of the polymer waveguide (n=1.49). A diffuse mirror is mounted to the bottom face of the waveguide with a 100 μm air gap. The top face is open or has a spectrally-selective mirror mounted with a 100 μm air gap.

The trapping efficiency η_{trap} changes when the top mirror is introduced, as light that would otherwise couple to the escape cone in an open-top concentrator is now trapped inside the concentrator. In an open top concentrator, the fraction trapped after each absorption and emission event is governed by the refractive index of the polymer-luminophore composite and the refractive index of the cladding, and is given by

$$\eta_{trap,i} = \cos\left(\sin^{-1}\frac{n_2}{n_1}\right)$$

where n_2 is the refractive index of air, and n_1 is the refractive index of the polymer-luminophore slab. With a reflecting mirror on the top surface, however, some of the light that passes through the polymer-air interface will be reflected back into the concentrator from the top surface mirror.

$$\eta_{trap,i} = \cos\left(\sin^{-1}\frac{n_2}{n_1}\right) + \left(1 - \cos\left(\sin^{-1}\frac{n_2}{n_1}\right)\right)\left(\frac{\int_0^{\frac{\pi}{2}} I(\theta)\, R_{TopMirror}(\theta)\, d\theta}{\int_0^{\frac{\pi}{2}} I(\theta)\, d\theta}\right)$$

where $I(\theta)$ is the intensity of light transmitted into the top air gap as a function of angle and $R_{TopMirror}(\theta)$ is the reflectivity of the top spectrally-selective mirror as a function of angle of incidence. In this way the escape cone losses will be suppressed on each absorption and emission event. The full expression of η_{trap} for the LSC accounts for this process for every absorption and re-emission event.

The waveguide efficiency η_{wg} describes the losses of the propagating photons that are already trapped within the concentrator. This will depend on the overlap between absorption and emission for the chosen luminophore, as some of the luminescent light may be reabsorbed by the luminophore during propagation. This term also depends on the absorption losses of both the front and back mirrors. In an open top configuration all of the trapped light is in total internal reflection modes between the polymer and air, and therefore has no interaction with the mirrors, and so this term primarily measures reabsorption. In the presence of a spectrally-selective mirror, however, the light that would have coupled to the escape cone is trapped inside the concentrator. Some of these photons propagate at near-normal angles and interact with the mirrors upon every pass through the waveguide, and are now especially vulnerable to reabsorption and mirror losses [104]. Thus the waveguide efficiency η_{wg} losses will increase when spectrally-selective mirrors are added to the top surface.

4.3.1 Designing spectrally-selective mirrors for the top surface of luminescent solar concentrators

Figure 4.2 shows a series of aperiodic top-surface mirrors designed to favor different scenarios. Aperiodic mirrors were chosen over periodic mirrors in order to suppress the reflection throughout the spectral region where the luminophores absorb. In Figure 4.2 (a) the reflectivity at normal incidence is shown overlaid against the absorption and emission spectra of a CdSe/CdS core/shell nanocrystal with a 7 monolayer CdS shell. In Figure 4.2 (b), the reflectivity weighted by the emission spectrum is shown as a function of angle.

Layer	Refractive index	Emission Weight 8	Emission Weight 6	Emission Weight 2	Emission Weight 1.5	Equal Weight	Absorption Weight 2	Absorption Weight 6
1	1.45	134.32	327.57	329.39	331.64	329.98	335.48	337.09
2	2.53	235.58	185.26	190.59	189.96	186.85	200.92	204.05
3	1.45	185.93	192.80	191.68	197.21	197.93	195.91	196.76
4	2.53	193.05	163.25	168.78	161.67	158.74	174.92	180.29
5	1.45	165.33	194.80	194.79	208.76	211.23	204.72	201.57
6	2.53	187.68	164.26	162.71	144.99	141.73	152.63	162.52
7	1.45	170.80	183.54	191.54	210.08	213.91	220.85	213.20
8	2.53	175.51	178.73	167.75	154.42	149.17	132.74	147.94
9	1.45	181.37	167.92	185.00	194.23	200.92	232.96	222.07
10	2.53	167.67	187.04	171.93	178.25	171.21	124.73	140.35
11	1.45	181.37	167.92	185.00	172.21	185.46	232.96	222.07
12	2.53	175.51	178.73	167.75	198.21	190.36	132.74	147.94
13	1.45	170.80	183.54	191.54	159.74	189.68	220.85	213.20
14	2.53	187.68	164.26	162.71	206.34	234.03	152.63	162.52
15	1.45	165.33	194.80	194.79	177.06	272.93	204.72	201.57
16	2.53	193.05	163.25	168.78	241.14	269.44	174.92	180.29
17	1.45	185.93	192.80	191.68	278.57	274.66	195.91	196.76
18	2.53	235.58	185.26	190.59	258.37	260.89	200.92	204.05
19	1.45	134.32	327.57	329.39	259.96	357.58	335.48	337.09

Table 4.1: The full layer thicknesses (nm) of each of the mirrors shown in Figure 4.2 are listed here.

The mirrors are classified as absorption weighted or emission weighted, as described in the methods section above. The absorption weighted mirrors are designed to favor transmission into the concentrator, having the onset of the reflectivity bands at longer wavelengths and thus having higher transmission across the absorption band of the luminophore, but also showing more angle-dependent reflectivity across the emission band. The emission weighted mirrors favor trapping of the emitted light, and are therefore designed to have the onset of the reflectivity band at shorter wavelengths at the expense of the transmission of the absorbing photons, and to exhibit more omnidirectional reflectivity across the wavelengths of the emission band of the luminophore. The full mirror layer thicknesses are given in Table 4.1.

Figure 4.3 shows how the presence of a top mirror affects η_{abs}, comparing a LSC with a diffuse back mirror (Figure 4.3 (a)) to one with a specular back mirror (Figure 4.3 (b)), and

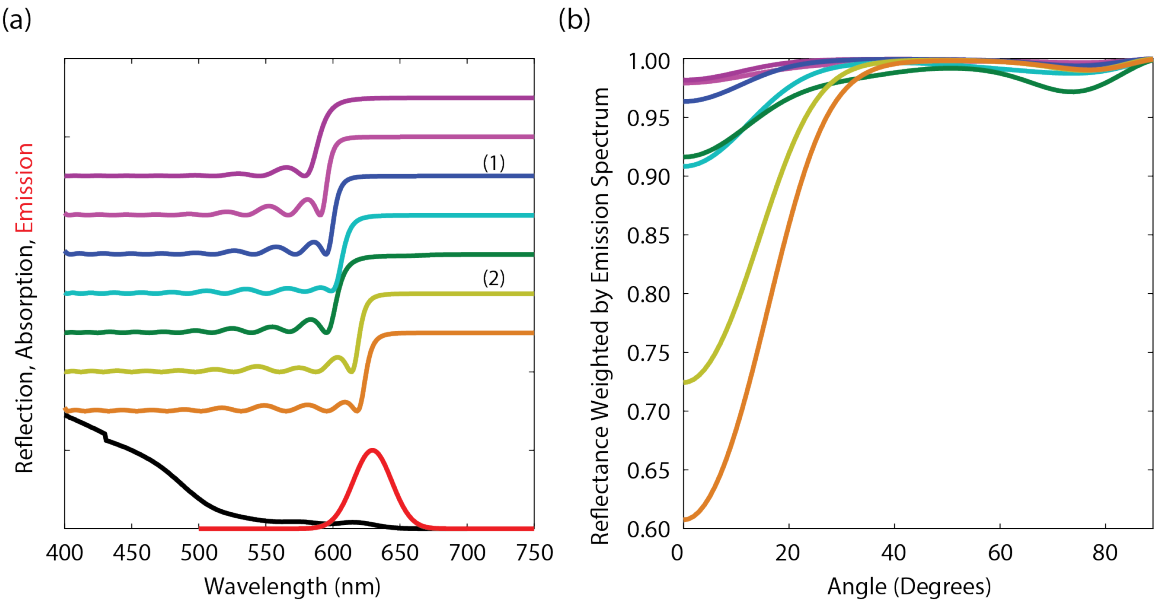

Figure 4.2: (a) Reflection of different aperiodic mirrors at normal incidence overlaid on the absorption (black) and emission spectrum (red) of a CdSe/CdS core/shell nanocrystal with a 7 monolayer shell. The mirror labeled (1) is the emission weighted mirror referred to in later figures, and the mirror labeled (2) is the absorption weighted mirror. (b) Reflectance of the aperiodic mirrors weighted by the emission spectrum of the luminophore, as a function of angle of incidence on the mirror.

with the top surface mirror (labeled (1) and blue from Figure 4.2). The largest difference in performance between the two back mirrors occurs after multiple passes. On the first pass, the absorption between both cases will be the same. A slight difference is seen in the second pass where the light has reflected off the mirror, as the diffuse mirror case will have a slightly longer path length than the specular mirror. For open top concentrators, it is already a well-known result that diffuse mirrors on the back surface improve performance due to the hemispherical back scattering off that surface [67, 120]. The most significant improvement in the absorption for the concentrator with the diffuse back reflector occurs over the spectral range from 550 nm to 600 nm. This occurs because the reflectivity of the aperiodic mirror shifts to shorter wavelengths as the angle of incidence increases away from normal incidence. Therefore, a wavelength range exists such that the light will transmit at normal incidence, scatter from the diffuse back reflector, and hit the front mirror

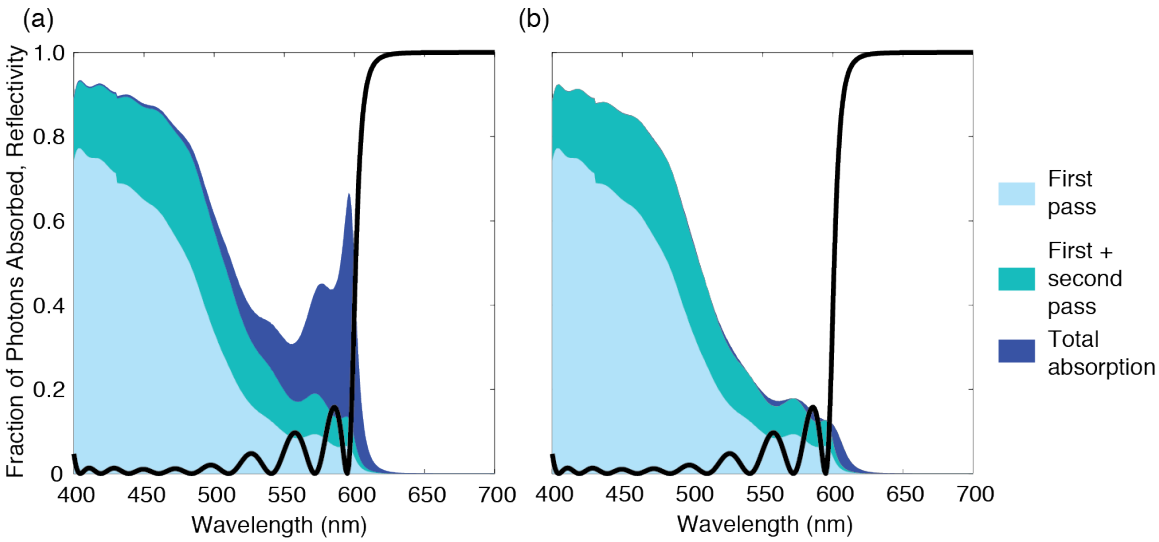

Figure 4.3: Comparison of incident light absorbed as a function of wavelength for a concentrator with a diffuse mirror (a) and a specular mirror (b) on the back. The concentrator has the emission weighted mirror ((1) from Figure 4.2) on the top surface, and the normal incidence reflectance spectrum of this mirror is shown as a guideline.

again at an oblique angle. This increases the number of passes that the light will travel through the concentrator, which in turn increases the likelihood that it will be absorbed by the luminophores. This effect is most pronounced for the wavelength range where the luminophores are weakly absorbing, as seen in the dark blue region of Figure 4.3 and in Figure 4.4 where we compare the predicted absorption for an OD of 0.5 and 5.0 at 450 nm.

From the seven mirrors that were shown in Figure 4.2, two were chosen for further comparison as they represent local maxima for concentrators with an OD of 0.5 at 450 nm (Table 4.2) and a quantum yield of 0.9. These mirrors were chosen to represent one emission weighted mirror that was designed to reflect the emitted light (labeled (1) and blue in Figure 4.2) and one absorption weighted mirror that was designed to transmit light at normal incidence across the absorption band of the luminophore (labeled (2) and yellow in Figure 4.2). These two mirrors will be compared in the next several studies.

Figure 4.5 (a) shows that the difference in performance between the LSCs with the absorption weighted and emission weighted aperiodic mirrors depends on the quantum

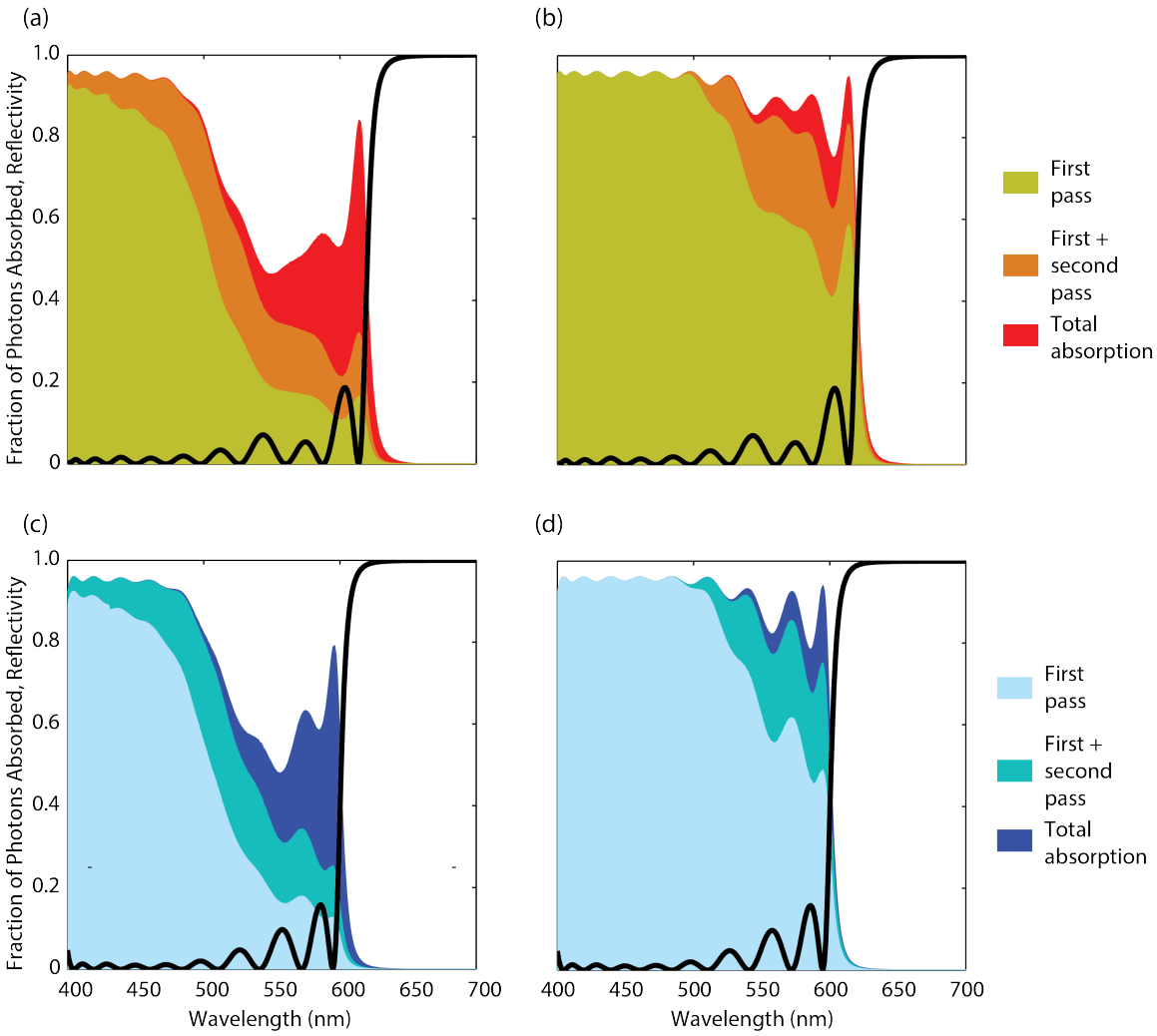

Figure 4.4: Comparison of incident light absorbed as a function of wavelength for a concentrator with an OD of 0.5 (left) and an OD of 5.0 (right) for a diffuse mirror on the back. (top) The concentrator has the absorption weighted mirror ((1) from Figure 4.2) on the top surface. (bottom) The concentrator has the emission weighted mirror ((2) from Figure 4.2) on the top surface. The normal incidence reflectance spectrum of each mirror is shown as a guideline in black.

yield of the luminophore. Above a quantum yield of 0.85, the concentrator with the emission weighted mirror outperforms the concentrator with the absorption weighted mirror, whereas at quantum yields below 0.85 no discernible difference is present. Both mirrors produce substantial gains over the open top concentrator at the full range of quantum yields simulated.

However, despite the comparable performance of these mirrors, the underlying reasons

OD	Emission Weight 8	Emission Weight 6	Emission Weight 2	Emission Weight 1.5	Equal Weight	Absorption Weight 2	Absorption Weight 6
0.25	16.94	17.56	17.53	16.14	14.90	16.22	15.41
0.50	17.82	18.36	18.42	17.22	16.05	17.41	16.69
0.75	16.78	17.23	17.38	16.45	15.43	16.75	16.20
1.00	15.54	15.92	16.10	15.40	14.53	15.79	15.36
1.50	13.39	13.67	13.89	13.48	12.82	13.93	13.71
2.00	11.75	11.98	12.22	11.99	11.45	12.46	12.35
3.00	9.49	9.66	9.89	9.83	9.44	10.29	10.30
4.00	8.03	8.17	8.36	8.37	8.08	8.82	8.87
5.00	6.99	7.09	7.29	7.35	7.08	7.74	7.81

Table 4.2: Calculated concentration factors for LSCs containing CdSe/CdS nanoparticles with a 7 monolayer CdS shell. The OD is determined at 450 nm, and a diffuse mirror is included on the back. The quantum yield is 0.9.

for the performance differs. The emission weighted mirror permits less light to enter the concentrator, but more of the luminescent light that hits the mirror at oblique angles is trapped within the concentrator. This can be seen in Figures 4.5 (b) and 4.5 (c), which show that the fraction of total photons ultimately lost to reabsorption is slightly higher for the emission weighted mirror compared to the absorption weighted mirror, the fraction of the total photons lost to the escape cone is considerably lower, and that the fraction of total photons transmitted into the concentrator is smaller. In comparison to an open top concentrator, both mirrors lose considerably more light to reabsorption and less to the escape cone.

Figure 4.5 (d) compares the calculated η_{trap} and η_{wg} for these LSCs. The absorption efficiency η_{abs} is independent of quantum yield, and η_{abs} for the absorption weighted mirror exceeds η_{abs} for the emission weighted mirror by 3.6%. The trapping efficiency η_{trap}, however, depends on the quantum yield and favors the emission weighted mirror by 5% at quantum yield of 0.6. The waveguide efficiency η_{wg} is relatively constant between quantum yields of 0.6 and 0.85, favoring the absorption weighted mirror by approximately 2.5%. Since η_{opt} is the product of all of these efficiencies, the relative benefits and losses from

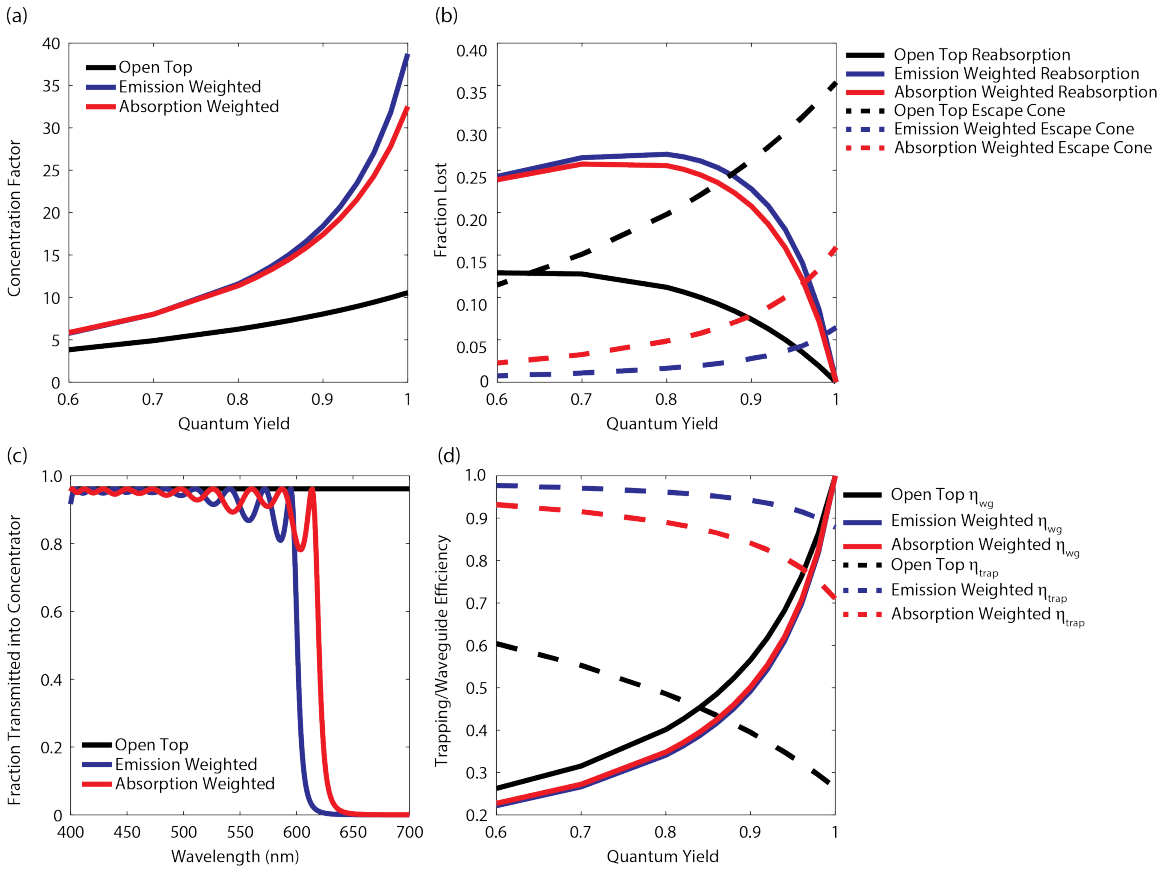

Figure 4.5: Monte Carlo ray-tracing simulations showing the predicted concentration factor and loss mechanisms for LSCs with different top mirror configurations. Results are shown for a LSC with an open top (black), a LSC with an emission weighted aperiodic mirror above the top surface (blue), and an absorption weighted aperiodic mirror above the top surface (red), where (a) shows the concentration factor, (b) shows the number of photons lost to reabsorption non-radiative losses (solid) and the escape cone (dashed), (c) shows the fraction of incident light that is transmitted into the concentrator for each mirror configuration, and (d) shows the waveguide efficiency (solid) and trapping efficiency (dashed).

the different mirrors are essentially canceled out at quantum yields between 0.6 and 0.85. At quantum yields greater than 0.85, the advantage of η_{trap} for the emission weighted mirror increases significantly, and the advantage of η_{wg} for the absorption weighted mirror declines slightly, leading to much higher performance for the emission weighted mirror.

Under these conditions, either mirrors that are designed to maximize absorption or trapping of emission lead to higher performance than other intermediate mirror designs. Only when the quantum yield is high do we find that it is preferable to maximize the trapping of

emission, as there is significant photon recycling in the concentrator from the repeated absorption and emission events. Nevertheless, even low quantum yield luminophores benefit from the introduction of a spectrally-selective mirror.

4.3.2 Mirror designs for varying luminophore loading fractions

To further probe the role of photon recycling in the concentrator, we studied how η_{opt}, η_{abs}, η_{trap}, and η_{wg} change as a function of the concentration of the luminophores for the same two mirrors discussed in Figure 4.2. Concentrators with optical densities of 0.1 to 2.0 at 450 nm were simulated for a 1 m x 1 m concentrator and a luminophore quantum yield of 0.9. This corresponds to a relative change in the loading fraction of luminophores in the concentrator from 10 - 200% compared to an optical density of 1.0. We find the largest optical efficiencies η_{opt} at an optical density of 0.4 for the emission weighted mirror and at an optical density of 0.5 for the absorption weighted mirror, as seen in Figure 4.6 (a). An open top concentrator, in contrast, exhibits optimal optical density of only 0.3 at 450 nm. In the open top concentrator, η_{abs} only increases slowly as a function of increased loading fraction since there is no additional trapping effect, which drives the optimum toward lower loading fractions. Regardless of the mirror used, an increase in the optical density of the luminophores leads to an increase in the fraction of incident light absorbed, an increase in the trapping efficiency, and a decrease in the waveguide efficiency, as shown in Figures 4.6 (b) - (d). This reduced waveguide efficiency is indicative of the larger number of reabsorption events occurring in a concentrator with higher concentration luminophores: under these conditions, the luminescent photons are more likely to be reabsorbed during propagation. The tradeoff between the increased total light absorption and the increased reabsorption losses for high concentrations results in the calculated optimum optical densities.

Figure 4.6 also shows the relative performance differences between the mirrors. In general the emission weighted mirror is preferred for low loading fractions, while the absorption weighted mirror is preferred for an optical density at 450 nm greater than 1.4. The

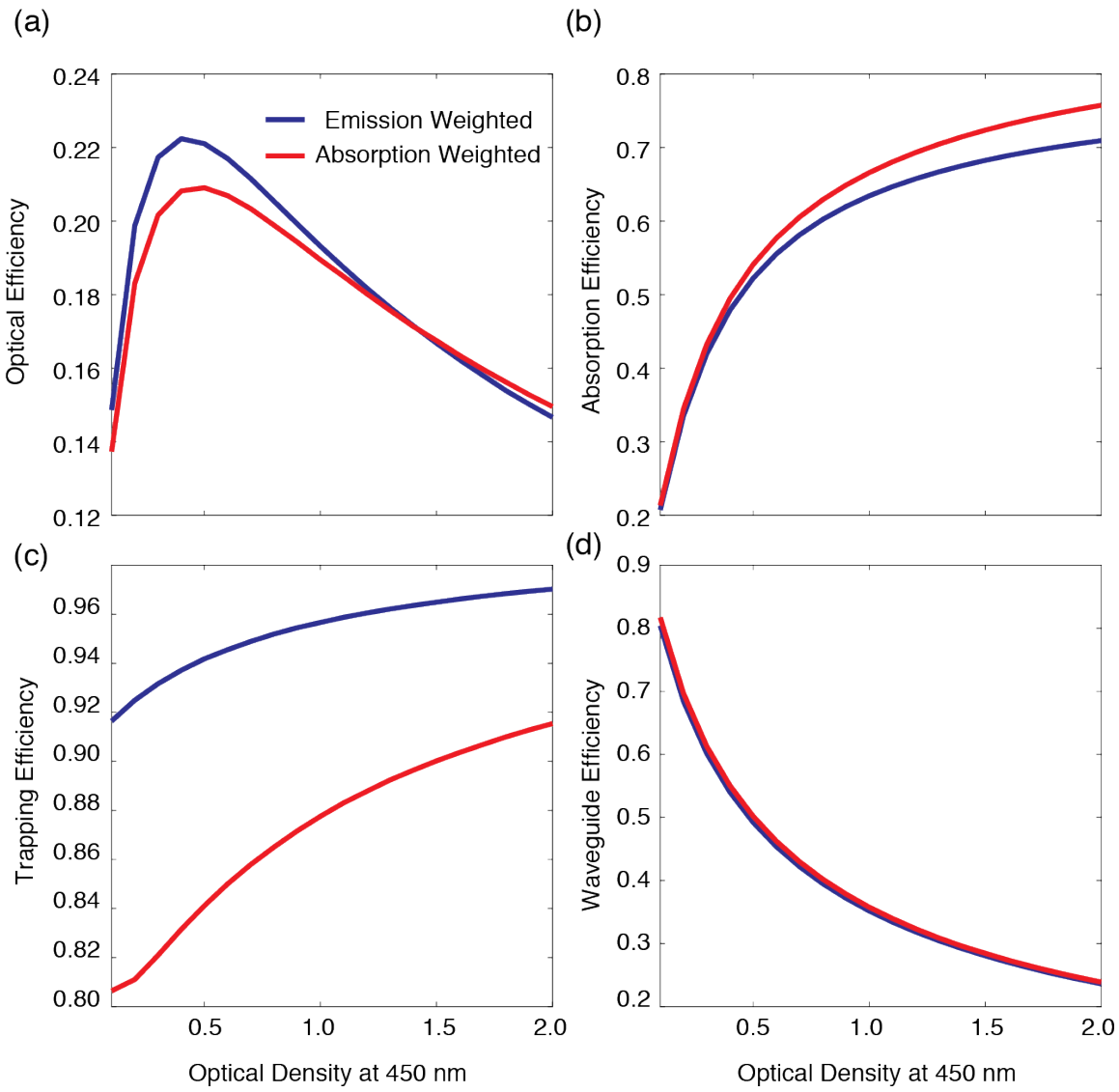

Figure 4.6: Comparison of the LSC efficiency as a function of luminophore loading fraction, or optical density at 450 nm. The emission weighted aperiodic mirror is shown in blue, and the absorption weighted aperiodic mirror in red. The (a) optical efficiency is calculated with the Monte Carlo ray-tracing model, the absorption efficiency (b) from ray tracing with multiple reflections, and the trapping efficiency (c) and waveguide efficiency (d) from the Monte Carlo ray-tracing model.

absorption efficiency η_{abs} for the LSC with the absorption weighted mirror increases faster with increasing luminophore loading relative to η_{abs} for the concentrator with the emission weighted mirror, as shown in Figure 4.6 (b). At a low loading fraction the luminophore weakly absorbs in the region between the reflectivity band onset of the absorption and

emission weighted mirror, which means there is little additional benefit from the extra light the absorption weighted mirror lets into the concentrator. Here, as seen in Figure 4.3, there can be some benefit to having an emission weighted mirror to absorb this light in multiple passes. However, as the loading fraction increases, a larger fraction of the incident light is absorbed on the first or second pass, which favors the absorption weighted mirror shown by a 2.9 - 6.8% relative improvement in η_{abs}. Similarly, Figure 4.6 (c) shows that η_{trap} is significantly higher for the emission weighted mirror, but the relative amount of improvement of η_{trap} for the emission weighted mirror declines as the luminophore concentration increases. There is little difference in η_{wg} (Figure 4.6 (d)) for these two cases, as for simplicity the back mirror was given a reflectivity of 1.0 and the materials in the top mirror are non-absorbing at these wavelengths. The interaction with the mirrors is therefore comparable, and so η_{wg} should be similar regardless of top surface mirror. The crossover point occurs when the relative benefit from the emission weighted mirror for η_{trap} equals the relative benefit for η_{abs} and η_{wg} for the absorption weighted mirror. This occurs at an optical density of 1.4 for this system. These calculations reinforce that a judicious combination of loading fraction optimization and spectrally-selective mirrors improves the overall concentration factors, while also indicating that highly absorbing luminophores may be better served by an absorption-weighted mirror.

4.3.3 Mirror designs for varying luminescent concentrator lateral size

The optimal mirror design also varies depending on the size of the concentrator. Large scale concentrators could be used in building integrated applications or architectural panels, whereas small-scale concentrators could find application for specific photovoltaic materials. To study an optimistic case, these concentrators were simulated with a quantum yield of 1.0 and an optical density of 0.5 at 450 nm. As seen in Figure 4.7 (a), the absorption weighted aperiodic mirror is preferred for small concentrators. The absorption efficiency

η_{abs} should be independent of lateral size because the absorption of incident light depends on the distance the photon travels through the thickness of the concentrator, not the lateral dimensions (see Figure 4.6 (b) for the difference in η_{abs} for these two mirrors). When the concentrator is small there is additional effect from light scattering: some of the incident photons will be scattered to the edge of the concentrator without undergoing the absorption and luminescence process. This also favors the absorption weighted mirror. The trapping efficiency η_{trap} depends on the size of the concentrator. At a small lateral size, a large fraction of the emitted light will reach the edges of the LSC with minimal interaction with the top mirror. This is shown in Figure 4.7 (b) by the similar η_{trap} values between the concentrators with absorption and emission weighted aperiodic mirrors in Figure 4.7 (b). At these small sizes, performance is therefore limited by the absorption, and so it is more important to use a mirror that allows a large fraction of the incident light into the concentrator.

At larger sizes, the emission weighted mirror is favored. As the lateral size of the concentrator increases the emitted light interacts more often with the top mirror and with the luminophores in the concentrator because it has a longer average path to travel to reach the solar cell. This is observed by the significant drop in trapping efficiency for both the absorption and emission weighted mirrors in Figure 4.7 (b) as the lateral size increases. However, the emission weighted mirror retains higher trapping efficiency values for larger LSC lateral sizes.

The crossover point between the two mirrors occurs when the relative benefit of each mirror is equal. This is observed in Figure 4.7 (a) at a lateral size of slightly larger than 10 cm. The absorption weighted mirror provides a relative benefit of 3.6% to η_{abs}. At small sizes, there is an additional contribution from direct scattering into the solar cell that gradually declines from 5.1% at small sizes to 0.4% at large sizes. In contrast the relative advantage of the emission weighted mirror to η_{trap} increases much more rapidly, from 0% at small sizes to nearly 30% at the 10 m x 10 m concentrator. The crossover point occurs

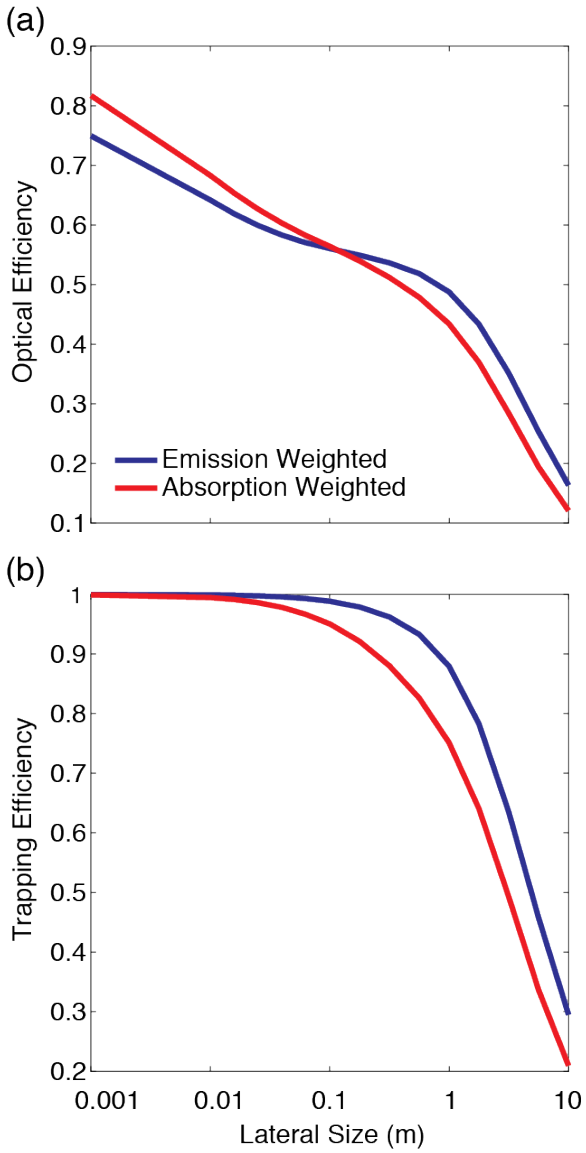

Figure 4.7: Monte Carlo simulations showing the optical efficiency (a) and trapping efficiency (b) of concentrators with an emission weighted (blue) and absorption weighted (red) aperiodic mirror on top.

when the relative benefits are equal.

4.3.4 Mirror designs for luminophores with different Stokes shifts

In an ideal scenario the absorption and emission of the luminophore would have no overlap, and the reflectivity band could be chosen to trap all the luminescent light without decreasing the transmission. However, many luminophores exhibit some overlap between

these bands, which makes choosing the spectral properties of the mirror more challenging [58]. To study this effect systematically, we used a family of Cd-based nanocrystal luminophores. These nanocrystals include CdSe core particles with a 0, 3, or 7 monolayer CdS shell. A set of mirrors (similar to Figure 4.2) were designed for each case using the absorption and emission spectra of each of the luminophores, and the concentrators with the highest η_{opt} are shown in Figure 4.8. The best top surface mirror for each luminophore was determined by simulating the concentrators with a quantum yield of 0.9, an optical density of 1 at 450 nm, and a lateral size of 1 m x 1 m.

For luminophores with significant overlap between the absorption and emission spectra, we find that it is more important to allow light into the concentrator than to reflect the emitted light. As seen in Figures 4.8 (a) and 4.8 (b), the optimum mirrors for the concentrators with the CdSe and CdSe/3ML CdS luminophores transmit a large fraction of the incident light, but have poor reflection of the emitted light at lower angles. In these cases, there is significant absorption near the onset of the reflectivity band due to the presence of high intensity excitonic features for core and core/thin shell nanocrystals. Therefore, small shifts in the reflectivity band onset have a large impact on the absorption efficiency of the concentrator.

The luminophores with significant overlap between the absorption and emission spectra also have a smaller η_{wg} than the luminophores with a small overlap between the absorption and emission spectra, due to the high likelihood of reabsorption of emitted photons. The emitted photons in concentrators with significant spectral overlap are less likely to interact with the top surface mirror than the emitted photons in concentrators using a luminophore with a large Stokes shift. The decrease in interaction with the top mirror reduces the benefit of an emission weighted mirror that traps the emitted light over a large range of angles. This can be seen from the reflectivity of the optimum mirrors for CdSe and CdSe/3ML CdS luminophores shown in Figure 4.8 (b).

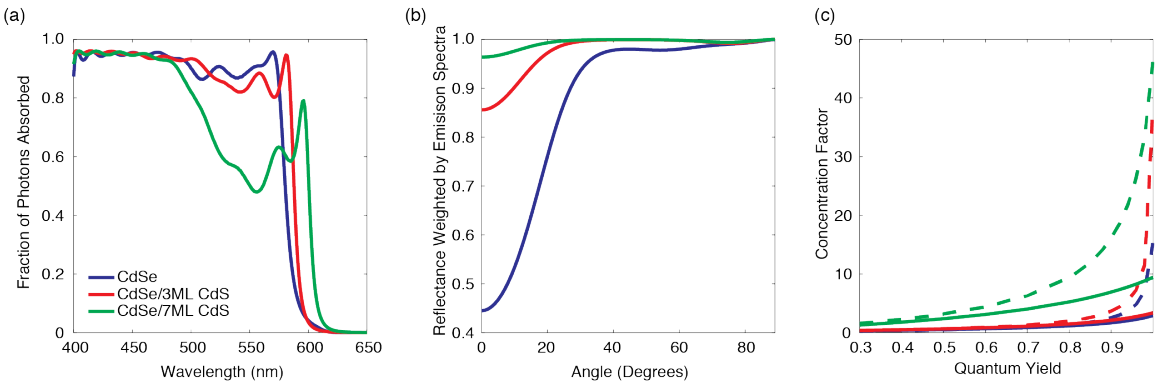

Figure 4.8: Comparison of optimum aperiodic mirrors for concentrators with CdSe-based luminophores. (a) The fraction of incident light absorbed as a function of wavelength. (b) The reflectance of the mirror as a function of angle is weighted over the emission spectrum of the luminophore. (c) The predicted performance of the concentrator is calculated using the Monte Carlo model with an open top (solid) or the aperiodic mirror (dashed). Results are compared for CdSe core nanocrystals (blue), CdSe/CdS core/shell nanocrystals with a 3 monolayer CdS shell (red), and CdSe/CdS core/shell nanocrystals with a 7 monolayer CdS shell (green).

Therefore, designing spectrally-selective mirrors for materials with significant overlap between absorption and emission spectra requires emphasis on improving the absorption efficiency of the concentrator as opposed to the trapping efficiency. This will allow for only modest improvements over the open top designs shown in Figure 4.5 (a) for quantum yields near 0.9. However, for luminophores with significant Stokes shifts and low overlap between the absorption and emission bands, introducing a spectrally-selective mirror leads to significant performance enhancements across a wide range of quantum yields. As reabsorption losses become less significant, escape cone losses dominate the loss pathways, making trapping designs more critical. Nevertheless, this result indicates that it is important to consider the dominant loss pathways to determine if the introduction of spectrally-selective mirrors will lead to significant performance enhancement.

4.4 Conclusions

A series of spectrally-selective, top surface mirrors were designed to favor different scenarios, including the transmission of sunlight into the concentrator and the omnidirectional

reflection of luminescent light for trapping within the concentrator. Figure 4.9 outlines the major conclusions we found from this study, namely that mirrors that prioritize incident sunlight transmission are favored when the concentrators have a high loading fraction of luminophores, when the concentrators are small, or when there is significant overlap between the absorption and emission spectra. The emission weighted mirrors result in higher performance at higher quantum yields, when the concentration of the luminophores is lower, the lateral size is larger, or there is low overlap between the absorption and emission bands of the luminophore. These emission weighted mirrors lead to the highest overall concentration factors found, as they are favored at conditions where there are significant photon recycling events that keep light trapped within the concentrator. The guidelines here could also be applied to other materials systems to improve the performance of LSCs with non-ideal luminophore properties.

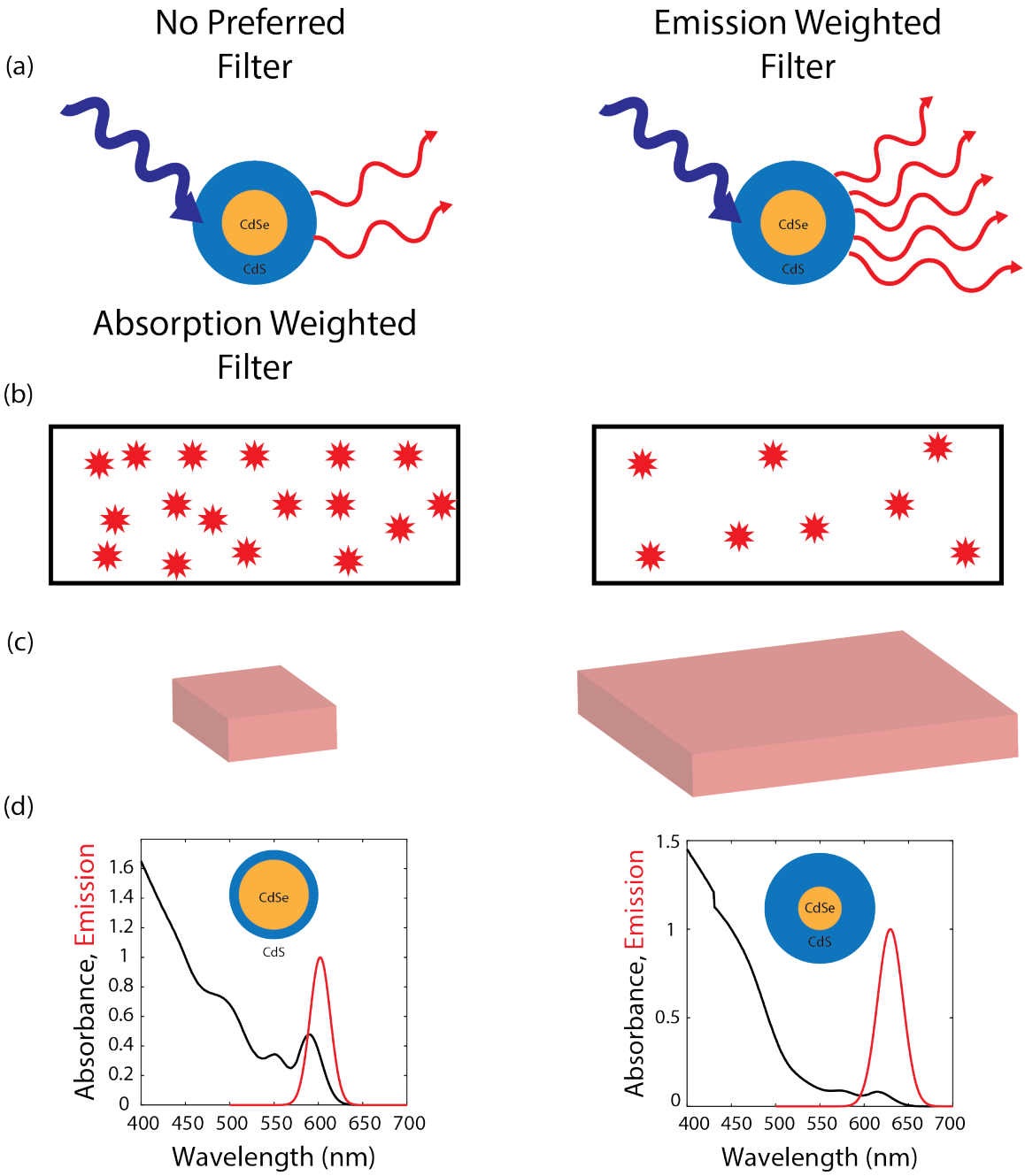

Figure 4.9: Summary of preferred mirrors for different designs of the LSC. (a) When the quantum yield is low, either mirror provides benefit. At high quantum yields, the emission weighted mirror offers greater benefits. (b) The choice of mirror depends on the concentration of luminophores in the slab, with the emission weighted mirror preferred at low concentrations. (c) The emission weighted mirror is also favored at large lateral sizes. (d) Luminophores with significant overlap need mirrors with more transmission, whereas mirrors with little overlap show better performance with the emission weighted mirror.

Chapter 5

Integrating Photonics with Luminescent Solar Concentrators: Optical Transport in the Presence of Photonic Mirrors

5.1 Introduction

High performance LSC operation necessitates both high quality luminescent downshifters and efficient light guiding to the adjacent solar cell. A recent resurgence in research in LSCs has been driven by the synthesis of highly performing downshifting materials based on luminescent nanocrystals [19, 20, 23, 24, 121]. These quantum dot nanocrystals meet many of the criteria for ideal luminophores, including high quantum yields, tunable absorption and emission, and resistance to photobleaching. In this chapter we specifically focus on quasi-type-II band aligned core/shell heterostructures, as this is a common nanocrystal materials platform that has been synthesized with quantum yields as high as 97% for heterostructures with thin shells and 86% for heterostructures with thick shells [24,112]. These nanocrystals have also been synthesized with narrow emission bandwidths making them good candidates for combination with the photonic architectures that will be discussed later [1]. Nevertheless, the quantum yield of these nanocrystals may be reduced when integrated into the polymer matrix, and similar materials with large Stokes shifts and diminished toxicity are potential replacements [13,122]. Additional light harvest-

ing benefits for single junction LSCs are also expected if longer wavelength luminophores are used, but we focus here on the CdSe/CdS combination because it is commonly studied and could be integrated with III-V solar cells.

However, even if highly performing nanocrystals are integrated into LSCs, performance will be limited by optical transport. To address this problem, the goal of this chapter is to understand optical transport in the presence of different photonic structures, as designed for LSCs that utilize luminescent nanocrystals. The emission spectrum of the luminescent nanocrystals is typically narrower than dyes, making them particularly suitable for combination with photonic structures of limited bandwidth [25]. Recent results have shown that the combination of wavelength-selective Bragg mirrors on the top interface with these nanocrystals results in high concentration factors for solar cells mounted in the middle of the LSC, enabled by a reduction in escape cone losses [1, 25, 55]. These devices can produce very high concentration factors, but also require high quantum yield nanocrystals and nearly perfect mirrors to translate the trapped light to the solar cell. Other recent proposals to improve light guiding include integrated photonic crystals, 3D opal structures, aligned luminophores to control the angle of emission, and others [2, 54, 123–126].

This chapter uses modeling to study the specific case of optical transport in LSCs that incorporate Bragg mirrors on the top surface, first showing that for operation over sufficiently large areas it is important to couple the luminescent light into guided modes with significant lateral propagation. The influence of different types of back reflectors on the conversion efficiency is then studied, and design guidelines for the use of phase shifting mirrors to force trapped light to propagate toward the adjacent solar cell are identified. These cases are then evaluated for non-ideal luminescent nanocrystals and imperfect mirror reflectivity.

5.2 Methods

A ray-tracing Monte Carlo code is used to calculate the propagation of light throughout the LSC, and to track the outcome of every incident photon [1, 127]. The LSC consists of a polymer waveguide with refractive index of 1.49 and an overall thickness of 150 μm, where the middle 75 μm of this layer is filled with CdSe/CdS core/shell heterostructures loaded at an optical density of 0.8 (Figure 5.1 and Figure 5.2). The emission spectrum of these nanocrystals is maximized at 598 nm, with a bandwidth of approximately 31 nm. The refractive index of the polymer-nanocrystal composite is assumed to be equal to the polymer alone, which is a reasonable assumption at the loading fractions studied here [61]. The solar cell is mounted to the right side face of the waveguide and specular mirrors are mounted to the other side faces of the waveguide with a 10 μm air gap between the polymer and mirror. Unless stated otherwise, the mirror reflectivity is set to 0.99. A quantum yield of 70% is typically assumed, which has been achieved in CdSe/CdS quantum dot and polymer composites, but is also significantly lower than the solution-phase quantum yields [24, 25]. This assumption allows for a comparison of photonic architectures when the quantum dot has significant non-radiative loss. In this study, emphasis is placed on guiding photons to a face mounted solar cell, and, as such, it is assumed that the interface between the solar cell and the LSC transmits light into the solar cell with unity efficiency. No other properties of the solar cell are assumed, as collection is defined only as light that reaches the edge of the concentrator. Sunlight is simulated with wavelengths ranging from 330 nm to 700 nm, incident over a range of injection positions on the top surface. The spacing of this grid is dependent on the size of the top face so that 641,601 photons are injected with equal spacing over the top face for each wavelength.

The concentration factor C for the LSC is given by $C = \eta G$, where G is the geometric concentration factor and η is the optical efficiency, or the fraction of incident photons that reach the edge of the solar cell. To compare structures, we focus on maximizing η and keep

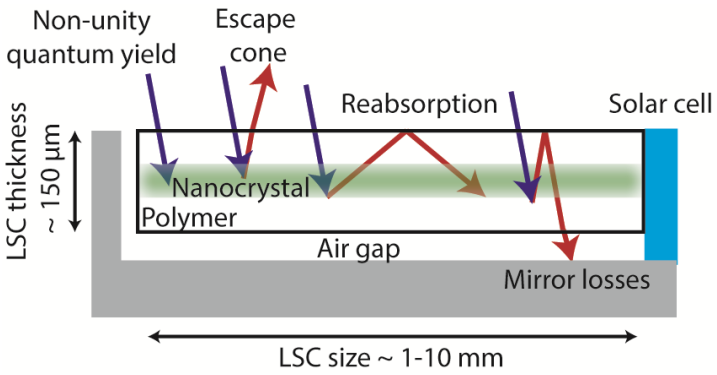

Figure 5.1: Schematic showing loss mechanisms of a luminescent solar concentrator. The green layer in the polymer waveguide is the nanocrystal-embedded layer. In this geometry the solar cell is mounted to the right face of the polymer waveguide (n=1.49). Mirrors surround the front/back, left, and bottom faces of the waveguide separated by a 10 µm air gap.

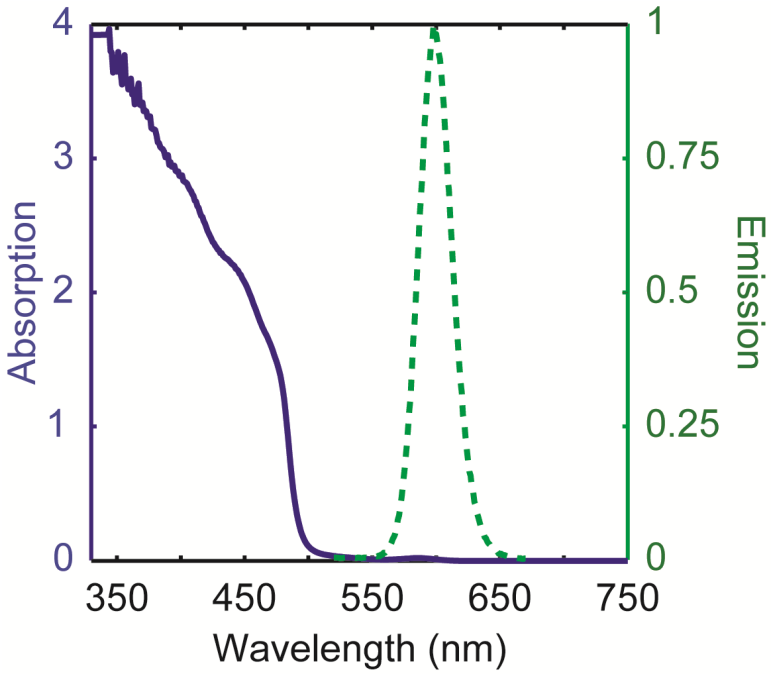

Figure 5.2: (solid) Absorption and (dashed) normalized emission spectra of CdSe/CdS dot-in-rod heterostructures. The nanocrystal properties are derived from Reference [1].

G fixed, since G is defined by the ratios of the sizes of the solar cell and of the concentrator.

5.3 Results and Discussion

In an ideal LSC, all of the incident sunlight is absorbed, re-emitted at a longer wavelength with unity quantum yield, and then trapped via total internal reflection (TIR) until it collected by the solar cell. Figure 5.1 outlines some of the loss mechanisms that prevent ideal operation, including initial absorption losses due to non-unity quantum yield, reabsorption losses, losses to the escape cone, and losses to the mirrors along the edges. The first depends on the synthesis of the nanocrystals and the embedding of the nanocrystals in the polymer matrix, whereas the latter three depend on the optical transport within the system. In particular, reabsorption losses depend on both the Stokes shift of the nanocrystal and the pathway of the emitted light through the LSC. Other losses that are not depicted in this figure include reflection off the top interface and photons that are not absorbed in two passes through the LSC and are subsequently reflected out of the waveguide. These losses are counted separately in the model.

The escape cone and mirror losses are strongly dependent on the optical transport within the LSC. Escape cone losses occur when light is emitted at an angle $\theta < \theta_c$, where θ_c is the critical angle for TIR within the polymer and the angles are defined with respect to normal incidence. The critical angle for a polymer with index of 1.49 and air is approximately 43°. This loss mechanism can be suppressed with the addition of a wavelength-selective mirror, such as a Bragg reflector, on the top interface. These mirrors are designed to accept sunlight within the absorption band of the semiconductor into the LSC, and to trap the luminescent light that would otherwise couple out of the LSC. In the system considered here, the sides of the LSC that do not contain the solar cell and the bottom face are covered with mirrors, separated from the LSC by an air gap. The purpose of the air gap is to reduce mirror losses: photons trapped in TIR modes never interact with the mirror because they are reflected at the polymer/air gap interface and trapped inside the polymer waveguide. The only light that interacts with the bottom mirror is therefore light that falls within the angular range

$-\theta_c < \theta < \theta_c$.

Figure 5.3 shows the results of calculations comparing the optical efficiency η and losses in an LSC with an open top to one that includes a Bragg reflector. The characteristics of the Bragg reflector are described in Figure 5.4. The LSC modeled in Figure 5.3 is 1 mm x 1 mm, which although smaller than a realistic LSC serves as a reasonable starting point for understanding the origin of the losses inside the system. A diffuse mirror is mounted to the bottom face of the luminescent solar concentrator separated from the polymer by a 10 μm air gap. The fraction of incident photons of varying wavelength that reach the solar cell is shown in Figure 5.3 (a), along with the fraction of photons lost to the escape cone, to reabsorption, and to the mirrors along the edges (Figures 5.1 (b) - (d)).

In general, the optical efficiency is high where the CdS is absorbing ($\lambda < 500$ nm), and small but non-zero at wavelengths longer than the bandgap. This arises from the mirrors surrounding the LSC, as a small fraction of incident photons are directed onto the solar cell without undergoing the absorption and emission process. Significantly higher optical efficiency is predicted for the Bragg mirror than the standard LSC. At wavelengths shorter than 500 nm, this enhanced performance is due to a reduction in coupling to the escape cone (Figure 5.3 (b)). At wavelengths longer than 500 nm, the Bragg mirror is more effective because it traps incident light that falls within its reflection band. While there is significant reflection off the top surface for photons incident at wavelengths over the emission band of the nanocrystal, any of this sunlight that does enter the LSC will be trapped by the Bragg mirror and directed toward the solar cell (Figure 5.4).

Although the LSC containing the Bragg mirror suppresses escape cone losses, it has slightly higher reabsorption and mirror losses. These observations are consistent with the optical transport in the presence of a Bragg mirror. This design does not guide the emitted photons into the total internal reflection modes; it merely traps the photons that fall in the angular range $-\theta_c < \theta < \theta_c$ within the LSC. Photons with angles close to normal incidence

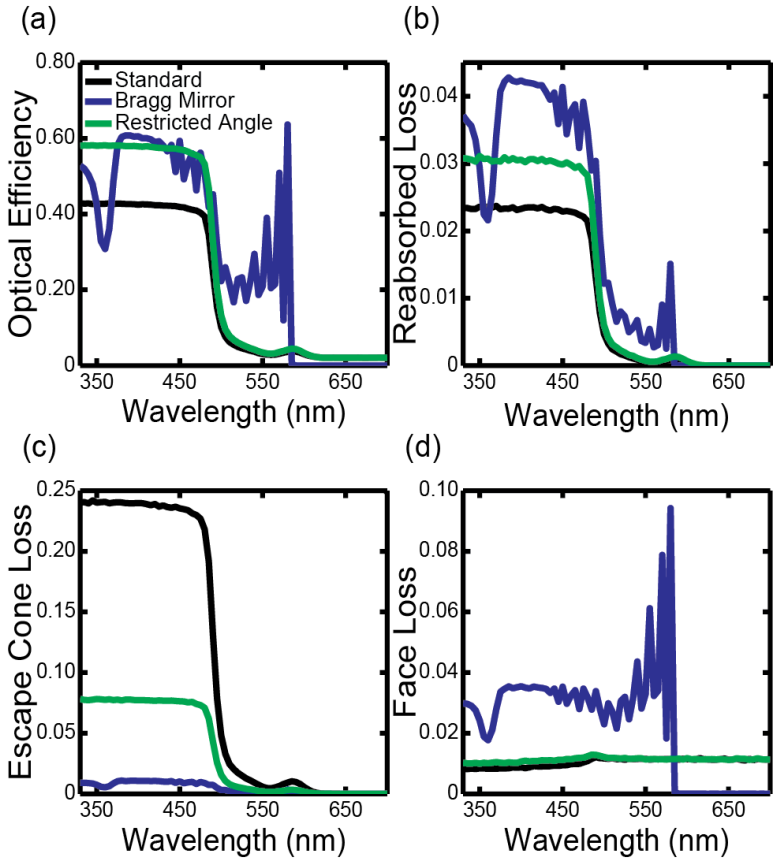

Figure 5.3: Monte Carlo ray-tracing simulations showing optical efficiency (a) and loss mechanisms ((b) - (d)) as a function of wavelength. Panel (b) shows the reabsorption loss, (c) the escape cone loss, and (d) the total mirror loss due to both the side and bottom mirrors. Results are shown for a standard LSC (black), one including a Bragg mirror on the top face (blue), and one where the angle of emission of the luminophore is restricted to couple into the TIR modes (green). The LSC size is 1 mm x 1 mm.

propagate short lateral distances, reflecting off of the Bragg mirror and the bottom diffuse mirror many more times before reaching the solar cell and resulting in increased reabsorption and mirror losses compared to the light in TIR modes. To illustrate this difference, calculations are shown in Figure 5.3 for luminescent materials with a restricted angle of emission, such that every emission event produces $\theta > 45°$ or $\theta < -45°$. This assumption couples all emitted light into TIR modes, making the difference between the two calculations the light that would otherwise be in the escape cone. As seen in Figures 5.3 (b) and (d), restricting the angle of emitted light to fall within the TIR angles reduces losses to re-

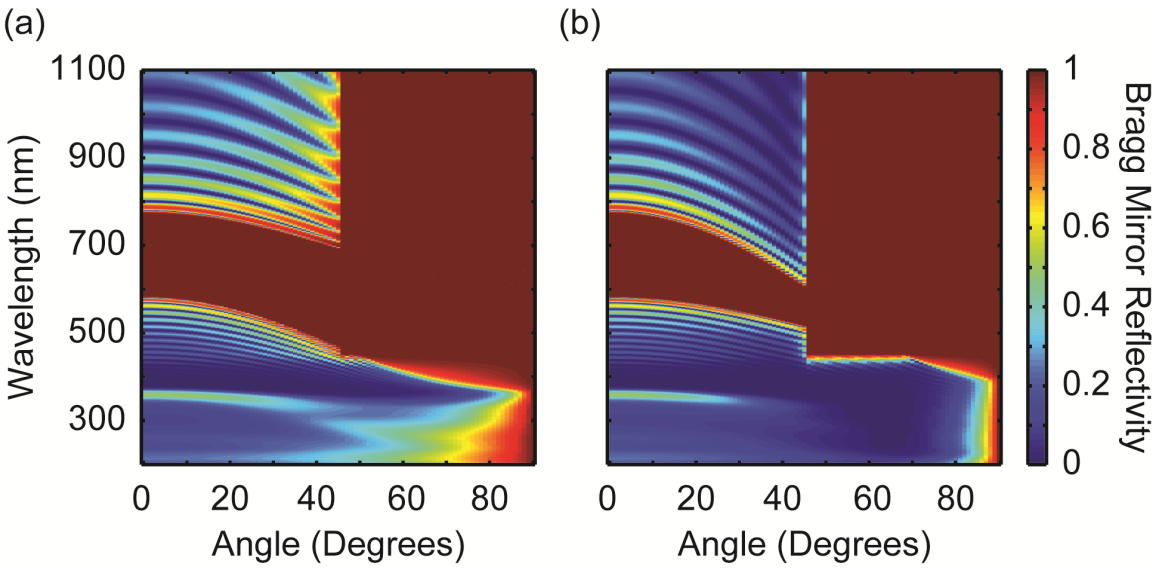

Figure 5.4: Probability of reflection from a 1D Bragg mirror for (a) s and (b) p polarized light. The bandgap of the Bragg mirror is tuned to match the emission spectrum of the heterostructures from Figure 5.2. The properties of the Bragg mirror are derived from Reference [1].

absorption and the faces relative to the Bragg mirror, consistent with the smaller number of reflection events needed to reach the solar cell. The escape cone losses are slightly higher, since in this case there is no Bragg reflector on top, and it is possible for light that reaches the sides to be coupled out of the LSC.

Figure 5.5 compares the optical efficiency and loss mechanisms as a function of the size of the LSC, up to a 10 mm x 10 mm device. Results are shown for the LSC with all emission directed into TIR modes (Figures 5.5 (a) - (d)), and the LSC including the Bragg mirror (Figures 5.5 (e) - (h)). The expectation is that with increasing size, optical transport is a more limiting factor, and so the divergence should be greater between the Bragg mirror LSC and the case where all light is coupled into TIR modes. Indeed, although the optical efficiency of both decreases with increasing size, the reduction in optical efficiency occurs more rapidly for the Bragg mirror than the case with all light in TIR modes (Figures 5.5 (a) and (e)). The Bragg mirror is also more affected by the reabsorption losses, although both systems show an increase in these losses with increasing size (Figures 5.5 (b) and (f)). The escape cone losses are considerably higher for the case where all light is in TIR modes, but

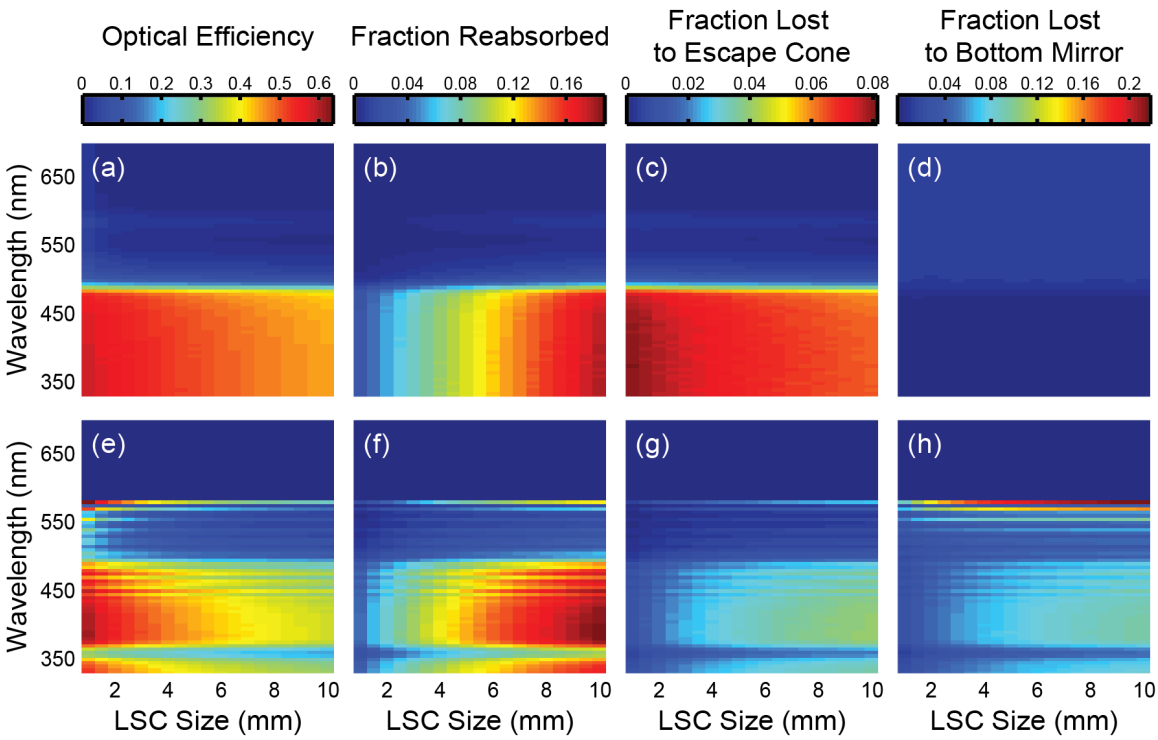

Figure 5.5: Predicted LSC performance as a function of lateral size from 1 mm to 10 mm where the angle of emission is restricted to the TIR angles ((a) - (d)) and where a Bragg mirror is included ((e) - (h)). The performance metrics shown are optical efficiency ((a) and (e)), reabsorption loss ((b) and (f)), escape cone loss ((c) and (g)), and bottom mirror loss ((d) and (h)).

decreases with increasing size, as opposed to the Bragg mirror that has a slight increase in escape cone loss as the structure gets larger (Figures 5.5 (c) and (g)). And finally, the Bragg mirror has increasing loss in the bottom mirror as the size increases (Figure 5.5 (h)). When all light is in the TIR modes, no photons interact with the bottom face mirror, making these losses negligible (Figure 5.5 (d)).

In this system the sides of the LSC are covered with mirrors rather than additional solar cells (Figure 5.1), and η represents the fraction of incident photons that propagate to one edge. Another version of this device would mount solar cells to all of the adjacent sides, necessitating only collection from a portion of the collector. In terms of the effect on a single solar cell, placing mirrors on the other sides is similar to having devices on the other sides with high radiative efficiency. In consideration of this type of layout, Figure 5.6

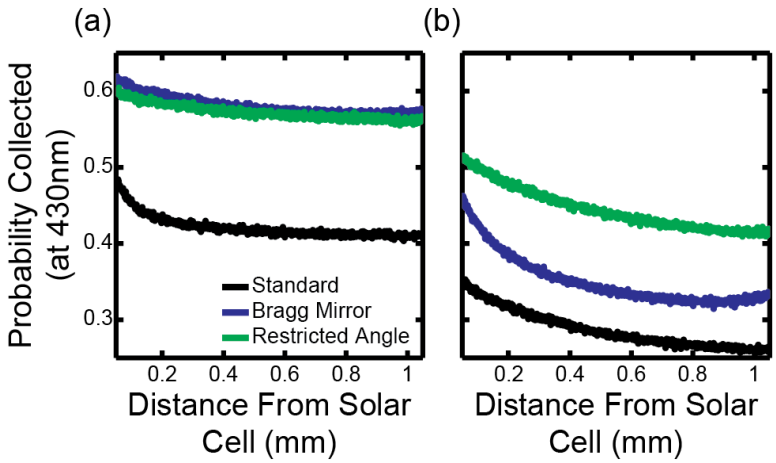

Figure 5.6: Optical efficiency as a function of distance from the solar cell for the standard LSC (black), the LSC with a Bragg mirror (blue), and the LSC where all the luminescence is restricted to the TIR angles (green). In (a) the LSC is 1 mm x 1 mm, and in (b) the LSC is 10 mm x 10 mm.

shows the optical efficiency for the different devices as a function of distance away from the side containing the solar cell. The calculations are shown for incident sunlight with a wavelength of 430 nm, which is within the absorbing region of the CdSe/CdS core/shell particle spectrum, and at LSC sizes of both 1 mm x 1 mm (Figure 5.6 (a)) and 10 mm x 10 mm (Figure 5.6 (b)). For each position, the simulation is run 50 times, and the results are averaged. In the smaller concentrator there is a rapid decrease over the first 100 μm for all three devices. In the larger concentrator there is a slight decrease in for both the standard LSC design and the case where all light is in TIR modes, since as the distance increases the reabsorption losses increase.

Interestingly, the Bragg mirror design does not show a steady decrease with increasing distance from the edge. This anomalous phenomenon is visualized by simulating photons near the opposite side face of the luminescent solar concentrator and tracing the position. Emitted photons near the opposite edge of the LSC can reflect off the Bragg mirror on the top surface, reflect off the mirror on the edge opposite from the solar cell after traveling through the air gap, and re-enter the polymer waveguide in a total internal reflection mode. Photons in total internal reflection modes are much more likely to be collected by the solar

cell, which increases the total fraction collected at that distance for the Bragg mirror simulation. This supports the evidence from earlier simulations: it is insufficient to merely trap light inside the LSC, but instead light must couple into modes with sufficient propagation to have high probability of collection by an edge-mounted solar cell.

One potential solution to this problem is to integrate phase shifting mirrors that anomalously reflect incident light, as recently demonstrated with plasmonic metasurfaces [128, 129]. When light reflects off a phase shifting mirror, the reflected light is phase shifted and obeys the generalized law of reflection $\sin\theta_r - \sin\theta_i = \frac{1}{n_i k_0}\frac{d\phi}{dx}$, where θ_r is the angle of reflection, θ_i is the angle of incidence, n_i is the refractive index on the incident side, k_0 is the free space wavevector, and $\frac{d\phi}{dx}$ is the gradient of the phase [130]. If the phase varies linearly, then $\frac{d\phi}{dx}$ is a constant, which adds a parallel wavevector to the incident wavevector. The angle of reflection can therefore be written as $\theta_r = \sin^{-1}\left(\sin\theta_i + \frac{\Delta k_x}{n_i k_0}\right) = \sin^{-1}(\theta_i + \delta)$ [130].

This also predicts that for $\theta_i \geq \sin^{-1}(1-\delta)$ light will be coupled into a surface bound mode that propagates along the interface. Therefore with an appropriate choice of δ, as determined by the nanostructures used on the mirror to impart a phase shift, the reflected light can be steered toward desirable angles in accordance with the generalized law of reflection.

For our purposes, there are a few constraints on the desirable parameters of the phase shifting mirror. First, coupling into a surface bound mode is undesirable, as this would likely lead to higher losses to the bottom face mirror rather than efficient propagation toward the edge-mounted solar cell. Fortunately many phase shifting mirror designs are inefficient at higher angles of incidence, and exhibit specular reflection rather than anomalous reflection. To understand the upper limits of the design, we apply the assumption that light is not coupled into surface bound modes at high angles of incidence, but is instead reflected specularly. We also assume that this phase shift only needs to occur over the bandwidth of

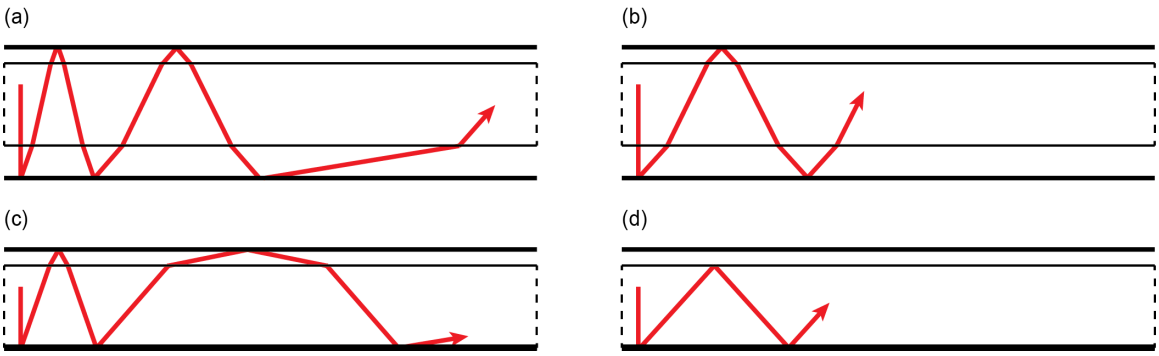

Figure 5.7: Schematic showing the path of a normally incident photon through a luminescent solar concentrator with a phase shifting bottom mirror. The structures in (c) and (d) are without an air gap, and (a) and (b) include an air gap. The two columns represent two different values of δ, $\delta = 1 - \frac{1}{1.49} = 0.33$ ((a) and (c)) and $\delta = \frac{1}{1.49} = 0.67$ ((b) and (d)).

the emission of the luminophores, so a broadband phase shifting mirror is not necessary. Notably this system is somewhat different than light trapping for solar cells accomplished with phase shifting mirrors, as the goal here is to couple light into the modes with the most significant propagation [130, 131].

The idea is illustrated schematically in Figure 5.7, for the cases where the phase shifting mirror is applied directly on the bottom of the LSC and when it is separated by an air gap. The schematic is shown for light of normal incidence, but similar arguments apply for off-normal incidence as well, and illustrations are shown for $\delta = 1 - \frac{1}{1.49} = 0.33$ and $\delta = \frac{1}{1.49} = 0.67$. Figure 5.8 shows the assumed dependence of the reflected angle on the incident angle. Considering the case without the air gap first, light of normal incidence ($\theta_1 = 0°$) hits the bottom mirror and is reflected with a phase shift at a new angle of reflection $0° < \theta_2$. The light then propagates back through the LSC until it reflects off the top Bragg mirror specularly, and is reflected back to the back mirror with $0° < \theta_2$. This results in another phase shift, such that the angle of the light when it is refracted back into the polymer follows $0° < \theta_2 < \theta_3$. Without an air gap, this continues until $\theta_i \geq \sin^{-1}(1 - \delta)$, in which case the light is reflected specularly. However, this gradual steering toward modes with more lateral propagation may be interrupted by reabsorption.

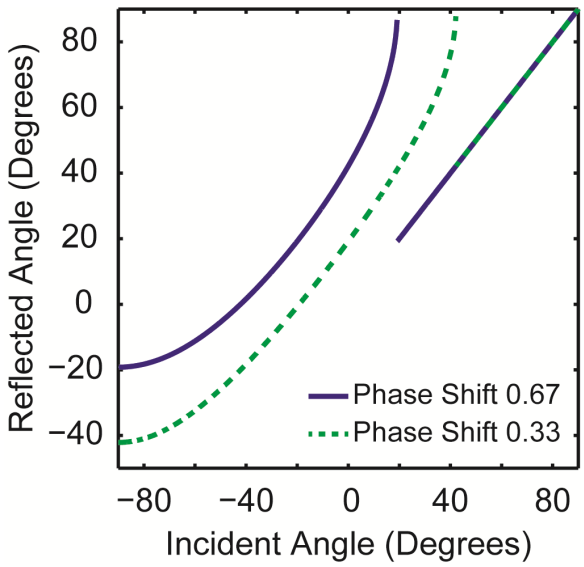

Figure 5.8: Reflected angle vs. incident angle using generalized Snells law with the assumption that if the photon would be scattered into a surface mode it is instead reflected specularly. (solid) Phase shifting mirror with a phase shift of $\frac{1}{n_{polymer}}$ 0.67. *(dashed) Phase shifting mirror with a phase shift of* $1 - \frac{1}{n_{polymer}}$ 0.33.

If at any point during the propagation through the LSC the photon is reabsorbed by the nanocrystals, then it will be re-emitted at a new angle and the phase shifting process will restart. Without an air gap, the ideal scenario is therefore to couple all light into the TIR modes, which then reflect specularly.

The optimal configuration of the phase shifting mirror changes when an air gap is included (Figures 5.7 (a) and 5.7 (b)). If an air gap is applied, then the TIR modes undergo specular reflection at the polymer/air interface and do not interact with the phase shifting mirror. The only light that is incident on the phase shifting mirror is that which falls in the angular range $-\theta_c < \theta < \theta_c$. The air gap is beneficial since it protects the TIR modes from mirror loss, but it is also no longer possible to use the phase shifting mirror to couple light into the TIR modes. The most favorable situation is now to steer the reflection as close to the critical angle of the polymer as possible. This favors a small δ, as it is better to gradually steer all the light toward this angle, and for reflection to only become specular at very oblique angles of incidence. Of course if the phase shift is too small then the phase

shifting mirror behaves as a specular mirror, and the advantage of the phase shift is lost.

Figure 5.9 shows a comparison of optical efficiency and losses for LSCs containing different bottom face mirrors as a function of mirror reflectivity, both with and without air gaps. The resulting spectral optical efficiency and losses are weighted by the solar spectrum over the region where the LSC is absorbing (330 - 500 nm), and the full spectral characteristics are given in Figure 5.10). The LSC is 10 mm x 10 mm. For simplicity the mirror reflectivity is assumed to be constant at all wavelengths. Results are also shown for a specular mirror of the same reflectivity and a diffuse mirror that scatters light with equal probability per solid angle. A Bragg mirror is present on the top interface in all cases.

Comparing the predictions for the standard mirrors first, the specular mirror has higher optical efficiency than the diffuse mirror. This is a consequence of including the Bragg mirror on the top surface. With a diffuse mirror, light at normal incidence can be scattered into modes with more lateral propagation, but the reverse process is also true. Since there are essentially no escape cone losses at the top interface, this favors the use of a specular mirror. As discussed earlier, the inclusion of the air gap is extremely important, as it reduces the effect of mirror losses. With an air gap, the light in TIR modes experiences no loss upon reflection with the back of the LSC as it never interacts with the back mirror.

Even at relatively low mirror reflectivity values, there is a significant gain from including the phase shifting mirror, although the improvement is most significant for the case without an air gap. At most mirror reflectivities the presence of the air gap is favored, but at very high reflectivities the phase shifting mirrors without an air gap become more favorable. For the case with no air gap and a phase shifting mirror, light within the range $\theta_c < \theta < \theta_c$ can be coupled into TIR modes with $\theta > \theta_c$. As long as the mirror losses are sufficiently low such that the extra reflections compared to the air gap case are tolerable, this provides an advantage as more light is coupled into propagating modes with reduced reabsorption. For the case with the air gap, the phase shifting mirror cannot convert light

into TIR modes, but it can redirect the light within the angular range $\theta_c < \theta < \theta_c$ close to θ_c. This improves the propagation by reducing the number of passes through the reabsorbing nanocrystal layer and the number of interactions with the bottom mirror. These assignments are supported by Figures 5.9 (b) and 5.9 (c), which show that the phase shifting mirror leads to reduced bottom mirror losses and reduced reabsorption losses due to the minimized interaction time as the photons propagate toward the edge-mounted solar cell.

Between the two values of δ shown in Figures 5.7 and 5.9, the smaller phase shift is favored slightly, but the difference is sufficiently small to indicate that enhanced performance could be expected from a wide range of phase shifts. The best case scenario is that the light will be steered toward an angle that is less than but close to the critical angle, in order to maximize propagation and minimize interaction with both the back mirror and the reabsorbing luminescent layer. If the phase shift is too large, then the angle quickly reaches the $\theta_i \geq \sin^{-1}(1-\delta)$ condition where the mirror becomes specular, and so the final angle of the propagating beam is not close to the critical angle. If the phase shift is small, then the angle where $\theta_i \geq \sin^{-1}(1-\delta)$ is steeper, and so the light within the polymer is steered closer to the critical angle. The difficulty is that as δ decreases, it becomes similar to a specular mirror. This explanation indicates that there should be an optimal value of δ.

A variety of different phase shifting mirrors based on metasurfaces have been proposed recently for use in reflection. One commonly used approach is to create gap-plasmon structures, which have been shown to operate under both polarizations of incident light, although designs based on lower loss dielectric structures have also been demonstrated to have complete phase control [128, 130, 132, 133]. A gap-plasmon metasurface with the appropriate phase shift to serve as the mirror in this LSC is shown in Figure 5.11 calculated following the method described in [130].

The period of the repeating structure (Γ) is related to the gradient of the phase shift

0 nm	56 nm	60 nm	61 nm	62.5 nm	63 nm	64 nm	65 nm	68 nm	80 nm

Table 5.1: Width of each sub-cell

$$\frac{d\phi\left(x\right)}{dx} = \frac{2\pi}{\Gamma} = \delta nk = \frac{\delta n 2\pi}{\lambda}$$

Therefore for the case where we assume an air gap ($n = 1$), and are targeting 600 nm luminescent light and $\delta = 0.2$:

$$\Gamma = \frac{2\pi}{\delta kn} = \frac{2\pi\lambda}{\delta n 2\pi} = \frac{600\text{nm}}{0.2} = 3000\text{nm}$$

For simplicity we assume that the metal surface is dispersionless over the band of the luminescence, and has a complex refractive index of $n = -7i$. We use finite difference time domain simulations to design the structure. For a 3000 nm period, we assumed that 10 sub-cells of 300 nm would be used, each containing a nanostructure of a particular width. The full set of 10 sub-cells are designed to span the entire 2π phase shift, with each sub cell contributing $\frac{2\pi}{10}$ phase shift. Simulations were performed on the individual sub-cells to extract the phase from a variety of different nanostructure widths, then the widths were chosen to achieve linear gradation in phase over the 3000 nm unit cell. The final chosen widths are shown in Table 5.1, based on the data shown in Figure 5.12 (a).

Simulations are then performed on this structure as a function of angle of incidence, as shown in Figure 5.12 (b), which shows the fraction of power at each angle of incidence coupled to each outgoing angle of reflection. This structure is not necessarily designed to be the optimal metasurface for this application, but is an example of a metasurface that fulfills the design criteria, and becomes more of a specular mirror as the angle of incidence becomes steeper.

The key benefit of these phase shifting mirrors is that they can be used to couple propagating light into angles that reduce reabsorption losses, potentially enabling the use of

semiconductor nanocrystals with lower quantum yields. Figure 5.13 shows a comparison of the optical efficiency of the different designs discussed here as the quantum yield varies. Results are shown for the standard, open-top LSC, one with a Bragg mirror on the top surface, one with a phase shifting mirror of $\delta = 1 - \frac{1}{1.49} = 0.33$, and one where all the emitted light is coupled into the TIR modes. Adding any photonic structure to manage light leads to significantly enhanced performance, with more noticeable gain at higher quantum yields. (Figure 5.9 assumed a quantum yield of 70%). Although the example case where all light is coupled into TIR modes has the best performance, a significant enhancement is predicted when the phase shifting mirror is integrated with the Bragg mirror to redirect trapped light into modes with more lateral propagation. By integrating a phase shifting mirror and a Bragg reflector into the LSC design, a nanocrystal with a quantum yield of 76% performs as well as a nanocrystal of 84% quantum yield inside an LSC with a Bragg reflector alone, or a nanocrystal with 99% quantum yield with no photonic light trapping elements. This finding supports the idea that luminophore design is not the only component to address in creating efficient LSCs: careful optical design can compensate for non-ideal nanocrystals.

5.4 Conclusions

To achieve high performance from LSCs, it is necessary to guide the luminescent light to the solar cell while minimizing other loss pathways. This chapter considers and compares photonic architectures that trap luminescent light within the LSC, and shows that it is important to couple light into modes with significant lateral propagation. To accomplish this goal, phase shifting mirrors that redirect light according to generalized Snells law of reflection are proposed, and calculations indicate that the use of these mirrors would lead to significantly higher concentration factors. For a quantum yield of 70% and mirror reflectivity of 0.99, concentration factors of up to 16.1 are achievable for LSCs utilizing phase shifting and Bragg mirrors compared to 12.8 for the standard LSC geometry. Here

the phase shifting mirror is robust to small variations in the gradient of the phase, does not need to be broadband or isotropic, and can lead to performance enhancement even with significant reflectivity loss. These results indicate that the use of phase shifting mirrors could have significant benefits for the use of lower quality or imperfect luminescent materials, while still enabling high concentration factors.

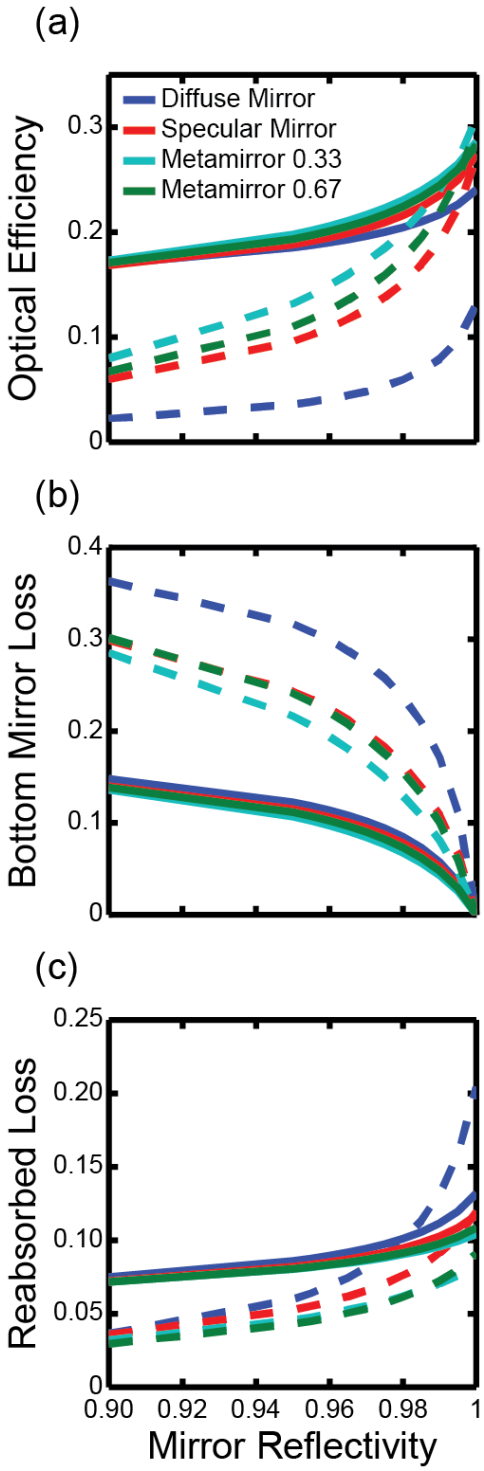

Figure 5.9: Solar spectrum weighted optical efficiency (a), bottom mirror loss (b), and reabsorption loss (c) as a function of mirror reflectivity. The solid lines include an air gap and dotted lines do not. Four different types of mirrors are compared: a diffuse mirror (dark blue), a specular mirror (red), and the two phase shifting mirrors. The solar spectrum is weighted over the absorption of the luminophore, from 330 - 500 nm.

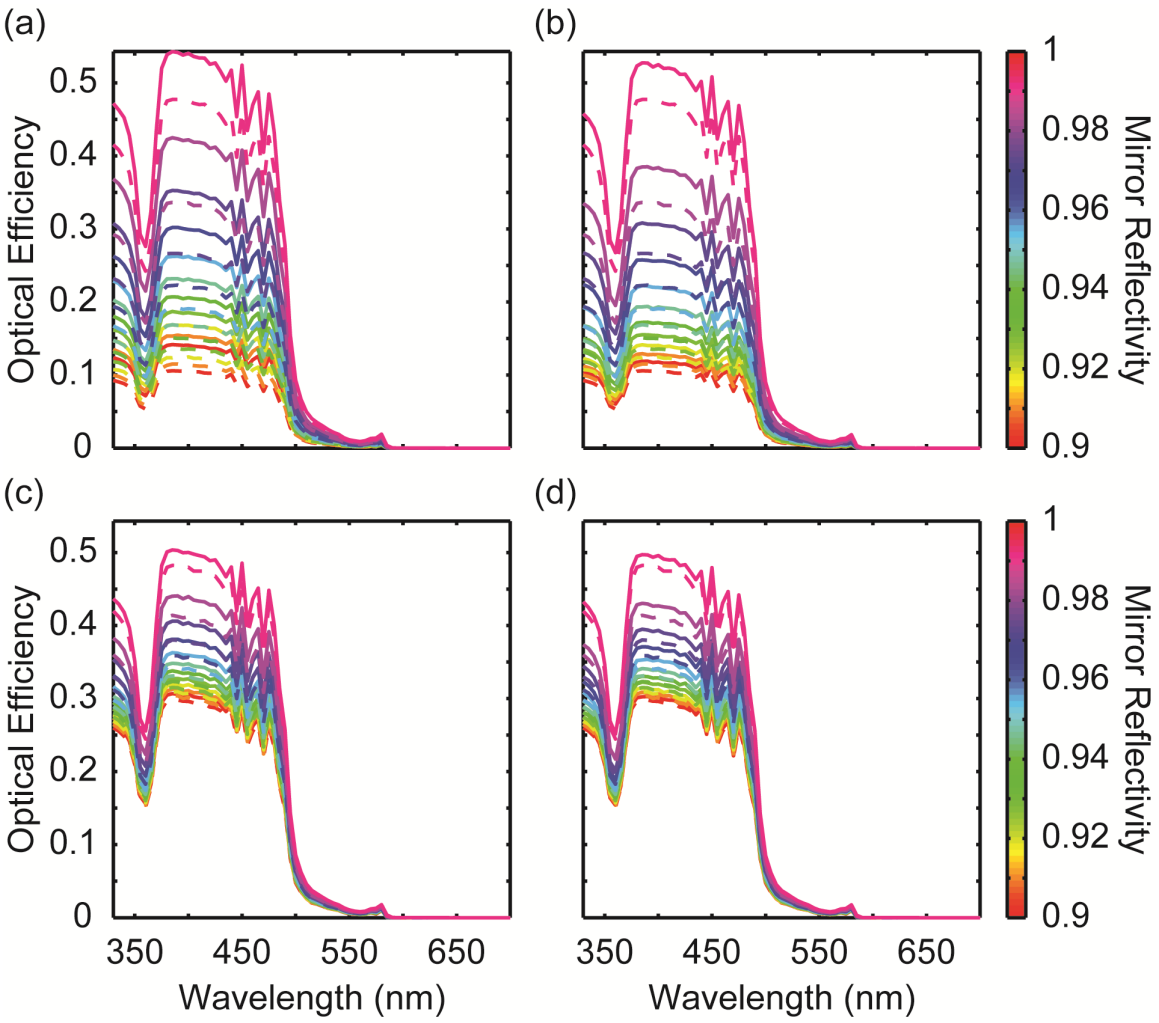

Figure 5.10: Comparison of optical efficiency between (solid) phase shifting mirror and (dashed) specular mirror for varying mirror reflectivity. (a) Phase shifting mirror with phase shift of 0.33 and specular mirror without an air gap between the polymer waveguide and bottom mirror. (b) Phase shifting mirror with phase shift of 0.67 and specular mirror without an air gap. (c) Phase shifting mirror with phase shift of 0.33 and specular mirror with a 10 μm air gap between the polymer waveguide and bottom mirror. (d) Phase shifting mirror with phase shift of 0.67 and a 10 μm air gap.

Figure 5.11: Schematic of a metasurface mirror, with the widths given in Table 5.1. The dielectric layer has a thickness of 5 nm, and each metal block is 10 nm tall.

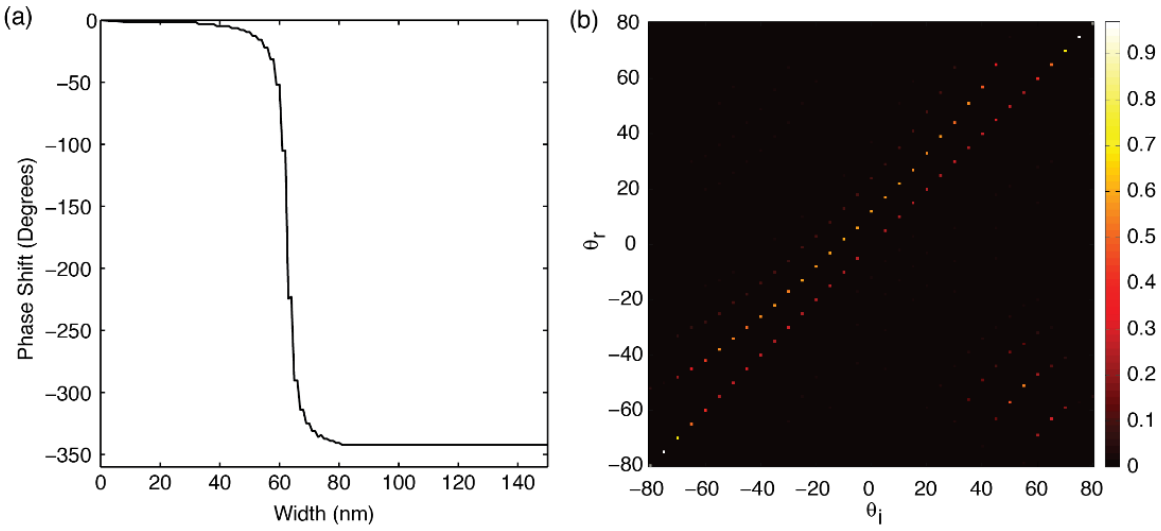

Figure 5.12: (a) Calculated phase shift at different widths of the top metal block, calculated in 300 nm unit subcells. (b) After a full array is designed consisting of 10 sub-cells, each containing a single nanoblock with the width in the table, the array is 3000 nm in length. This calculation shows the incident angle and reflected angle, with the fraction going into each angle represented by the color axis.

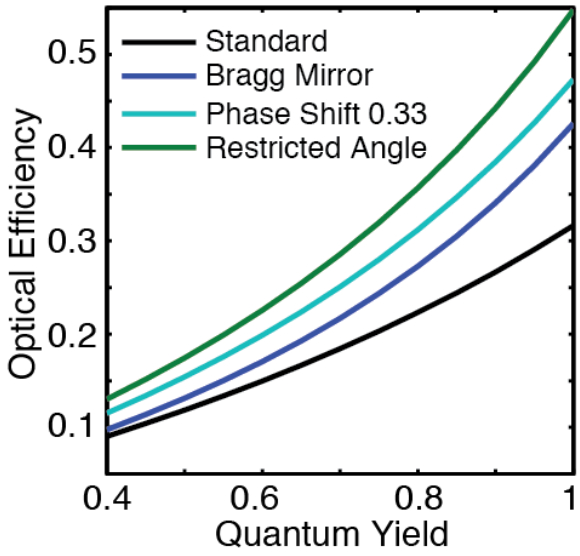

Figure 5.13: Solar spectrum weighted optical efficiency as a function of luminiophore quantum yield for different mirrors. An air gap is included between the polymer and the mirrors.

Chapter 6

Modifying the Angle of Emission from Luminophores Using Alternating High and Low Refractive Index Layers

6.1 Introduction

Chapters 4 and 5 showed the increase in concentration factor possible by utilizing photonic designs implemented on the top and bottom faces of the LSCs. However, the spectrally-selective mirrors and phase-gradient metasurfaces discussed earlier still do not reach the hypothetical performance of an LSC where all emitted light is coupled into TIR modes upon every emission event. This phenomenon could be realized if the angle of emission from the luminophores was controlled. This chapter will focus on photonic structures that modify the local electromagnetic environment of the luminophores to change the emission angle.

For large-area luminescent solar concentrators it can be assumed that only the light in the total internal reflection (TIR) modes will be collected by the solar cell. For a sufficiently large path length in the concentrator it is highly likely that emitted light that does not reflect off of the top and bottom faces with 100% probability will eventually be transmitted after multiple bounces. Therefore, the rate of collection of the solar cell material can be thought of as [61]

$$\frac{dJ}{d\omega} = Nf\left|\boldsymbol{d}_a(\omega)\right|^2 \frac{\pi\omega}{\hbar\epsilon_0 V}\int_{|k_\parallel|>\frac{\omega}{c}} d^3\boldsymbol{k}\int_{V_t} dV\left|\boldsymbol{E}_k^{*(T)}(\boldsymbol{r},\omega)\right|^2 \delta\left(\omega-\omega_k\right)$$

This equation can be broken down into the product of the concentration of the excited luminophores, the overall electric dipole moment of the luminophore at a given frequency, and the photonic local density of states (LDOS) of the TIR modes averaged over the volume of the waveguide core. In this equation N is the number of luminophores, f is the fraction of luminophores in the excited state, $\boldsymbol{d}_a(\omega)$ is the dipole strength, $\boldsymbol{k}$ is the wavevector, V is the volume, and $E_{\omega k}^{*(T)}$ is the normalized electric field profile. In the case where the LSC has the same type of luminophore and number of excited luminophores this equation shows that the rate of collection by the solar cell will be directly related to the photonic LDOS.

The photonic LDOS is defined as [61]

$$LDOS(\omega,\boldsymbol{r},\boldsymbol{d}) = -\frac{2}{\pi}n(\boldsymbol{r})^2\frac{\mathrm{RE}\left[\boldsymbol{E}(\boldsymbol{r},\omega)\cdot\boldsymbol{p}^*(\boldsymbol{r},\omega)\right]}{\left|\boldsymbol{p}(\boldsymbol{r},\omega)\right|^2}$$

where n is the refractive index of the surroundings, $\boldsymbol{E}$ is the transient electric field, and $\boldsymbol{p}$ is an arbitrary excitation pulse spectrum. Therefore, the refractive index of the surroundings can have a large impact on the photonic LDOS and by tuning the refractive index of the surroundings with nanophotonic designs it is possible to tune both the wavelength of emission [59, 60] and the angle of emission [2, 61, 123]. For example, [2] modifies the photonic LDOS by placing a luminophore embedded layer within a Bragg stack (Figure 6.1). This design significantly improves light guiding over a small spectral range as the emission from the luminophores in this region is highly directional into the total internal reflection modes.

These nanophotonic cavities can significantly improve the light guiding in LSCs by controlling luminophore emission into total internal reflection modes. However, for most of these designs the luminophore embedded layer has a thickness that is also on the order of the wavelength of light, which is much thinner than the thickness of most bulk con-

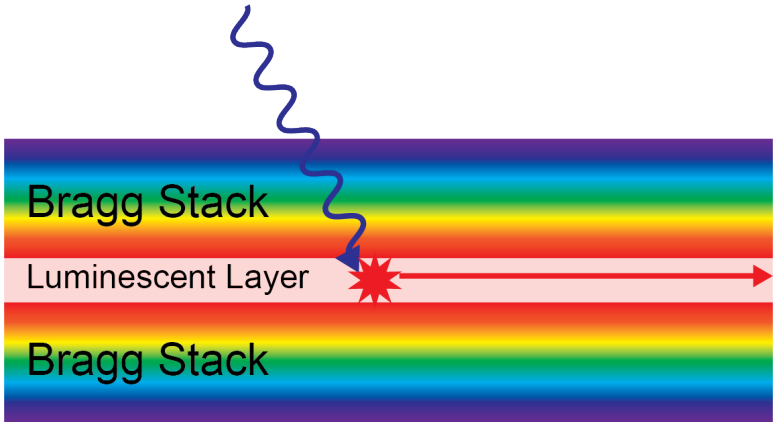

Figure 6.1: Schematic of photonic LSC used in [2].

centrators. This will reduce the absorption efficiency of the LSC unless the layer has an extremely high loading fraction, which will reduce overall LSC concentration factor. To address this problem, I designed an LSC where luminophores are directly embedded into one of the two sets of layers that make up the Bragg stack. Using FDTD simulations I studied how different properties of the photonic LSC affected the light guiding within the concentrator.

6.2 Methods

A nanostructured stack LSC was designed using a 1D Bragg stack as its basis as seen in Figure 6.2. In this design 10 alternating pairs of high (red) and low (blue) refractive index layers are stacked to form the 1D Bragg structure with one extra layer of high or low refractive index for simulations when the luminophores are in the low or high refractive index layer respectively. The high refractive index material is modeled after titania and defined with a refractive index of 2.3 over the wavelength range. The low refractive index material is modeled after a polymer such as PMMA and defined with a refractive index of 1.5. In these simulations it was assumed that the materials were not dispersive and the loading of the luminophores into one of the two sets of layers did not significantly affect the

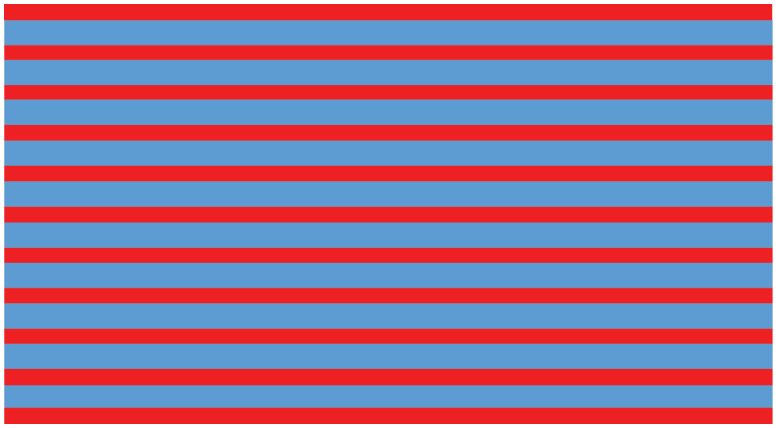

Figure 6.2: Schematic of my photonic LSC design show a stack of quantum dots embedded in polymer (blue) and titania (red) layers. The inverse layer structure is used for quantum dots embedded in the titania layer.

refractive index of the composite. The luminophore loading should not affect the refractive index of the composite as long as the loading fraction is small, which will be discussed in Chapter 7.

The thickness of the layers was chosen such that the center of the photonic band stop was found at a wavelength of 600 nm.

$$t = \frac{\lambda_d}{4n}$$

In this equation t is the thickness of the layer, λ_d is the design wavelength, and n is the refractive index of the layer.

To simulate the performance of these photonic concentrators a FDTD algorithm was used in the commercial software package Lumerical Solutions. For more information on the FDTD algorithm see Section 3.2. This software package requires the geometry of the structure, location of the monitors, refractive index models for the layers, and the mesh size used for the discretization as inputs. In these simulations two monitors were placed 860 nm above and below the photonic LSC to determine if the emitted light escapes out of the top face. The monitors must be placed a distance away from the photonic LSC that is

on the order of the wavelength of interest as that was found in preliminary simulations to be necessary to not collect evanescent waves off the photonic LSC as escaped losses. To ensure that the emitted light is given the chance to escape out of the top or bottom face the lateral size of these simulations is 15 μm, which is significantly larger than the thickness of the full stack (1.7 μm). Finally, the mesh size for these simulations is set to be 2 nm over the full simulation range so that each layer is discretized with at least 30 cells.

After defining the geometry and other simulation parameters a dipole emitter is defined in order to simulate emission from the structure. In these simulations an unpolarized dipole was placed at the middle of each of the layers of interest to predict the performance of the photonic LSC. Preliminary simulations showed no significant difference between a dipole placed at the center of the layer and one placed at different locations within the layer. After the FDTD algorithm in performed in Lumerical Solutions, the output data is collected by the monitors, which is exported to MATLAB for further processing.

6.3 Results and Discussion

Figure 6.3 shows the fraction that escapes out of the top and bottom faces for luminophores embedded in each layer within the stack. The dotted black line shows the reflectance spectrum for light incident on the photonic design at normal incidence. In this figure layer 1 is the bottom layer of the structure and layer 10 is the top layer. For luminophores embedded in the polymer layer there is one layer of titania below layer 1 and above layer 10. For luminophores embedded in the titania layer the opposite is true. Even though the fraction lost to the escape cone increases when luminophores are embedded in the layers closer to the outside of the photonic LSC there is still a spectral region for luminophores embedded in both the polymer and titania layer where the fraction in the escape cone is less than a standard concentrator of the same refractive index.

For luminophores in the polymer layer light guiding is enhanced for wavelengths greater

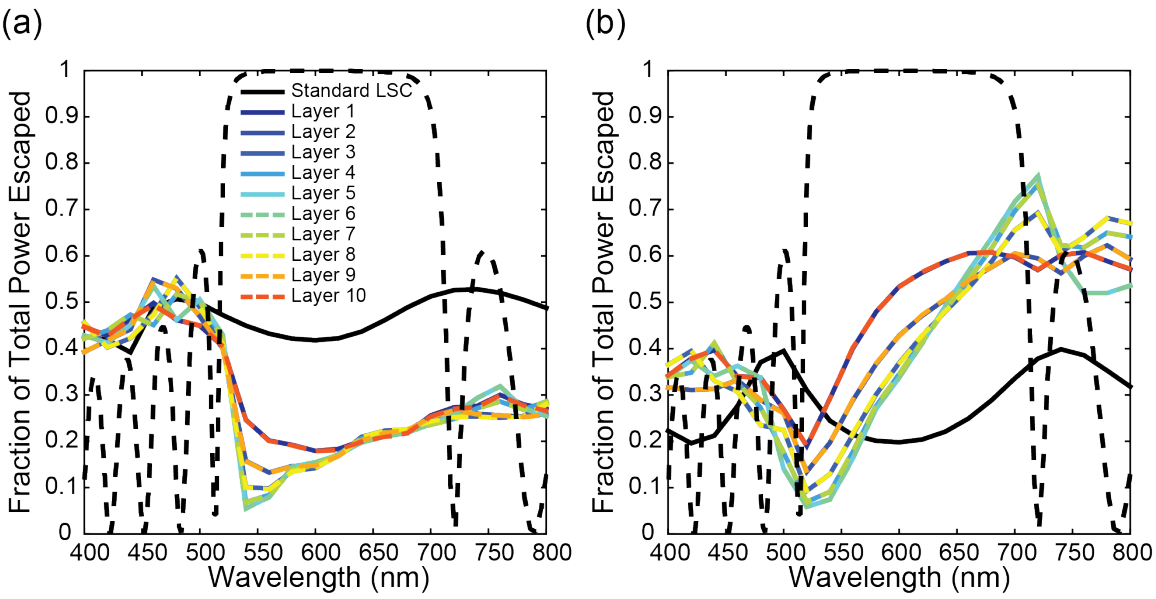

Figure 6.3: Predicted escape cone losses for a photonic LSC with luminophores embedded in the polymer (a) or titania (b) layer of the 1D Bragg stack.

than 500 nm. At its peak near the center of the structure the escape cone losses are reduced by 36% compared to the escape cone losses predicted for a standard LSC with the same refractive index as the polymer and a thickness equal to the thickness of all of the emitting layers put together. For luminophores in the titania layer the light guiding is enhanced for wavelengths between 475 nm and 550 nm. At its peak the escape cone losses are reduced by about 14% compared to a standard LSC with a refractive index of the titania layer and a thickness of all emitting layers put together. The light guiding for luminophores embedded in the titania layer is only enhanced over a small bandwidth because the fraction escaped monotonically increases through the region of the photonic band stop for luminophores in the titania layer, which does not occur when the luminophores are embedded in the polymer layer. In addition, the fraction trapped by the titania standard LSC is significantly higher than the polymer standard LSC due to the higher refractive index. Therefore, it is predicted that enhanced light guiding would only be observed for narrow band emitting luminophores embedded in the titania layer, while the luminophore could have a significantly wider emission band and still observe enhanced light guiding if embedded in the polymer

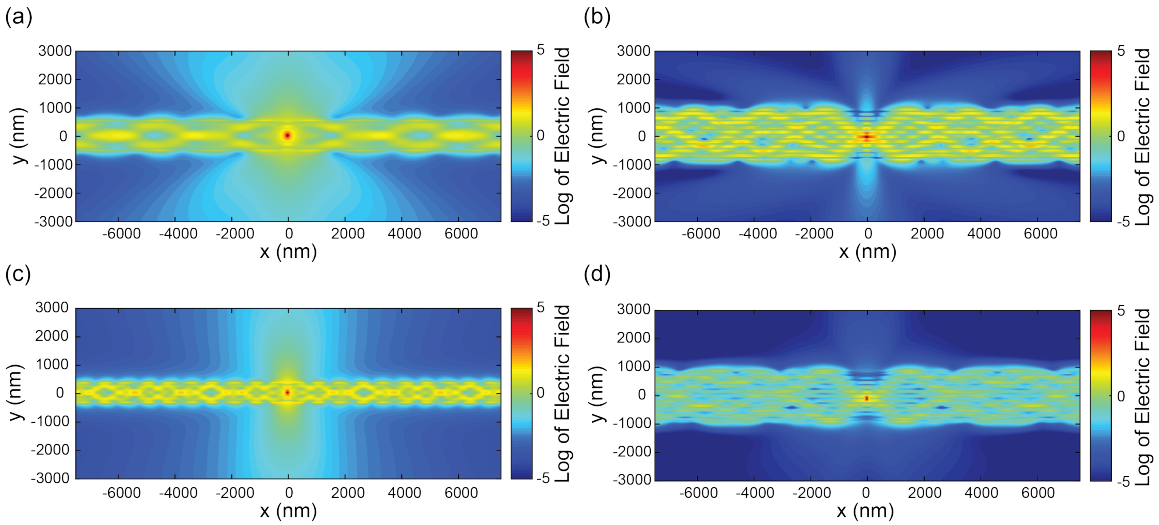

Figure 6.4: Log of electric field intensity for a luminophore embedded in the center of a standard polymer layer (a), a polymer layer within a photonic LSC (b), a standard titania layer (c), and a titania layer within a photonic LSC (d).

layer.

The increase in light guiding by the photonic structure when compared to the standard LSC is due to the highly directional emission from the emitters within the photonic structure. The log of the emitted electric field intensity for a dipole placed in the middle of the structure and with a wavelength that corresponds to the minimum escape cone losses is shown in Figure 6.4. In the case of the standard LSC, (Figure 6.4 (a) and (c)), we see an electric field distribution that matches with the emission of an unpolarized dipole within a medium. A fraction of the emitted light escapes the top or bottom of the concentrator, but a large fraction of the light is trapped by total internal reflection. Figure 6.4 (c) has a larger fraction of the emitted light trapped within the LSC compared to the polymer concentrator in Figure 6.4 due to the higher refractive index. This matches well with the difference in escape cone losses predicted for each of the standard concentrators.

The photonic LSCs show highly direction emission within the structure showing similar behavior as was seen in [2]. In addition, the intensity of the emitted light on the outside of the photonic structure is significantly reduced for both photonic LSCs with luminophores

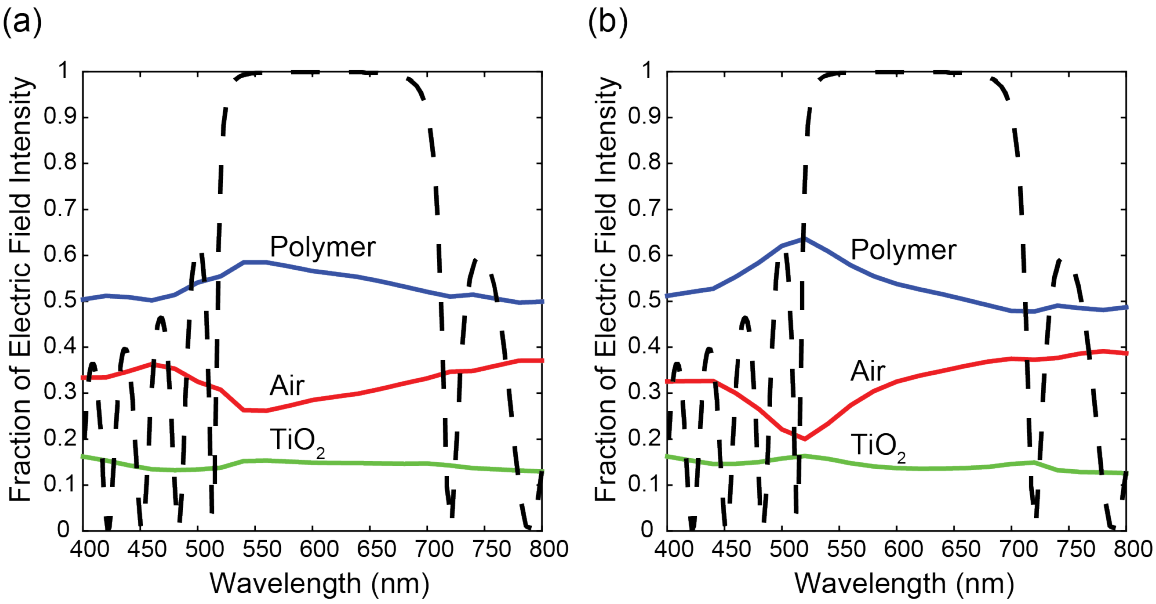

Figure 6.5: Predicted escape cone losses for a photonic LSC with luminophores embedded in the polymer (a) or titania (b) layer of the 1D Bragg stack.

embedded in the polymer and titania layers. However, it seems that the propagation of the emitted light within the LSC is different for the two different LSCs. For luminophores embedded in the polymer layer (Figure 6.4 (b) the greatest intensity of the electric field is in the polymer layer as it propagates through the LSC. However, for luminophores embedded in the titania layer (Figure 6.4 (c) the greatest intensity of the electric field is also in the polymer layer even though it is emitting from the titania layer.

To quantitatively characterize the electric field intensity of the emitted light in the polymer, titania, and air I integrated the total electric field intensity over each region. The results of this integration are shown in Figure 6.5. As expected the fraction of electric field intensity in the air decreases to a minimum for both photonic LSCs at the minimum in escape cone losses. However, it also shows that approximately 55% of the guided light propagates through the polymer layer independent of whether the emitter was embedded in the polymer or titania layer of the photonic LSC.

6.4 Conclusions

In this chapter we present a new design for a photonic LSC based on the structure of a 1D Bragg stack. By embedding the luminophores in one set of layers within the stack we increase the optical density of the photonic LSC compared to other cavity based concentrators and still observe highly directional emission. This highly directional emission decreases the escape cone losses for the luminophores embedded in the polymer layer for wavelengths greater than 500 nm with a maximum decrease of 36%. However, when the luminophores are embedded in the titania layer the escape cone losses are only decreased over a narrow spectral width from 475 - 500 nm. In general, this narrow bandwidth is not wide enough to accommodate most luminophores that would be embedded in the LSC. However, it is possible that embedding luminophores into the titania layer could be used for luminophores with significant reabsorption losses, narrow emission bandwidths, and low quantum yields as the probability of reabsorption losses is significantly reduced for luminophores embedded in titania. The guided light in these two photonic LSCs appears to propagate through the polymer layers of the stack as 55% of the emitted electric field is found in the polymer layer for luminophores embedded in both the polymer and titania layer.

Chapter 7

Nanoscale QD Poly(cyclohexylethylene) composites

7.1 Introduction

Thin films of LSCs have promising applications in building integrated photovoltaics (BIPV) as a way to integrate solar harvesting into the facades of urban buildings [35]. With the careful choice of luminophore and polymer matrix these LSCs could provide a method to achieve a semi-transparent energy harvesting glazing that could be incorporated into both opaque and transparent building materials in order to produce a distributed power generation system [4, 13, 14, 17, 35, 134, 135]. This glazing could also be integrated into the existing window architecture as a glazing or panel within the inert gap of the outer panes. This would likely give the concentrator a long life time as well as resistance to weathering. Even in current building stock a thin film LSC coating could be useful as a retrofit to existing windows or other building materials to harvest energy without significantly altering the current architecture. In this chapter, I will discuss work that has been done to create nanoscale LSCs using CdSe/CdS core/shell quantum dots embedded in Poly(cyclohexylethylene).

For most cadmium based concentrators to date the quantum dots are embedded in Poly(lauryl methacrylate). A drawing of the PLMA structure is shown in Figure 7.1 (a).

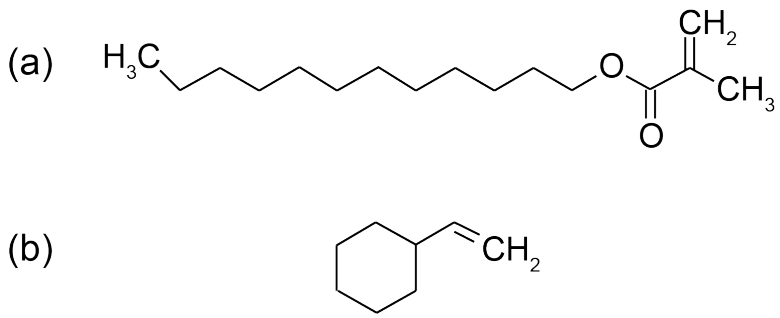

Figure 7.1: (a) Chemical structure of PLMA. (b) Chemical structure of PCHE.

High quality dispersions of CdSe/CdS quantum dots in the LMA monomer and nonpolar solvents are observed due to the interaction of the large carbon chain and the long chain ligands of the CdSe/CdS quantum dots. This has achieved high quality LSCs with a strong QY and little evidence of aggregation [57, 136–138]. While this polymer matrix produces high performing LSCs, PLMA is not often used as a polymer in industrial thin film applications because it has a glass transition temperature of -65 °C unless it is cross-linked. We have observed that films can be made from composites of CdSe/CdS and PLMA but they are not resistant to weathering affects and can be easily wiped off due to its glassy transition at room temperature.

Therefore, in this work we utilize poly(cyclohexylethylene) (PCHE) as the polymer matrix for the thin film composites. PCHE (Figure 7.1 (b)) is a derivative of the commodity polymer polystyrene where the benzene ring has been fully hydrogenated [139]. PCHE should be significantly more stable at room temperature as its glass transition temperature is 120 °C, which should reduce the damage that the LSC may experience as it heats up under operation as well as reduce the damage from weathering effects.

7.2 Methods

7.2.1 CdSe/CdS - PCHE Composite Fabrication

CdSe/CdS quantum dots were synthesized by Mayank Puri following the procedure detailed in Section 2.3.1. After synthesis the quantum dots were dried and dispersed in a known quantity of octane and a volume of this solution was added to pure octane such that the concentration of QDs in octane was 0.75 mg/mL, 2.5 mg/mL, or 30 mg/mL.

PCHE was synthesized by Colin Peterson and provided in a powdered form. An initial PCHE/octane solution was created at a concentration of 200 mg/mL and stirred for 2 hours in order to ensure full dissolution of the PCHE in the octane. Then the concentrated solution was run through an alumina plug to filter any polymer reaction byproducts or impurities. After filtration, a volume of the concentrated solution was added to the the QD/octane solution such that the PCHE was at a concentration of 60 mg/mL.

This final solution was then spun on 1 in x 1 in glass and silicon substrates using a Laurell WS-650Mz-23NPPB spin coater. The solution was deposited onto the substrate and then spun at 2000 RPM for 20 seconds with an acceleration of 500 RPM/s and then 500 RPM for 40 seconds with an acceleration of -500 RPM/s to complete the drying.

7.2.2 Variable Angle Spectroscopic Ellipsometry

The refractive index of the composite as well as the thickness was determined by spectroscopic ellipsometry using the Woolam Vase ellipsometer. Each of the films on the silicon substrate were measured spectrally from 350 nm to 1000 nm and with angles of incidence from 55° to 75° at three different location on the film. Then a Maxwell-Garnett effective medium approximation was used to determine the refractive index using the refractive index of a pure PCHE film and the refractive index of the CdSe/CdS quantum dots extracted

from absorption measurements. The Maxwell-Garnett EMA model is shown in the equation below.

$$\epsilon_{eff} = \epsilon_m \frac{2\delta_i (\epsilon_i - \epsilon_m) + \epsilon_i + 2\epsilon_m}{2\epsilon_m + \epsilon_i - \delta_i (\epsilon_i - \epsilon_m)}$$

Where ϵ_{eff} is the permittivity of the composite, ϵ_i is the permittivity of the quantum dots, ϵ_m is the permittivity of PCHE, and δ_i is the volume fraction of the quantum dots in the matrix.

7.2.3 Reflection and Transmission Measurements

Transmission and total reflection measurements were taken with a Cary 7000 UVvis spectrometer. Transmission was measured at $180°$. Diffuse transmission and total transmission were measured by measuring the incident light (T_1), the light transmitted by the sample (T_2), the light scattered by the instrument (T_3), and the light scattered by the sample and the instrument (T_4). Then the total transmission and diffuse transmission were calculated with the following equations:

$$T_t = \frac{T_2}{T_1}$$

$$T_d = T_4 - T_3 \left(\frac{T_2}{T_1}\right)$$

Total reflection was measured by mounting the sample, tilted at $3° \; 10'$ to the reflection port of an integrating sphere within the diffuse reflectance accessory for the Cary 7000. Diffuse reflectance was measured by mounting the sample at normal incidence to the reflection port of the integrating sphere. In this way specular reflection was calculated as the subtraction of total and diffuse reflectance.

7.2.4 Spatially-Resolved Measurements of Steady-State and Time-Resolved Photoluminescence

Spatially-resolved measurements of steady-state and time-resolved photoluminescence were measured by placing the glass samples on a nanopositioning stage and exciting with a 405 nm laser light source. Using Labview the sample was translated 100 μm in each lateral direction in steps of 5 μm and the emitted light was characterized with an Isoplane spectrometer and PIXIS CCD for steady-state photoluminescence characterization or a single photon avalanche diode and a time correlated single photon counting system for time-resolved photoluminescence characterization. The raw data was analyzed in MATLAB to extract important characteristics such as photoluminescence wavelength and radiative lifetime.

7.3 Results and Discussion

Characterization of the refractive index as well as the transmission and reflection of the thin film QD/PCHE composites are shown in Figure 7.2. At a loading fraction of 0.75 mg/mL there is no discernible change in the refractive index from the measured refractive index of a reference PCHE film. However, as the concentration is increased up to 30 mg/mL we observe a modification of the refractive index to show more characteristics of the QDs and less of the bare PCHE film. The increase in refractive index at higher loading fractions also increases the refractive index greater than the refractive index of the glass substrate (n = 1.52), which will alter the optical transport in the thin film LSC. The change in optical transport when the film has a refractive index less than or greater than the refractive index of the glass substrate will be discussed in more detail below.

This increase in volume fraction and refractive index of the composite has significant affects on the transmission and reflection properties of the composites. As the concentra-

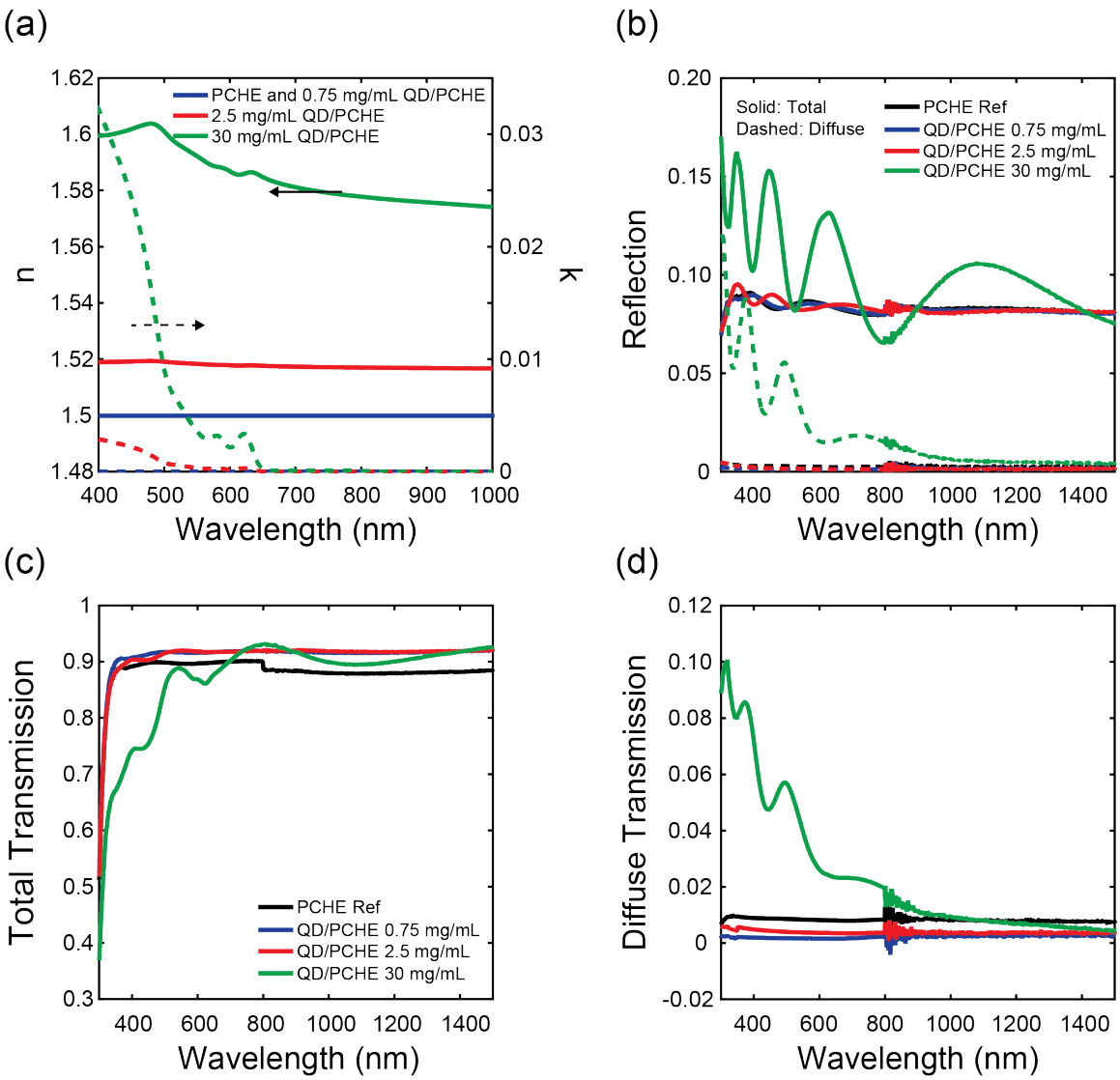

Figure 7.2: Real (solid) and imaginary (dashed) components of the refractive index (a), reflection (b), and transmission (c) and (d) measurements for QD/PCHE composites at a loading fraction of 0.75 (blue), 2.5 (red), and 30 (green) mg/mL.

tion of the QDs increases within the PCHE composite we observe the oscillation of the reflection and transmission spectra due to thin film interference effects. Along with this at large loading fractions we observe an increase in the diffuse transmission of the composite. The forward scattered light is likely due to an increase in scattering due to the large volume fraction of QDs in the composite, which for 30 mg/mL is 10.5% by volume.

The concentration of the QDs within the PCHE composite will also have an impact

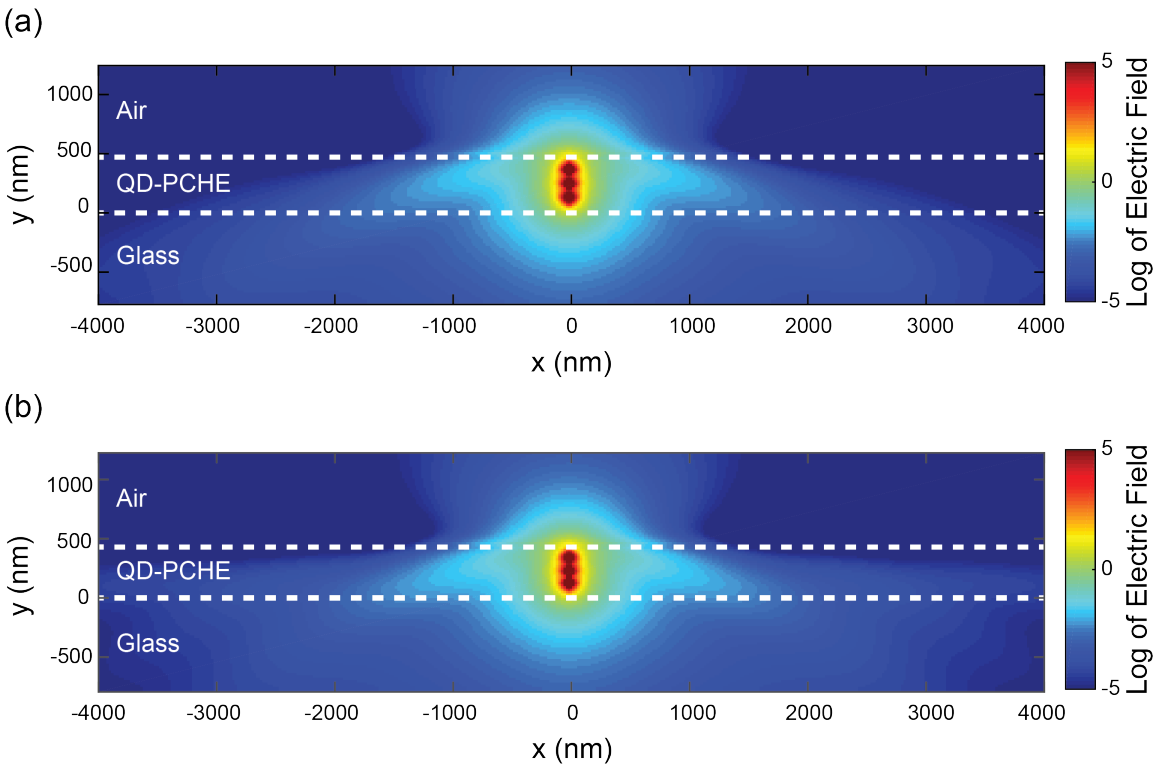

Figure 7.3: Electric field intensity distribution showing the propagation of emitted light from a QD-PCHE composite loaded at 2.5 mg/mL (a) and 30 mg/mL (b).

on the optical transport of the LSCs. Figure 7.3 shows the average electric field intensity distribution for the PCHE composites loaded at 2.5 mg/mL (a) and 30 mg/mL (b). The electric field intensity distribution is made up of the average electric field intensity of 3 unpolarized dipoles emitting at 630 nm and spaced evenly throughout the thickness of the composite. When the refractive index of the composite is less than the refractive index of the glass substrate (Figure 7.3 (a)) the electric field propagates freely into the glass substrate. However, when the refractive index of the composite is greater than the refractive index of the glass substrate (Figure 7.3 (b)) a portion of the emitted light is trapped within the thin film. The emitted light that propagates through the thin film will have a long path length through a highly concentrated composite, which could make it susceptible to reabsorption losses. It is likely that there is an optimum loading fraction that balances the increase in absorption of incident sunlight with the increase in reabsorption losses.

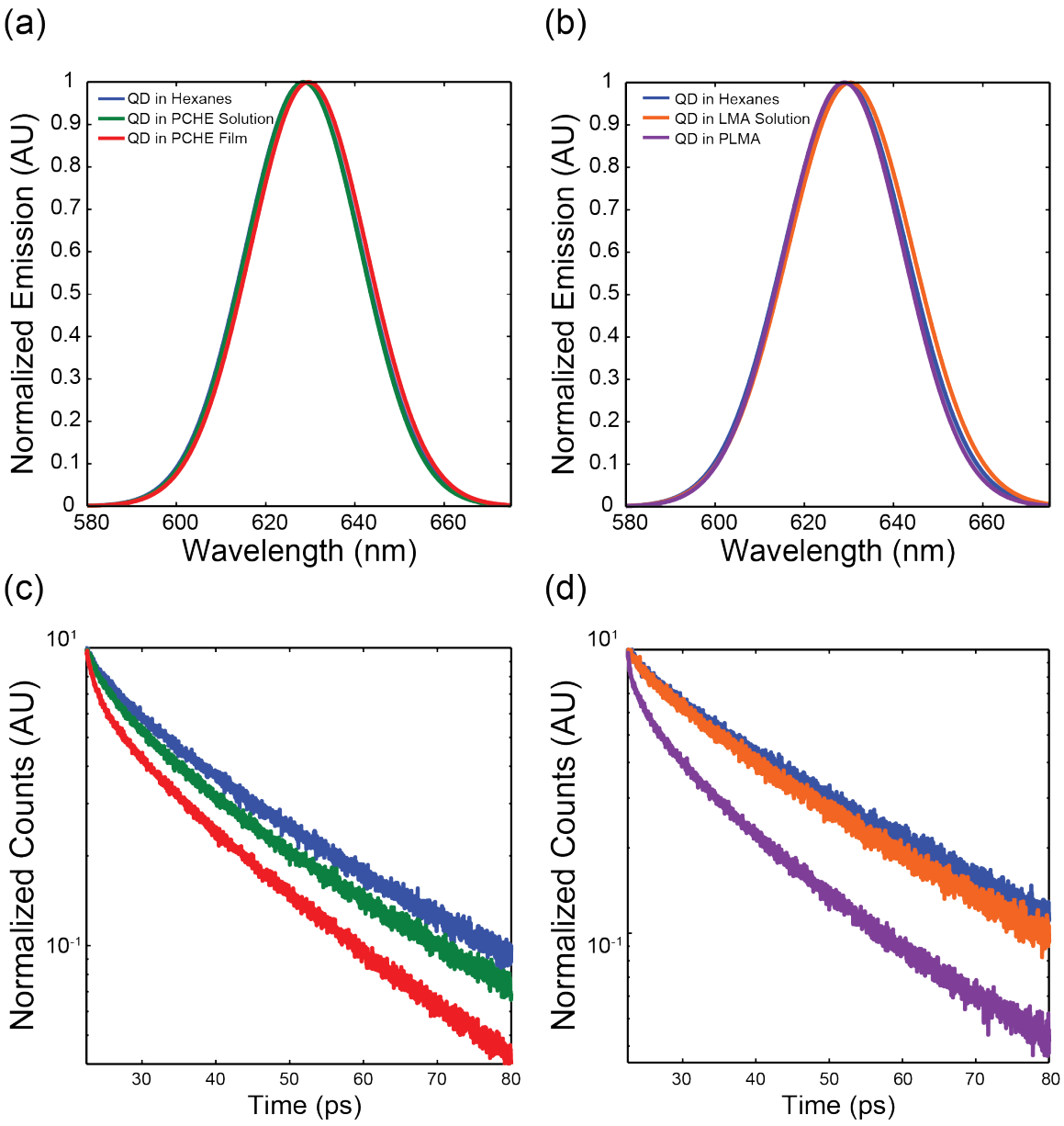

Figure 7.4: Steady-state (a),(b) and time-resolved photoluminescence (c),(d) for QD/PCHE thin films (a),(c) and QD/PLMA bulk composites (b),(d).

Figure 7.4 shows a comparison between the steady-state and time-resolved photoluminescence properties of CdSe/CdS core/shell QDs embedded in a PCHE thin film or a bulk PLMA composite. In both the PCHE and PLMA composites there is little change in the photoluminescence wavelength of the QDs as it goes from the synthesized QDs in hexanes, to the respective polymer precursor solution, and then finally the solid state.

The time-resolved photoluminescence figures (Figure 7.4 (c) and (d)) show some difference between the PCHE and PLMA composites. To quantitatively compare the radiative lifetimes for each experiment the time-resolved photoluminescence data is fit to a stretched exponential function.

$$f(t) = e^{-\left(\frac{t}{\tau}\right)^{\beta}}$$

Where τ is the radiative lifetime and β is stretching exponent that describes how well the decay matches a single exponential decay.

It appears that the lifetime of the QD/PCHE precursor solution shows a small decrease in the lifetime as compared to the as-produced QDs in Hexanes from 18.2 ns to 14.7 ns with a change in beta from 0.77 to 0.72. This drop is not as large as when incorporated into the LMA solution where the lifetime changes from 22.6 to 20.0 ns and the beta changes from 0.81 to 0.82. This is likely due to impurities on the produced PCHE that may interact with the QY of the CdSe/CdS QDs. Further filtration steps may help to reduce this effect. Even though there is a small drop in solution it appears that both the PCHE and PLMA composites show approximately the same drop in lifetime from the solution to solid state to 12.4 and 11.7 ns with a beta of 0.71 and 0.71 respectively. This has also been observed in other polymer systems [135] with CdSe/CdS core/shell QDs. In total we observe that the QDs do not red-shift significantly in the the PCHE composite and produce a composite with a similar radiative lifetime as a composite with PLMA.

To further explore the optical homogeneity of the QD/PCHE composites spatially-resolved measurements of steady-state and time-resolved photoluminescence measurements were performed on the glass samples and each loading fraction. These results are summarized in Figure 7.5. The photoluminescence wavelength data shows as slight redshift in photoluminescence as a function of concentration. In addition to a slight red-shift, the radiative lifetime also decreases as a function of loading fraction within the LSC from 12 ns

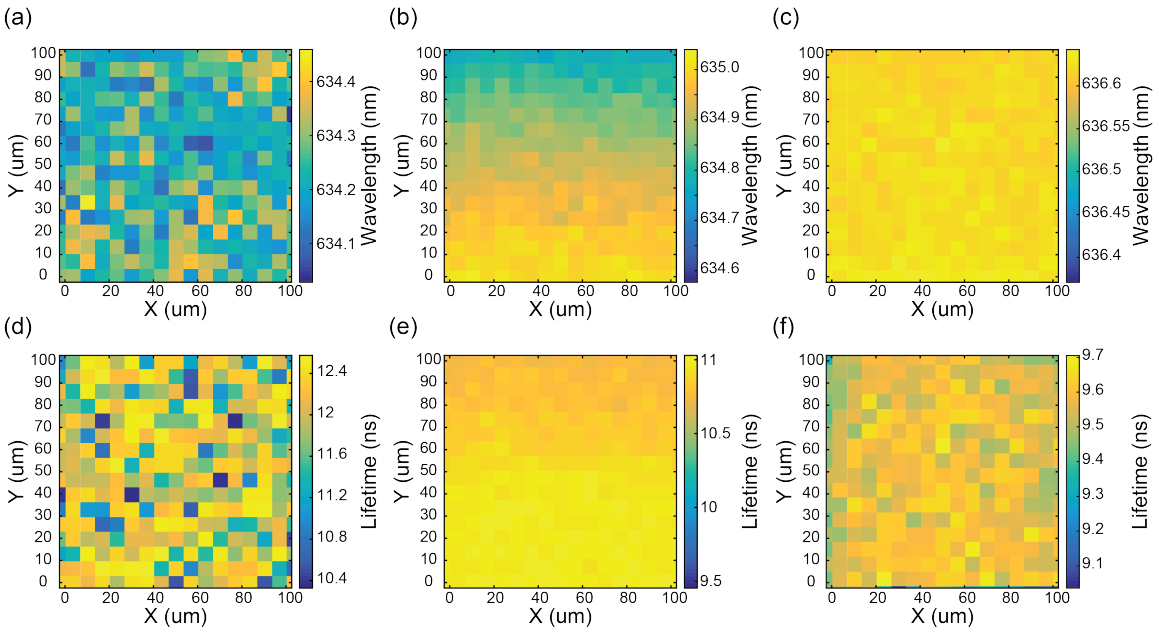

Figure 7.5: Photoluminescence wavelength (a), (b), and (c) and radiative lifetime (d), (e), (f) data for QD/PCHE thin films with a loading fraction of 0.75 (a) and (d), 2.5 (b) and (e), and 30 (c) and (f) mg/mL.

to 9.5 ns at the largest loading fraction. A possible mechanism for this is the increased rate of radiative and non-radiative energy transfer from one quantum dot to another may occur as the QDs are brought closer together. This would likely reduce the QY of the composite overall.

7.4 Conclusions

In this chapter I have demonstrated work done to fabricate CdSe/CdS core/shell QDs embedded in PCHE a commodity polymer that could be advantages for BIPV installations. The QDs disperse well in the PCHE film as evidenced by steady-state and time-resolved photoluminescence measurements and they emit with similar optical properties as QD/-PLMA composites that are often found in literature. As the loading fraction of the QDs in the PCHE increases the refractive index of the composite takes on more of the characteristic of the QD material as opposed to the PCHE. In addition, some non-ideal reflection and

transmission properties are observed including diffuse scattering near the UV wavelengths. However, this diffuse scattering should not significantly affect the visible transmittance of the coating, but further study will be needed to determine the affect on LSC light guiding properties. Finally, the increase in loading fraction also increases the refractive index of the composite. When the refractive index of the composite is greater than the refractive index of the substrate a portion of the emitted light becomes trapped within the thin film becoming more susceptible to reabsorption losses. Further study is needed to determine the optimum loading fraction that optimizes incident light absorption and increased reabsorption.

Chapter 8

Silicon Quantum Dot-Poly(methyl methacrylate) Nanocomposites with Reduced Light Scattering for Luminescent Solar Concentrators

8.1 Introduction

In Chapters 4, 5, and 7 the optical transport of LSCs were studied using CdSe/CdS core/shell quantum dots. However, for commercial applications CdSe/CdS is not an attractive luminophore due to its carcinogenic properties and relatively low abundance [140]. Si QDs, as introduced in Section 2.3.2, are an attractive luminophore replacement for semi-transparent, large-area LSCs due to their indirect, near-infrared emission [35, 91], low toxicity [92, 93], and widespread elemental abundance [14]. However, since Si QDs have only recently been proposed for use in LSCs, little work has been completed to incorporate them into polymer matrices. Ideally, methods should be developed to incorporate Si QDs in a wide library of polymers while maintaining their high PLQY and suppressing particle agglomeration that leads to scattering losses [141]. As we demonstrate in this Chapter, scattering losses can significantly affect the performance of large-area Si QD LSCs. We expect that all nanocrystal based composites will suffer from light scattering losses depending on the loading fraction of the luminophore. Therefore, while we focus on modeling and

characterizing the scatter behavior of Si LSCs, we expect the techniques and models used in the Chapter to be relevant to other nanocrystal composites.

Limited reports indicate that Si QDs can withstand bulk polymerization in polymers including poly(methyl methacrylate) (PMMA) [142, 143], poly(dimethylsiloxane) [144], thiolene polymers [145], silicone elastomers [146], and polystyrene [147], as well as in silica aerogels [148]. However, only one report provides significant evidence for low scattering cross sections in bulk polymerized Si QD/polymer composites, wherein Si QDs were incorporated within flexible slabs of poly(lauryl methacrylate) crosslinked with ethylene glycol dimethacrylate [14]. In terms of building-integrated LSC applications, however, PMMA and polycarbonate have been noted as desirable host polymers due to their favorable mechanical properties and relatively low parasitic absorption [49, 50]. Herein, we focus on incorporating Si QDs into PMMA, a commodity thermoplastic with high clarity and light transmittance coupled with good strength, stability, and scratch resistance [149]. PMMA is popular for optical and structural applications alike and is less expensive than polycarbonate, making it an interesting polymer for Si QD encasement.

In this study, we prepare and examine the optical properties of Si QD/PMMA composite slabs. We determine the effect of Si QD concentration on light scattering properties by examining loading fractions ranging from 0.06 to 0.50 wt %. Using a variety of spectroscopic techniques, we also examine the effects of two different Si QD surface ligands on the transmission and light scattering properties of these composites. The studied ligands include a long alkane (1-dodecene) and an ester-functionalized alkane (methyl 10-undecenoate), which has not previously been studied within the PMMA system. We find that the more polar surface moieties enable a single-particle dispersion of Si QDs in methyl methacrylate, or MMA, which translates to reduced light scattering by Si QDs in PMMA. Attenuation measurements demonstrate the impact scattering has on the waveguide losses of the composite slabs. These low scattering ester-capped Si QD/PMMA composites hold promise

for realizing efficient, nontoxic, and large-area LSCs.

8.2 Results and Discussion

8.2.1 Scattering in Si QD LSCs

To illustrate the importance of decreasing scattering losses in Si QD-based LSC devices, we employed a ray-tracing Monte Carlo model as described in Chapter 3 to predict concentration factors under different scenarios. The concentration factor is an LSC figure of merit that depends on device geometry and light concentration performance. It is defined as the geometric gain of the device (collection face area/concentration edge area) multiplied by the fraction of incident light that is successfully concentrated to the collection edge. In Figure 8.1, we show some concentration factor predictions, comparing results from 50% (a) or 100% (b) PLQY Si QDs with varying scattering probabilities. In all cases, the LSCs are modeled to be 3 mm thick as this is the approximate thickness of common window glass. The 50% PLQY model represents the currently achievable case based on quantum yield measurements from our fabricated Si QD/PMMA composite slabs. The incoming sunlight is modeled as normally incident for these results, which provides the lower limit for the concentration factor since the addition of diffuse sunlight increases the concentration factor at relevant concentrator tilts.

The predicted concentration factor may also be weighted for realistic operating conditions. In Figure 8.2 we show the predicted concentration factor for LSCs tilted at 0° (horizontal), 45° (latitude), and 90° (vertical window) in Minneapolis, MN (45° N geographic latitude) as well as the predicted concentration factor for a LSC with only normally incident sunlight. The direct normal irradiance (DNI) and diffuse horizontal irradiance (DHI) for Minneapolis, MN are taken from Typical Meteorological Year data sets in the National Solar Radiation Data Base and converted into incident solar energy per year and square meter as a function of angle [150]. The total expected energy per year is shown in

the legend of Figure 8.2 for each operating condition. With the expected angular distribution of incident sunlight, the average concentration factor is predicted for each operating condition by weighting the Monte Carlo results by the incident angular distribution.

An isotropic scattering probability is included in the model and described in terms of a characteristic scattering length. This is defined as the distance light travels such that the fraction of incident light scattered is $\frac{1}{e}$, where the probability of light scattering follows the equation

$$P_s = e^{\frac{-l}{l_s}}$$

where P_s is the probability of scattering, l is the distance traveled in meters, and l_s is the scattering length in meters.

Figure 8.1 (a) and (b) show the predicted concentration factors for LSCs with a 3 mm thickness, a loading fraction of 0.1 wt %, different lateral sizes, and different scattering lengths. Scattering can originate from various sources, including individual nanocrystals, aggregates, and inhomogeneities within the polymer [51, 52]. In some cases, scattering can be beneficial as either sunlight or luminescent light can be scattered directly into the solar cell. However, this tends to only be useful for small concentrators. As the lateral size increases, the effect of scattering becomes detrimental since it disrupts the propagation of luminescent light toward the edge and increases escape cone losses. In general, for large Si QD LSCs, significant concentration factor gains can be achieved by increasing the scattering length/LSC size ratio from 0.01 to 1. Some further improvement in the concentration factor is observed for ratios of up to ~ 100 for LSCs with side lengths greater than ~ 30 cm. In the case of perfectly dispersed ~ 3 nm diameter Si QDs at a loading of 0.10 wt % we can analytically calculate the expected scattering length. This is calculated using a quasi-static approximation where the size of the particle is much smaller than the wavelength of incident light [151]:

$$C_{sca} = \frac{k^4}{6\pi}|\alpha|^2$$

where C is the cross section, k is the incident wave vector, and α is the polarizability, which is equal to:

$$\alpha = \frac{4\pi r^3 (\epsilon - \epsilon_m)}{\epsilon + 2\epsilon_m}$$

In the above equation r is the radius of the particle, ϵ is the permittivity of the particle, and ϵ_m is the permittivity of the surrounding medium. Using the scattering cross section we can calculate the scattering length of the LSC as a function of wavelength using the assumption that the scattering length (l) is the distance traveled such that $\frac{1}{e}$ of the incident light is scattered. Therefore,

$$1 = C_{sca} N l$$

where N is the number concentration of Si nanocrystals in the PMMA matrix, which is calculated as:

$$N = \frac{V_F}{\frac{4}{3}\pi r^3}$$

In the above equation V_F is the volume fraction of Si, which is estimated to be 0.0005 for Si loaded at 0.1 wt %. The calculated scattering length as a function of nanoparticle radius is shown in Figure 8.3 at a wavelength of 845 nm, which is the peak of the luminescence spectra of the Si QDs. For our $\sim$ 3 nm diameter Si QDs at a loading of 0.10 wt % a scattering length of 51 m is expected, which far exceeds the length scale required for window applications.

Figure 8.1 (c) and (d) compare the fraction of absorbed photons that are either collected at the edge (optical efficiency, also called optical quantum efficiency) or lost via various

mechanisms for a $1m^2$ concentrator. The figures present the outcome only for photons that are absorbed at least once in the LSC; sunlight that passes through the concentrator and is neither absorbed nor collected is taken out of this calculation in order to show the loss pathways clearly. The category absorbed loss represents light that is lost nonradiatively after an absorption event. Reabsorption loss, in contrast, corresponds to light that experiences at least two absorption events before also being lost nonradiatively. Scattered loss includes emitted photons that exit out of the top or bottom face of the concentrator after one or more scattering events, while escape cone loss includes photons exiting the same way without any scattering event, but possibly after a reabsorption and reemission event. While reabsorption is expected to be small in these concentrators, the large path lengths of these 1 m x 1 m concentrators can lead to a significant amount of reabsorption. This leads to increased reabsorption and escape cone losses for 50% PLQY Si QDs (Figure 8.1 (c)), as well as increased escape cone losses for 100% PLQY Si QDs (Figure 8.1 (d)). If no reabsorption was assumed, then the predicted escape cone losses would approach 25% for large scattering lengths as expected for a single photoluminescence event (Figure 8.4).

These figures show that scattering is one of the most significant loss mechanisms that limits the performance of these LSCs. In the case of 50% PLQY Si QDs, the largest loss mechanism is absorbed loss deriving from the nonunity quantum yield. For scattering lengths less than 0.1 m, light scattering is the second most dominant loss mechanism. This loss does not become negligible until the scattering length exceeds 1 m, which is the side length of the modeled LSC. Similar trends are exhibited in the 100% PLQY case, wherein scattering is the primary loss mechanism for scattering lengths below approximately 0.1 m for 1 m^2 LSCs. These results indicate that long scattering lengths are required for efficient, large-area LSCs. Strategies that reduce scattering losses may be more important than either reducing reabsorption through luminophore design or reducing coupling of luminescent light to the escape cone.

8.2.2 Nanocomposite Fabrication

Si QD/PMMMA nanocomposites were fabricated by Samantha Hill and Uwe Kortshagen in the Mechanical Engineering Department at the University of Minnesota. The silicon QDs were produced in a nonthermal plasma according to previously published methods [90] and were functionalized with one of two different ligands: methyl 10-undecenoate (referred to as ester-Si QDs) or 1-dodecene (referred to as alkane-Si QDs). Methyl 10-undecenoate is not a commonly reported ligand for Si QDs, but enables good suspensions in polar solvents [152]. In contrast, 1-dodecene is frequently reported in the literature to enable single-dot dispersions of Si QDs in nonpolar solvents [153]. These functionalized Si nanoparticles were turned into composites at a variety of loading fractions and I characterized the composites. The remainder of this chapter will focus on my characterization and modeling.

8.2.3 Nanocomposite Scattering Properties

To quantitatively characterize the light scattering of these slabs, transmission and total reflection spectra were measured from 400 to 1600 nm, as shown in Figure 8.5. Transmission and total reflection measurements were taken with a Cary 7000 UV-vis spectrometer. Transmission was measured at 180°, and the spectra were corrected for the transmission of an undoped PMMA slab of the same thickness by using it as the 100% transmission reference. Compared to the PMMA reference slab, transmission decreases either because of Si QD absorption, which occurs for wavelengths less than 800 nm, or scattering, which can occur over the entire wavelength range.

Since Si QD absorption is expected to be nearly zero above 800 nm, we focus initially on the transmission of the near-infrared (NIR) light to discuss the scattering properties of the Si QD/PMMA slabs. For every Si QD/PMMA slab we fabricated, light transmission in the NIR region of the spectrum for the alkane-Si QD sample is significantly lower than

the corresponding ester-Si QD sample. We expect that this is due to Si QD agglomeration facilitated by the chosen surface species. Agglomeration leads to an increased number of strong scattering centers based on the volume dependence of scattering. Such scattering sites can both forward and backward scatter the incident light within the concentrator, which will decrease the transmittance measured by the detector positioned 180° from the incident light beam.

The ester-Si QDs also retain high optical transmission in the PMMA matrix for much higher loading fractions than the alkane-Si QDs. The ester-Si QDs retain high transmission, near 100% for loading fractions up to 0.15 wt %. The alkane-Si QDs, in contrast, do not have complete transmission in the NIR for even the lowest loading fraction of 0.06 wt %. In addition, the ester-Si QDs with a loading fraction of 0.25 wt % still show a greater NIR transmission than the alkane-Si QDs with a loading fraction of 0.06 wt %. These are promising results for designs that require high absorptivity from the composite combined with minimal agglomeration of the Si nanoparticles.

The total reflection spectra in Figure 8.5 (b) are used to assess the extent of scattering at wavelengths shorter than 800 nm. Total reflection was measured by mounting the sample, tilted at $3^\circ 10'$, to the reflection port of an integrating sphere within the diffuse reflectance accessory for the Cary 7000. Scattering is important in this spectral range, as the Si QDs exhibit broad photoluminescence from 650 - 950 nm. Total reflection measurements detect contributions from specular reflection, diffuse reflection, and back scattering. The total reflection of our undoped PMMA slab is shown for reference in the solid black line in Figure 8.5 (b). For all of the nanocomposite samples, the total reflection spectra exhibit a common shape, featuring a maximum in the range of 580 - 700 nm, depending on the loading fraction. Because the loading fractions of Si QDs are low, the nanocomposite is expected to exhibit a refractive index and corresponding reflectivity following that of the PMMA reference. As a result, we conclude that the high reflection from the nanocomposites in the

visible region is due to backscattering from agglomerated Si QDs. At shorter wavelengths, the Si QD absorption starts to dominate over the scattering cross section, leading to the minimal reflection at 400 nm for all doped samples. The reflection minima present in all samples in the near-infrared correspond to absorption overtones from the polymer matrix (Figure 8.6).

For samples of the same loading fraction, the reflection data shows that ester-Si/PMMA slabs have reduced reflection relative to the alkane-Si/PMMA slabs. Since the slab surfaces exhibit similar specular reflection (Figure 8.7), we conclude that the large differences in reflection are driven by agglomeration-induced scattering. Additionally, for PMMA slabs with 0.06 and 0.10 wt % ester-Si QDs, no extra reflection was measured compared to the undoped PMMA reference. These results suggest that good dispersions of the ester-Si QDs in PMMA are achieved at loading fractions of 0.10 wt % or less. Some additional reflection is present for the 0.15 wt % ester-Si QD/PMMA sample, which was not obvious in the NIR transmission. The increased sensitivity of the total reflection measurement to scattering at shorter wavelengths demonstrates the complementary nature of these two data sets.

The percentage haze shown in Table 8.1 is used to determine the scattering of light over the visible spectrum, which is useful for future application as building integrated LSCs. The haze of the composites, which is the fraction of transmitted light that is forward scattered, was characterized using the ASTM D1003-13 standard [154]. Briefly, a Cary 7000 Universal Measurement Spectrophotometer with the diffuse reflectance accessory was used to measure the incident light, the total light transmitted by the specimen, the light scattered by the instrument, and the light scattered by the instrument and the specimen. These measurements were taken over the wavelength range from 380 nm to 780 nm and weighted by spectral power density of the CIE Standard Illuminate C. Then the percentage haze was calculated with the following equation

Sample	Haze (%)
PMMA Reference	7.7
Alkane-Si: 0.06 wt%	50.0
Alkane-Si: 0.10 wt%	82.7
Alkane-Si: 0.15 wt%	98.7
Alkane-Si: 0.25 wt%	99.6
Alkane-Si: 0.50 wt%	99.4
Ester-Si: 0.06 wt%	7.7
Ester-Si: 0.10 wt%	9.9
Ester-Si: 0.15 wt%	23.6
Ester-Si: 0.25 wt%	52.7
Ester-Si: 0.50 wt%	98.6

Table 8.1: Percentage haze measured for PMMA reference, Alkane-Si / PMMA composites, and Ester-Si / PMMA composites.

$$\text{haze} = \frac{T_4 - T_3\left(\frac{T_2}{T_2}\right)}{T_2} \times 100$$

where T_1 is the incident light, T_2 is the total light transmitted by the specimen, T_3 is the light scattered by the instrument, and T_4 is the light scattered by the instrument and the specimen. The Ester-Si / PMMA composites at 0.06 and 0.10 wt % loading fractions show comparable percentage haze to the PMMA reference value of 7.7% and significantly reduced haze compared to the Alkane-Si counterparts at the similar loading fractions.

Finally, we measured the attenuation of photoluminescence intensity as a function of excitation distance from the edge, with these results shown in Figure 8.11. Attenuation was measured using a 100 mW, 405 nm CW laser diode (Oxxius LBX-405-100-CIR-PP) as the excitation source. The composite sample was mounted with its large face perpendicular to the laser and its edge coupled to a 4 mm x 6 mm integrating sphere port. An OceanOptics Flame spectrometer was used to measure the output PL as the excitation light was moved in 0.5 mm increments away from the collection edge. The PL spectra were fit to a Gaussian distribution to identify the peak. The intensity value at the peak of photoluminescence was

corrected for the background measured in the range of 344 - 550 nm and then normalized to the initial value when the excitation was located at the collection edge. The photoluminescence spectrum was corrected for the background intensity measured in the range of 344 - 550 nm, and then fit to a Gaussian distribution to identify the peak of the spectrum. In order to produce the best fit, the data from 850 nm and longer in wavelength was removed, as the sensitivity of the detector degrades rapidly after this point. The extracted peak intensities were then averaged for data collected at the same position. This lead to an average of 10 points at each position from 0.5 mm - 19.5 mm away from the edge, and an average of 5 points per position at 0 mm and 20 mm away from the edge. The averaged raw photoluminescence spectra, an example fit, and the averaged fitted photoluminescence spectra are shown in Figures 8.8, 8.9, and 8.10 respectively.

These measurements probe the influence of light scattering on the trapped luminescent photons. In Figure 8.11, the intensity at the wavelength of the peak of the photoluminescence spectrum at each excitation distance was divided by the intensity of the peak of the photoluminescence spectrum at the point where the laser is incident closest to the integrating sphere. The overall shape of the attenuation of the photoluminescence as a function of excitation position derives from the reduction in the solid angle of the collection port as the excitation spot moves farther away, as well as waveguide losses such as reabsorption and/or scattering. We expect the minor reabsorption effects to be mostly unaffected by the choice of capping ligand, but to increase with increasing Si QD loading. We also expect to observe changes in the scattering based on the agglomeration state for the different Si QD surfaces and loading fractions.

The attenuation of photoluminescence due to the change is solid angle between the emission source and the detector was calculated numerically using the ray-tracing program Zemax. A 1.25 cm radius, 4.2 mm thick PMMA cylindrical disk was evaluated with a 4 mm by 6 mm rectangular detector placed 0.5 mm away from one edge of the disk. Then, a

Sample	Attenuation Length (mm)
Alkane-Si: 0.06 wt%	> 25
Alkane-Si: 0.10 wt%	17.9
Alkane-Si: 0.15 wt%	7.8
Alkane-Si: 0.25 wt%	5.4
Ester-Si: 0.06 wt%	> 25
Ester-Si: 0.10 wt%	> 25
Ester-Si: 0.15 wt%	> 25
Ester-Si: 0.25 wt%	> 25
Ester-Si: 0.50 wt%	16.3

Table 8.2: Extracted attenuation lengths for Alkane-Si / PMMA composites and Ester-Si / PMMA composites.

point source was scanned within the PMMA disk at the same locations of the attenuation experiment and the intensity of photoluminescence on the detector was calculated. This is shown in the black curve of Figure 8.11 (c). Good agreement of the distance dependent features of the disk is observed. However, small differences between the model and the experimentally measured data are to be expected. There is some uncertainty in the experimental excitation location, both laterally and along the thickness, as the laser spot has a finite width. Along with that the model uses a rectangular detector while the experimental measurement uses an integrating sphere with a similar size rectangular port.

Normalizing by the predicted attenuation due to the change in solid angle it is possible to observe the attenuation of the Si/PMMA composites due to reabsorption and scattering. This allows for an extraction of the attenuation length of emitted photons within the Si/PMMA composites if the attenuation length is less than 25 mm. If the attenuation length is greater than 25 mm then the photoluminescence does not decay enough to create an exponential decay fit with high quality. The extracted attenuation lengths for the composites are shown in Table 8.2.

Ester-Si QD/PMMA samples for loading fractions up to 0.10 wt % and alkane-Si QD/PMMA samples for loading fractions up to 0.06 wt % exhibit similar attenuation of the pho-

toluminescence as the excitation distance from the collection edge increases to 2 cm. The differences between the ligand treatments are more apparent at higher loading fractions, where the ester-Si/PMMA samples exhibit effective collection of photoluminescence from longer distances. The difference between the two sample sets increases with loading fraction until the highest concentration sample at 0.50 wt %. The quality of the fit in this case is reduced, however, since transmission through the slab is nearly zero after a distance of 4 mm. Because of this, we cannot characterize the attenuation effectively out to 20 mm and do not include the 0.50 wt % samples in this analysis. Based on these results, we conclude that ester-Si QDs result in longer photoluminescence propagation lengths and are more useful for light concentrating applications when using PMMA as the polymer matrix.

8.2.4 Outlook for LSCs

Using a combination of the same ray-tracing Monte Carlo models as discussed in Figure 8.1 and modifying a quality factor analysis found in reference [44] to account for solar cells on all sides and our experimental spectra, we make predictions about the limiting performance and sizes of these concentrators. Modifying the quality factor analysis gives:

$$C = \frac{b\left(1-R\right)\left(1-e^{-\alpha_1 d}\right)\eta_{PL}\eta_{trap}}{1+\beta\alpha_2 L\left(1-\eta_{PL}\eta trap\right)}\left(\frac{L}{4d}\right)$$

$$C_{sat} = \frac{b\left(1-R\right)\left(1-e^{-\alpha_1 d}\right)}{4\beta\left(\eta_{PL}^{-1}\eta_{trap}^{-1}-1\right)\alpha_2 d}$$

In the above equation C is the concentration factor, C_{sat} is the saturation concentration factor, b and β are factors from reference [44] that account for collection of reemitted light and an estimation factor of the waveguide efficiency respectively, and R is the reflection off of the top of the LSC. α_1 is the mean absorption coefficient weighted by the solar spectrum. α_2 is the mean attenuation coefficient over the photoluminescence region, which

is the summation of the overlap between the absorppion and photoluminescence spectra and the attenuation due to single particle scattering. L is the edge length of the concentrator and d is the thickness of the concentrator, which is 4 mm for these predictions. Finally, η_{PL} and η_{trap} are the photoluminescence quantum yield and trapping efficiency respectively.

Using these equations, we can predict the saturation concentration factor as a function of Si QD loading as well as the saturation length, which is found at the intersection of the predicted linear rise in concentration factor without attenuation and the saturation concentration. The results of these calculations are presented in Figure 8.12.

Assuming that the Si nanocrystals are perfectly dispersed so that the only scattering derives from the isolated nanocrystal scattering limit, we find that among the nanocrystal concentrations we experimentally studied, a loading fraction of 0.10 wt % leads to the highest concentration factor limits for both 50% and 100% quantum yield cases in 3 mm thick devices. The concentration factor limit is estimated to be 21x for an 11 m concentrator edge length with 50% PLQY, and 103x for a 26 m concentrator edge length with 100% PLQY (Figure 8.12). If we instead consider devices scaled for a residential window (3 mm thick slab, 1 m edge length), then the optimal loading for a nonscattering LSC is 0.06 wt % with a PLQY of 50% and 0.1 wt % for QDs for a PLQY of 100% (Figure 8.13). We also note that these 3 mm thick optimized devices have high visible light transmission, slightly exceeding our experimental, 4.4 mm thick slabs as shown in Figure 8.5. From these predictions, we expect that it is important to have a good dispersion of Si QDs in PMMA for loading fractions up to 0.1 wt % for large LSC applications. However, the difference in the quality of dispersions between ester-Si and alkane-Si composites is still useful at higher loading fractions as other composite applications may have different loading requirements due to different polymer thicknesses.

The characterization of these composites indicates that the ester-Si QD/PMMA composites are well-suited for LSC applications, whereas the alkane-Si/PMMA composites

are not. At a loading fraction of 0.10 wt %, the ester-Si QD/PMMA composites have transmission near 100% in the near infrared when adjusted for the extinction of a PMMA reference, have total reflection properties that mimic the blank PMMA reference, and exhibit improved photoluminescence propagation lengths when compared to the alkane-Si QD/PMMA composites. The alkane-Si QD/PMMA composites exhibit significant scattering that leads to increased diffuse reflection, incomplete transmission of unabsorbed light, and interrupted propagation of luminescent light toward the edge of the concentrator across the range of loading fractions that are appropriate for large-area LSCs.

8.3 Conclusions

In this chapter we show simulations that demonstrate that scattering losses can significantly reduce Si QD LSC performance. To reduce these losses we establish a strategy for improving the dispersion of the Si QDs in PMMA compared to previously published methods. We find that using a ligand with some structural similarity to the repeating polymer unit can facilitate the QD dispersion within the polymer matrix. In the Si QD / PMMA system, the ester group in methyl 10-undecenoate is more similar to MMA than an analogous unfunctionalized alkane. Correspondingly, ester-Si QDs exhibit improved dispersion relative to alkane-Si QDs. The fine dispersion of ester-Si QDs within the monomer translates into a bulk polymer composite with lower scattering losses even at higher loading fractions as compared to alkane-Si QD nanocomposites. The loading of Si QDs is not limitless, however, as increased scattering is observable for even the ester- Si QD / PMMA composites at and above 0.15 wt % Si. Based on concentration factor limit and Monte Carlo models, we predict that a loading fraction up to 0.1 wt % is necessary to achieve high concentration factors for window-scale concentrators made with 3 mm thick polymer sheets. Therefore, we conclude that ester-Si / PMMA composites show good promise for low-scattering window-scale LSCs, while alkane-Si / PMMA composites do not due to

significant scattering losses.

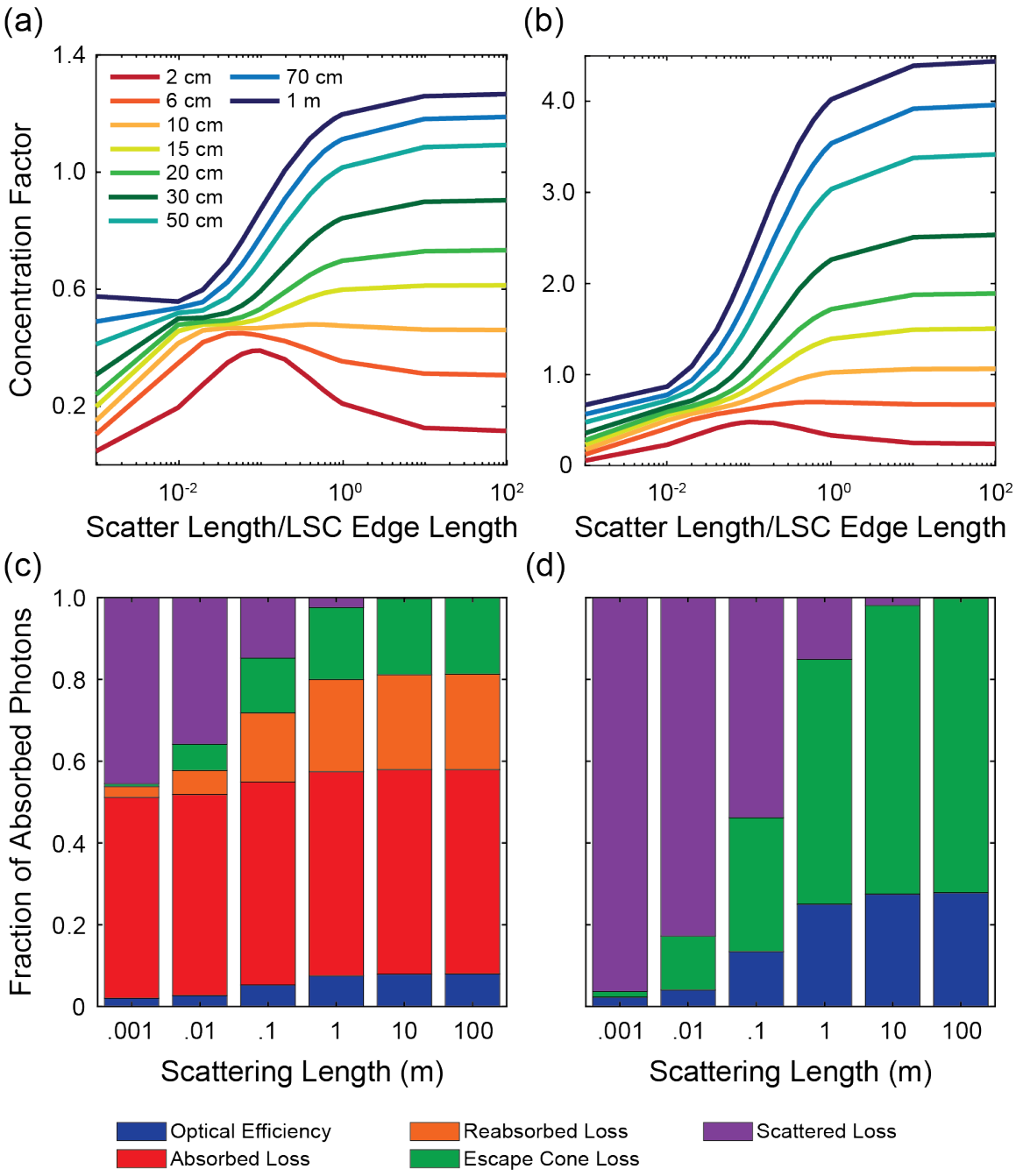

Figure 8.1: Simulated effect of scattering on Si QD LSC performance. The top row presents the concentration factor for square LSCs of side lengths ranging from 2 cm (red) to 1 m (purple) with a constant 3 mm thickness as a function of the scattering length to LSC side length ratio for a 0.1 wt % loading of Si QDs with (a) 50% or (b) 100% photoluminescence quantum yield. The bottom row shows the fraction of absorbed photons that are either collected by the solar cell at the edge of the concentrator or lost to various pathways for a 1 m2, 3 mm thick LSC with a 0.1 wt % Si QD loading and either (c) 50% or (d) 100% photoluminescence quantum yield. Photons that pass through the concentrator and are not absorbed are not shown here.

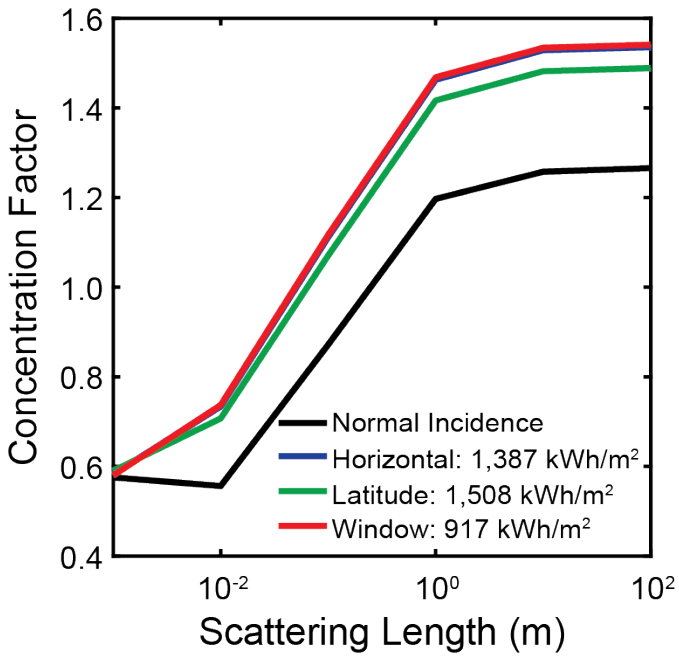

Figure 8.2: Predicted concentration factor as a function of scattering length for a 1 m x 1 m concentrator with a thickness of 3 mm, a loading fraction of 0.1 wt%, and photoluminescence QY 50%. Data is plotted for light at normal incidence (black) and at the expected angular profile when it is horizontal (blue), tilted at the latitude angle (green), and tilted vertically for a south facing window (red) in Minneapolis, Minnesota (45° N geographic latitude).

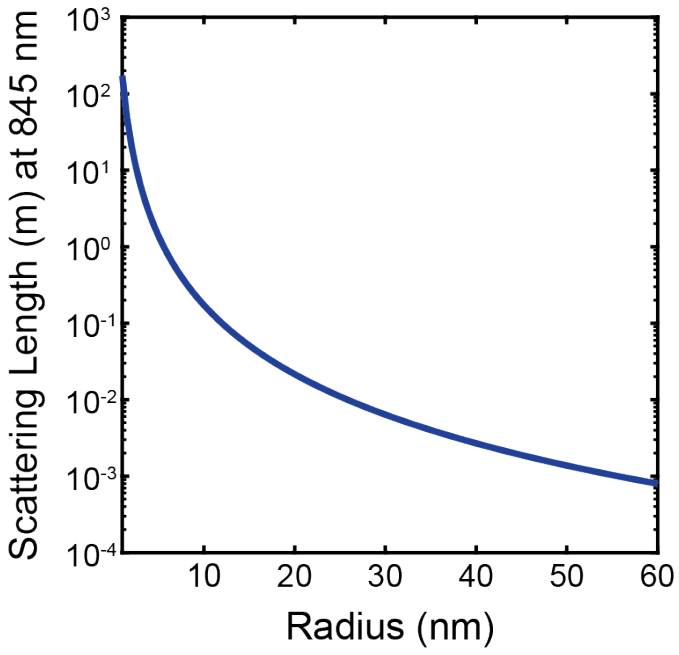

Figure 8.3: Calculated scattering length at 845 nm from Si spheres as a function of particle radius.

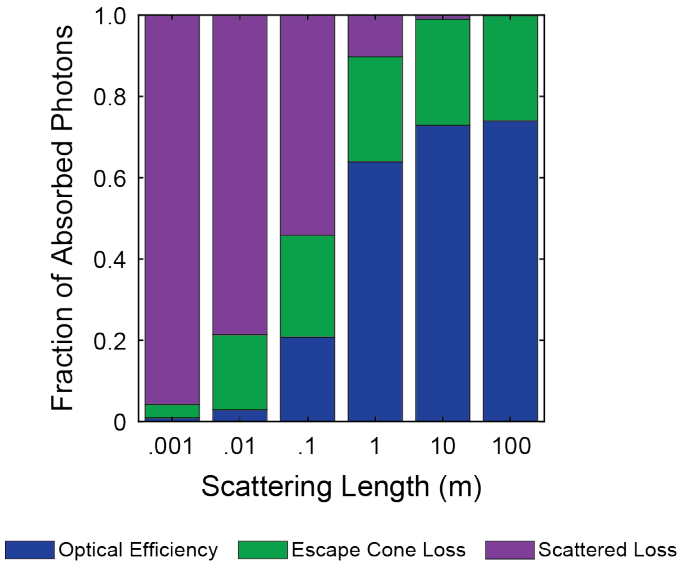

Figure 8.4: Fraction of absorbed photons that are either collected by the solar cell at the edge of the concentrator or lost to various path ways for a 1 m^2, 3 mm thick LSC with a 0.1 wt% Si QD loading, 100% photoluminescence quantum yield and no reabsorption of photoluminescent photons.

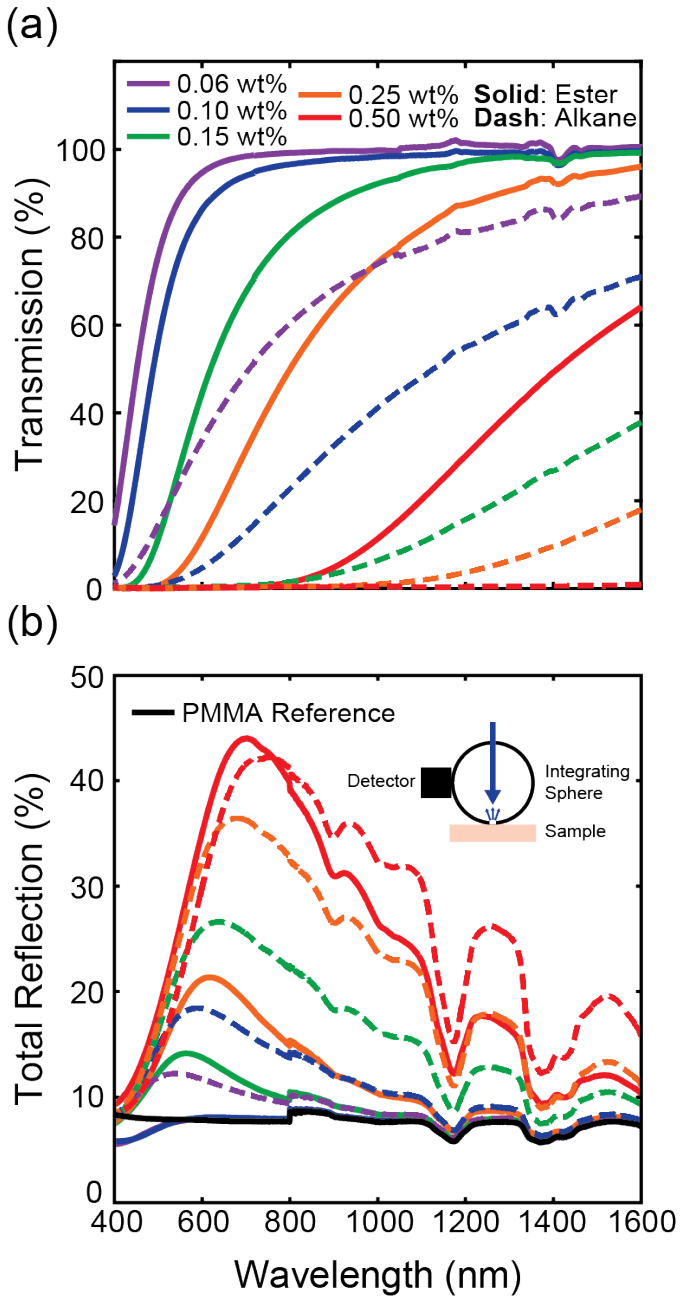

Figure 8.5: (a) Transmission at normal incidence and (b) total reflection of Si QD/PMMA composites using either alkane-Si QD (dashed line) or ester-Si QDs (solid line) at weight percentages ranging from 0.06 wt % (purple) to 0.50 wt % (red). Transmission is corrected by the PMMA reference while the total reflection is not, but includes the total reflection of the PMMA reference plotted in solid black line.

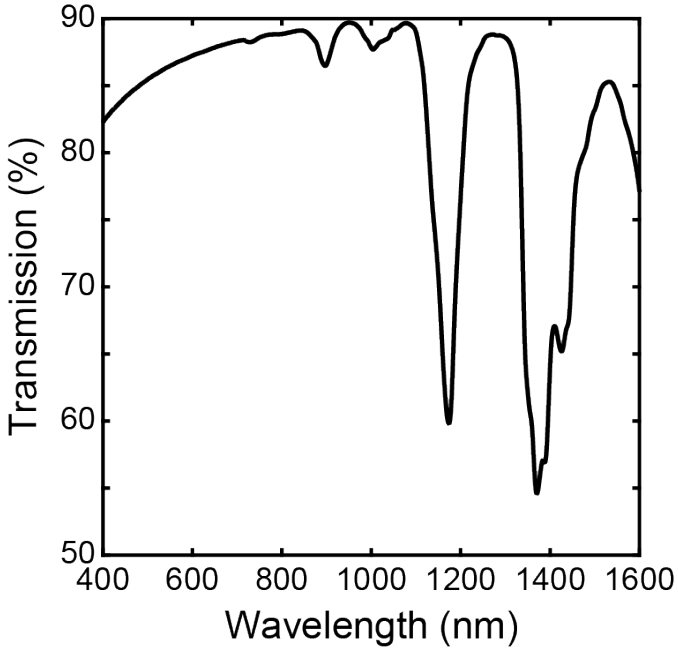

Figure 8.6: Transmission spectrum of PMMA reference.

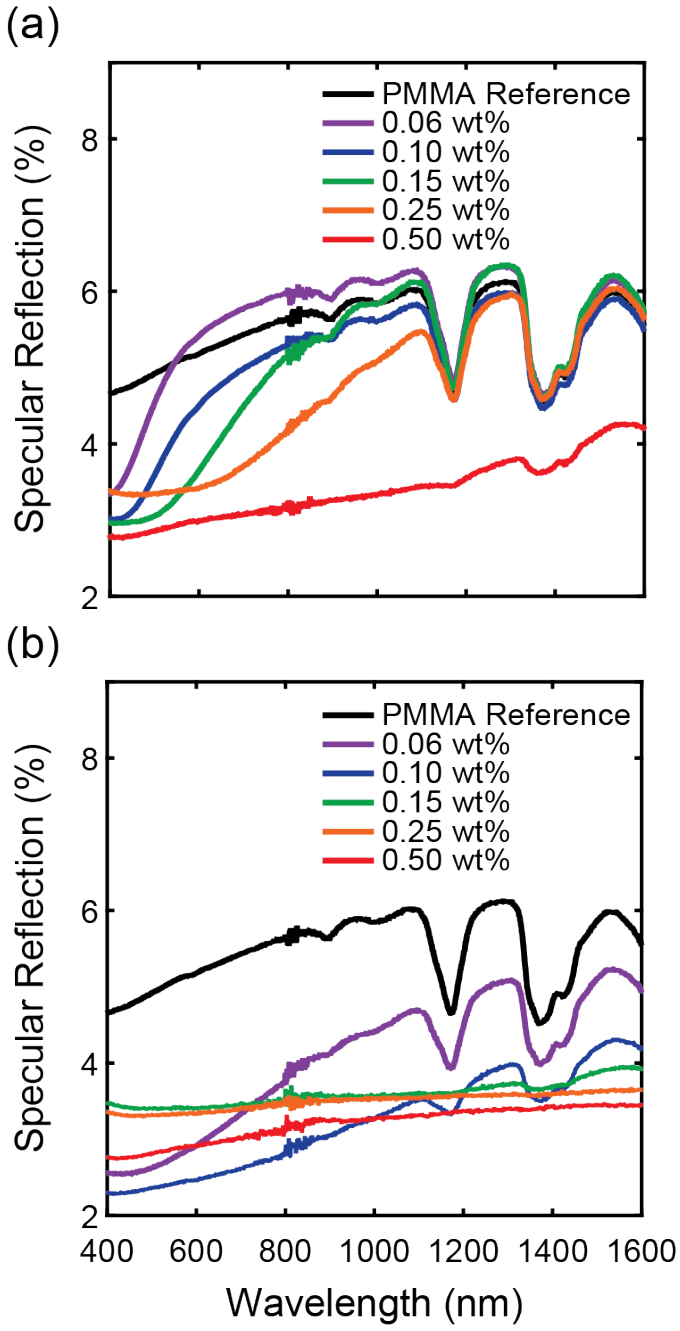

Figure 8.7: Specular reflection for (a) ester-Si QD or (b) alkane-Si QDs at loading fractions ranging from 0.06 wt % (purple) to 0.5 wt % (red). A PMMA reference is shown is black

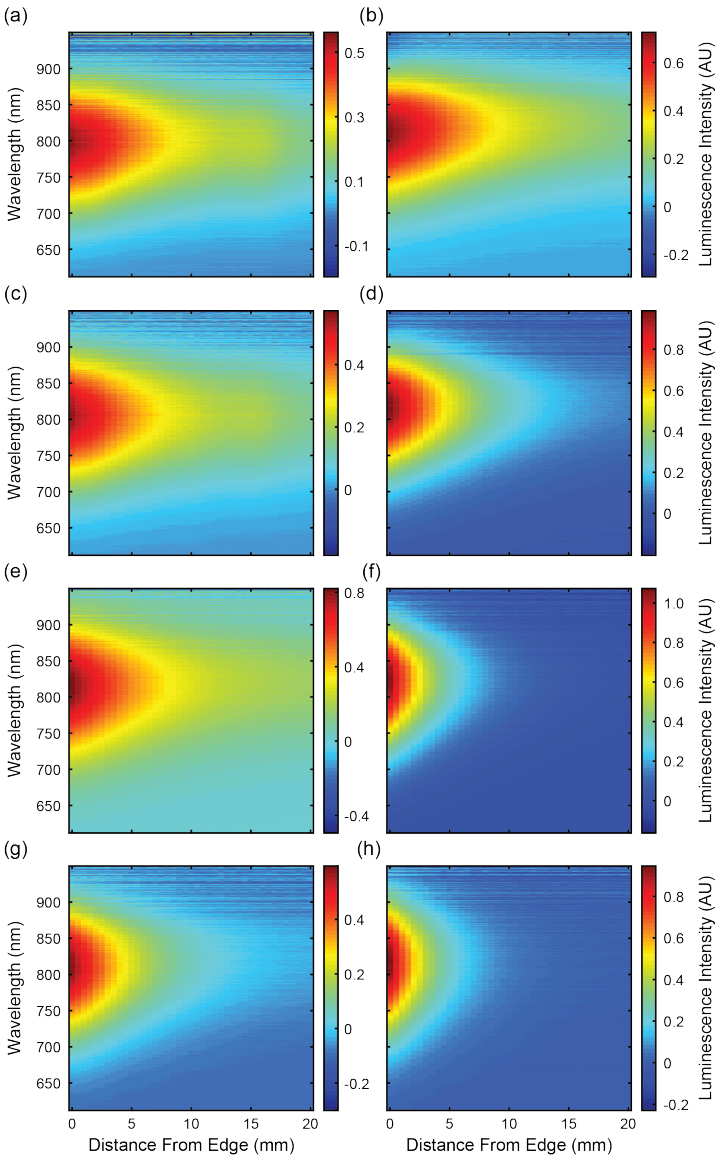

Figure 8.8: Luminescence intensity as a function of wavelength and distance from collection edge for (left) ester-Si and (right) alkane-Si at a loading fraction of (a,b) 0.06 wt %, (c,d) 0.10 wt %, (e,f) 0.15 wt %, (g,h) 0.25 wt %.

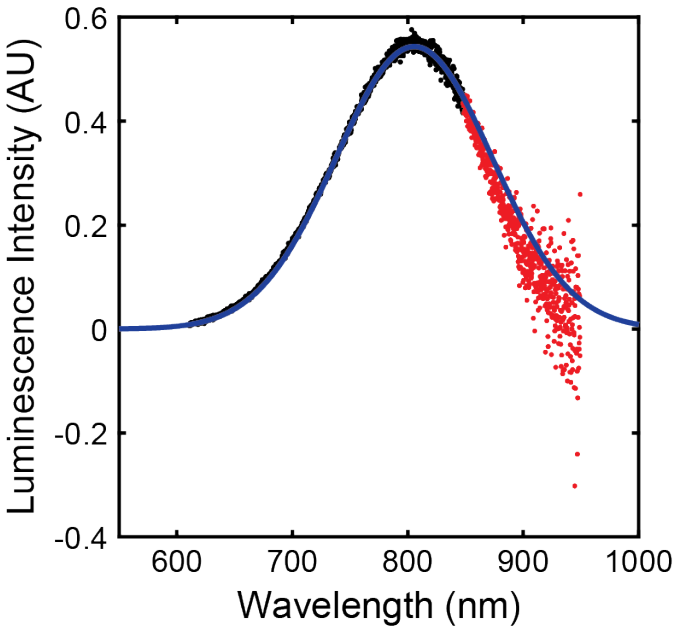

Figure 8.9: Representative wavelength vs. photoluminescence spectrum (black dots) and corresponding fit (blue line). Red dots correspond to photoluminescence data that was excluded due to increasing noise after 850 nm from the detector.

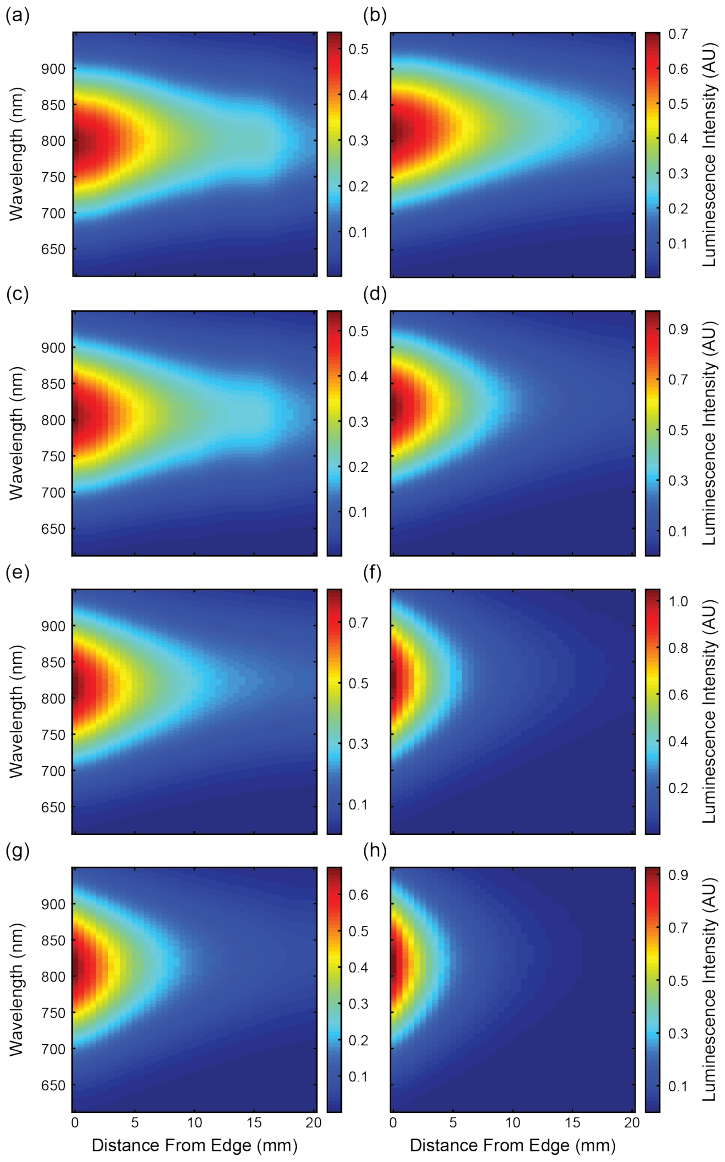

Figure 8.10: Gaussian fits of luminescence intensity as a function of wavelength and distance from collection edge for (left) ester-Si and (right) alkane-Si at a loading fraction of (a,b) 0.06 wt %, (c,d) 0.10 wt %, (e,f) 0.15 wt %, (g,h) 0.25 wt %.

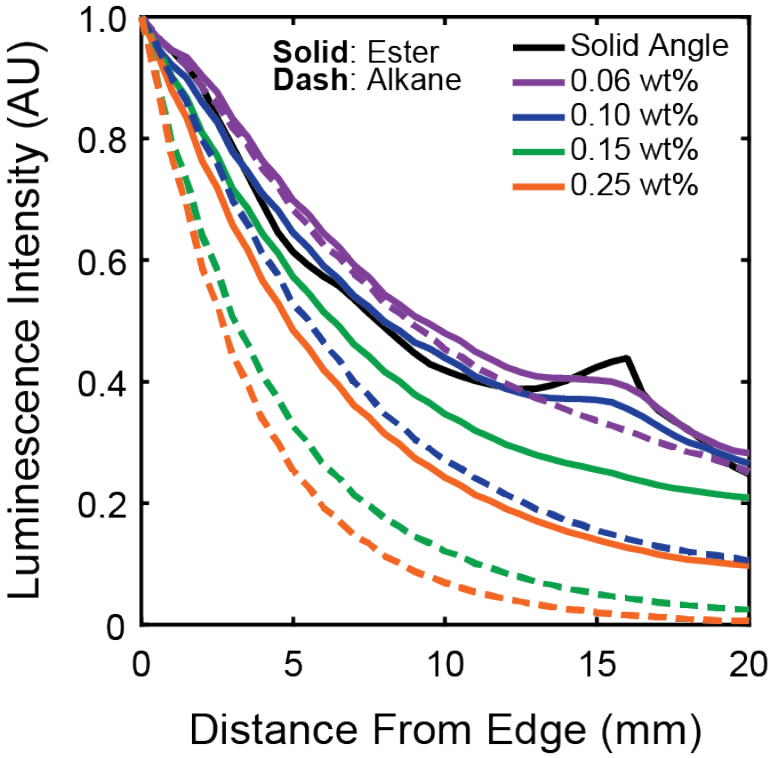

Figure 8.11: Attenuation of emitted light in Si QD/PMMA composites excited by a 405 nm laser rastered from 0 to 20 mm from the collection edge. The peak emission intensity of attenuating light through ester-Si QD/PMMA slabs (solid lines) and alkane-Si QD/PMMA slabs (dashed) is measured for particle loading fractions from 0.06 wt % (purple) to 0.25 wt % (orange). A calculation of the dependence of the solid angle for attenuation is shown in black.

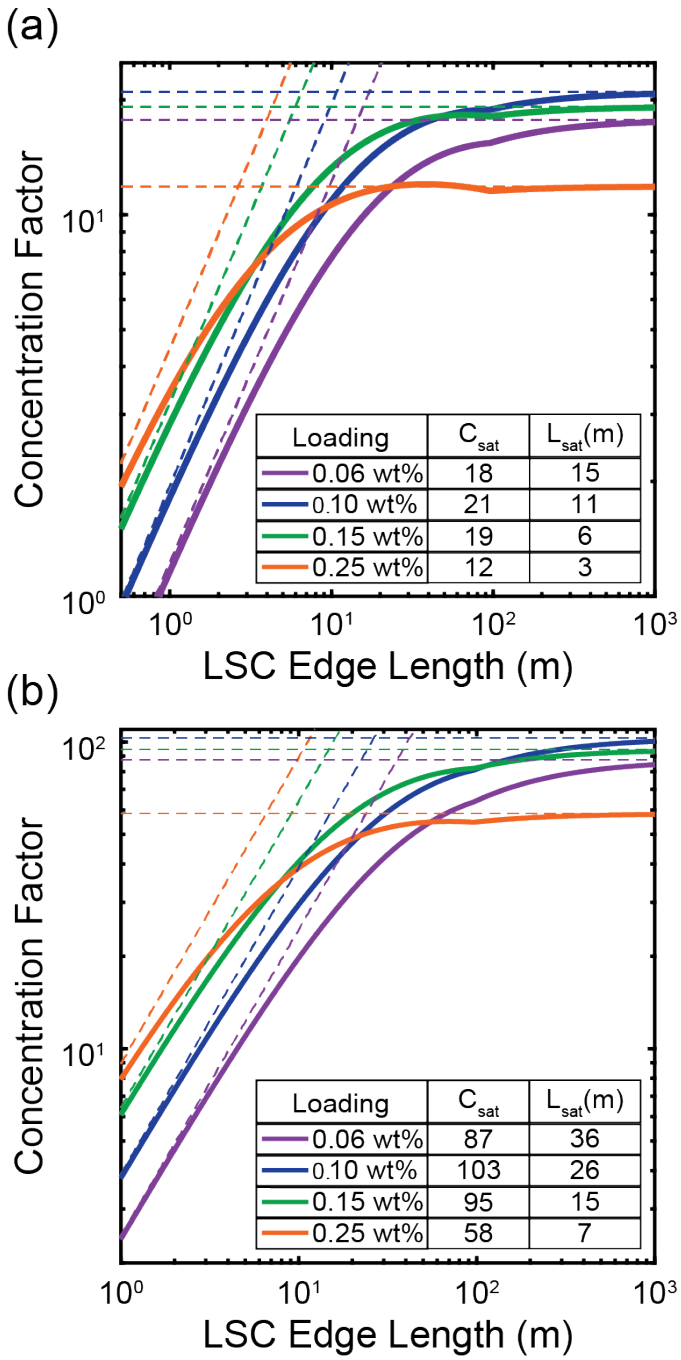

Figure 8.12: Predicted concentration factors as a function of side length for Si QDs loaded at 0.06 wt % (purple), 0.10 wt % (blue), 0.15 wt % (green), and 0.25 wt % (orange) and single particle scattering. (a) shows optimal concentration factors for 50% photoluminescence quantum yield and (b) shows optimal concentration factors for 100% photoluminescence quantum yield.

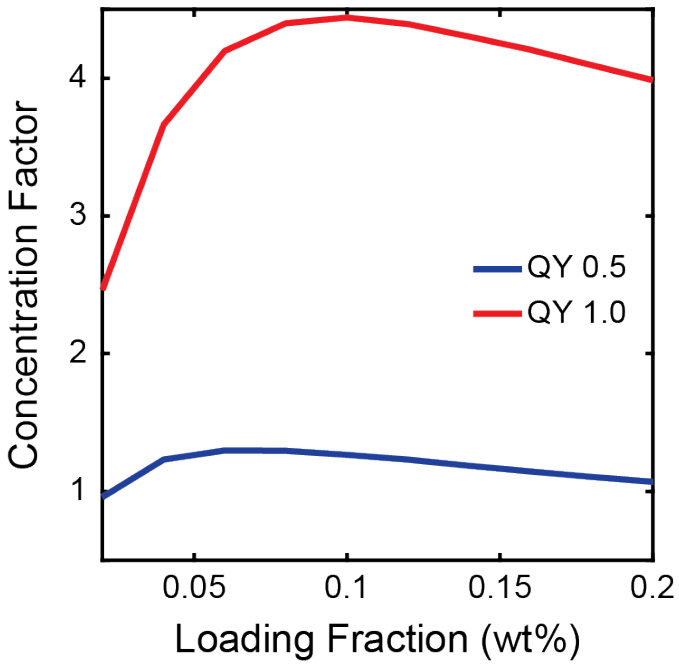

Figure 8.13: Simulated concentration factor as a function of loading fraction for a 3 mm thick LSC and a 1 m side length.

Chapter 9

Summary and Outlook

The purpose of this thesis is to show recent work performed to design, fabricate, and characterize luminescent solar concentrators as well as nanophotonic designs to improve light guiding in LSCs. We have designed spectrally-selective mirrors, reflective metasurfaces, and modified the photonic local density of states in LSCs to control the optical transport of the emitted light. We have also developed ray-tracing and analytical models to predict the performance of LSCs with these different photonic designs. In addition to design and modeling efforts, we have also fabricated visibly transparent Si and CdSe/CdS quantum dot polymer composites and characterized their properties for use as transparent light harvesting designs in BIPV. Control of optical transport in both thin film and bulk LSCs provides an exciting path way to improved light guiding in the concentrator design, relaxed constraints on luminophores for LSCs, and possible implementation of LSC into building integrated designs.

9.1 Summary

In Chapter 4 we designed a series of spectrally-selective top mirrors for LSCs to explore how to optimally balance the transmission of incident sunlight with the reflection of emitted light for different LSC parameters. This study determined that priority should be given to

the transmission of incident light when the concentrators have a large loading fraction of luminohpores, when the lateral size is small, or when there is significant overlap between the absorption and emission spectra. Priority should be given to the reflection of emitted light when the luminophore has high quantum yield, the loading fraction of luminophores is lower, the lateral size is large, or there is low overlap between the absorption and emission spectra. We also showed that emission weighted spectrally selective mirrors are necessary for the highest overall concentration factors as they are favored when photon recycling events occur to keep light within the concentrator.

Chapter 5 compares the performance predicted for photonic architectures that trap the luminescent light within the LSC and shows the importance of coupling light into the total internal reflection modes. In order to shift emitted light into TIR modes or modes with directional propagation towards the solar cell, phase shifting reflective metasurfaces are designed that reflect light according to generalized Snell's law. Monte Carlo ray-tracing calculations of LSCs with these reflective metasurfaces and wavelength-selective mirrors on the top and bottom indicate that the use of mirrors that direct the emitted light would lead to significantly higher concentration factors than a wavelength-selective mirror by itself or a standard concentrator.

In Chapter 6 we designed another type of nanophotonic design to improve light guiding in LSCs by modifying the photonic local density of states of the luminophores to achieve highly directional emission. By embedding the luminophores in either the polymer or the titania layer of a 1D Bragg stack we observe a reduction in the escape cone losses compared to a standard open top concentrator for luminophores embedded in each of the layers within the stack. Along with reduced escape cone losses we observe that most of the emitted light propagates within the polymer layer for luminophores embedded in the polymer or titania layer.

In Chapter 7 we fabricated well-dispersed CdSe/CdS core/shell QDs embedded in PCHE,

a derivative of the commodity polymer polystyrene. These composites show little visible light scattering and have similar optical properties to QD/PLMA composites currently found in literature. This fabrication process provides a pathway for high quality nanoscale LSCs, which will open up exciting optical techniques and designs to control the optical transport in thin film LSCs.

Finally, 2e investigate the optical properties of Si QD / PMMA composites in Chapter 8. By utilizing a ligand that has structural similarity to the repeat unit in PMMA we achieve composites with no visible light scattering for luminophore loading fractions of 0.06 and 0.10 wt%. In general, the scattering properties of the ester-Si / PMMA composites are significantly reduced compared to alkane-Si / PMMA composites, which leads to reduced visible haze, diffuse reflection, and longer attenuation lengths. These studies show that ester-Si / PMMA composites may be attractive for future low-scattering window-scale LSCs.

9.2 Outlook

9.2.1 Optics of Nanoscale Thin Film LSCs

The ability to coat LSCs through thin film processing methods is very advantageous for the implementation of LSC technology in currently underutilized areas for solar harvesting. However, these progressively thinner LSCs cannot be effectively modeled by ray-tracing methods. As the thickness of the LSCs approach the wavelength of the absorbed and emitted light, the interaction between the light and the LSC structure must be modeled with wave-optics methods as described in Chapter 6. Therefore, to fully model the properties of nanoscale LSCs, new models must be created that combine the FDTD and Monte Carlo ray-tracing method to accurately model the behavior of the thin film as well as the propagation of light throughout the full concentrator.

The combined FDTD ray-tracing model will provide a method to answer many currently unanswered questions for how the properties of LSCs change when the thickness is on the order of the wavelength of light. As the thickness of the concentrator decreases the quantum dots embedded within the concentrator will have a significantly large impact on the refractive index of the composite as opposed to the bulk concentrator. In Chapter 7 we observed an increase in refractive index up to 0.1 for loading fraction up to 30 mg/mL. The modification of the thin film refractive index will likely affect the emission properties of the QDs within the composite. Further study of this modification may provide further insight into the best loading fractions and substrates required for efficient light guiding within the design.

While these thin film LSCs may be advantageous for implementation of LSC technology, they will likely absorb only a small fraction of the incident solar spectrum due to their reduced optical density. Therefore, designs that improve the absorption within the luminescent film will likely be need to achieve maximum concentration factors. When designing a structure for this purpose it is likely important to retain the visible transmittance of the LSC as this would likely be utilized in an application where transparency is important. A possible method to improve absorption within the thin film LSC is to apply a dielectric metasurface to the back of the thin film. An example of a possible metasurface is shown in Figure 9.1. A dielectric metasurface, unlike the metallic metasurfaces described in Chapter 5, uses a periodic array of dielectric materials in order to control the phase of the reflected light. The use of dielectrics reduces the losses due to luminophore metal quenching and may be able to retain their transparency over the visible spectrum. In study of these metasurfaces it will be important to also study the affect of the metasurface on emitted light guiding as the best metasurface may not be the one that allows the LSC to absorb the most light. It will be important to balance the affect of the metasurface on incident light absorption and emitted light guiding.

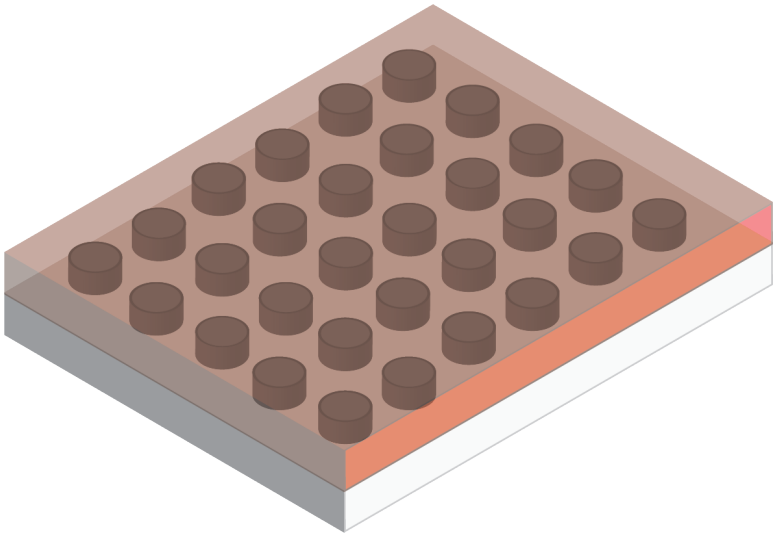

Figure 9.1: Schematic of dielectric metasurface embedded into thin film LSC.

9.2.2 Fabrication of Tandem LSCs

While LSCs can effectively downshift and concentrate light onto solar cells mounted at the edge when photonic designs are utilized, the total light guided is still limited by the absorption spectrum of the luminophore. Tandem LSCs present a possible solution to expand the incident sunlight that can be converted into electricity. These LSCs can be configured in multiple ways including a LSC layered on top of a silicon solar cell [138], a stack of LSCs separated by an air gap [155, 156], and a stack of thin film LSCs on a substrate [157].

CdSe/CdS core/shell quantum dots and Si quantum dots make an advantageous pair of luminophores as CdSe/CdS quantum dots efficiently convert UV light to approximately 630 nm, while the Si QDs can absorb light with lower energies and convert to light around 850 nm. Fabrication of this tandem structure should be simple as preliminary experiments have shown that thin films of Si / PMMA can be deposited using a doctor blade approach with polar solvents and the CdSe/CdS PCHE thin films can be deposited using spin coating with nonpolar solvents. A schematic of this design is shown in Figure 9.2. This orthogonal solvent approach should allow for deposition of unique composites without interpenetration

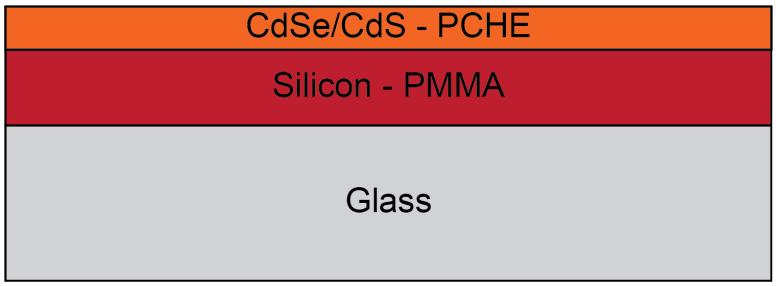

Figure 9.2: Schematic of CdSe/CdS and Si tandem LSC

of the QD material. Further studies are necessary to determine how the thickness of each layer, optical density, and configuration of the stack affect the absorption and waveguiding efficiency of the LSC.

9.2.3 Fabrication of High and Low Refractive Index Stack to Control Luminophore Emission

As shown in Chapter 6 directional emission can be achieved by embedding luminophores in the layers of a photonic design. Successful fabrication of these designs would provide a pathway toward a high OD concentrator with improved light guiding, which would be advantageous in applications that require thin film LSCs. However, the fabrication of these designs is not trivial and some fabrication issues must be solved to create high quality photonic LSCs. Even though the CdSe/CdS core/shell quantum dots are resistant to high temperature they are likely not resistance to the temperatures required for evaporation deposition of high refractive index materials. Therefore, all-solution based processing may be the best pathway toward a photonic LSC. However, sol-gel processes to produce the titania, which would likely serve as the high refractive index layer, give relatively low refractive indices without exposure to high temperatures. A study of film refractive index for different sol-gel processes to produce dielectrics of high refractive index may give insight on methods to produce high refractive index materials at room temperature.

Preliminary experiments of stacked CdSe/CdS in PCHE and titania films have showed

a significant increase in the reflection and scattering compared to what would be expected theoretically for the thin film stack. This anomalous reflection and scattering may reduce the light that can be absorbed by the concentrator and the light that can be guided to the edge respectively, which would be detrimental to performance. Studies that characterize the roughness, refractive index, and thickness of the stacked structures should provide insight on the best practices to produce uniform stacked structures.

9.3 Conclusions

Recently luminescent solar concentrators have seen a resurgence in research as new luminophores have been created and photonic designs have been implemented to work towards reducing the cost per Watt of solar technology. Controlling the optical transport of incident and emitted light will continue to play a key role in designing concentrators that effectively concentrate light. This work has developed design criteria for spectrally-selective top mirrors and reflective metasurfaces to trap and guide the emitted light over to the edge, while transmitting enough of the solar spectrum to be absorbed be the concentrator. While this criteria was developed for CdSe/CdS core/shell particles, it should be transferable to other dye and QD systems. In addition, we have shown the ability to control scattering losses in Si / PMMA concentrators by changing the surface of the Si QD, which reduce losses in large area Si based concentrators. This work shows that through careful control of the light transport through LSCs significant gains in the concentration factor are observed, providing a pathway for utilizing tailored nanophotonic designs improve LSC performance in a variety of applications.

Bibliography

[1] N. D. Bronstein, L. Li, L. Xu, Y. Yao, V. E. Ferry, A. P. Alivisatos, and R. G. Nuzzo, "Luminescent solar concentration with semiconductor nanorods and transfer-printed micro-silicon solar cells." ACS nano **8**, 44–53 (2014).

[2] J. Gutmann, M. Peters, B. Bläsi, M. Hermle, A. Gombert, H. Zappe, and J. C. Goldschmidt, "Electromagnetic simulations of a photonic luminescent solar concentrator." Optics express **20 Suppl 2**, A157–67 (2012).

[3] "Solar Industry Data — SEIA https://www.seia.org/solar-industry-data," Tech. rep.

[4] W. H. Weber and J. Lambe, "Luminescent greenhouse collector for solar radiation." Applied optics **15**, 2299–300 (1976).

[5] A. Goetzberger and W. Greube, "Solar energy conversion with fluorescent collectors," Applied Physics **14**, 123–139 (1977).

[6] V. Wittwer, K. Heidler, A. Zastrow, and A. Goetzberger, "Theory of fluorescent planar concentrators and experimental results," Journal of Luminescence **24-25**, 873–876 (1981).

[7] A. Luque and S. Hegedus, eds., *Handbook of Photovoltaic Science and Engineering* (John Wiley & Sons, Ltd, Chichester, UK, 2010).

[8] E. Yablonovitch, "Thermodynamics of the fluorescent planar concentrator," Journal of the Optical Society of America **70**, 1362–1363 (1980).

[9] T. Markvart, "The thermodynamics of optical étendue," Journal of Optics A: Pure and Applied Optics **10**, 015008 (2008).

[10] R. Reisfeld, "New developments in luminescence for solar energy utilization," Optical Materials **32**, 850–856 (2010).

[11] E. Klampaftis, D. Ross, K. R. McIntosh, and B. S. Richards, "Enhancing the performance of solar cells via luminescent down-shifting of the incident spectrum: A review," Solar Energy Materials and Solar Cells **93**, 1182–1194 (2009).

[12] B. Richards, "Enhancing the performance of silicon solar cells via the application of passive luminescence conversion layers," Solar Energy Materials and Solar Cells **90**, 2329–2337 (2006).

[13] F. Meinardi, H. McDaniel, F. Carulli, A. Colombo, K. A. Velizhanin, N. S. Makarov, R. Simonutti, V. I. Klimov, and S. Brovelli, "Highly efficient large-area colourless luminescent solar concentrators using heavy-metal-free colloidal quantum dots," Nature Nanotechnology **10**, 878–885 (2015).

[14] F. Meinardi, S. Ehrenberg, L. Dhamo, F. Carulli, M. Mauri, F. Bruni, R. Simonutti, U. Kortshagen, and S. Brovelli, "Highly efficient luminescent solar concentrators based on earth-abundant indirect-bandgap silicon quantum dots," Nature Photonics **11**, 177–185 (2017).

[15] H. Li, K. Wu, J. Lim, H.-J. Song, and V. I. Klimov, "Doctor-blade deposition of quantum dots onto standard window glass for low-loss large-area luminescent solar concentrators," Nature Energy **1**, 16157 (2016).

[16] M. R. Bergren, N. S. Makarov, K. Ramasamy, A. Jackson, R. Guglielmetti, and H. McDaniel, "High-Performance CuInS2 Quantum Dot Laminated Glass Luminescent Solar Concentrators for Windows," ACS Energy Letters **3**, 520–525 (2018).

[17] M. G. Debije and P. P. C. Verbunt, "Thirty Years of Luminescent Solar Concentrator Research: Solar Energy for the Built Environment," Advanced Energy Materials **2**, 12–35 (2012).

[18] F. M. Vossen, M. P. Aarts, and M. G. Debije, "Visual performance of red luminescent solar concentrating windows in an office environment," Energy and Buildings **113**, 123–132 (2016).

[19] F. Purcell-Milton and Y. K. Gun'ko, "Quantum dots for Luminescent Solar Concentrators," Journal of Materials Chemistry **22**, 16687–16697 (2012).

[20] L. R. Bradshaw, K. Knowles, S. McDowall, and D. R. Gamelin, "Nanocrystals for Luminescent Solar Concentrators," Nano Letters **15**, 13151323 (2015).

[21] V. Sholin, J. D. Olson, and S. A. Carter, "Semiconducting polymers and quantum dots in luminescent solar concentrators for solar energy harvesting," Journal of Applied Physics **101**, 123114 (2007).

[22] J. Bomm, A. Büchtemann, A. J. Chatten, R. Bose, D. J. Farrell, N. L. Chan, Y. Xiao, L. H. Slooff, T. Meyer, A. Meyer, W. G. van Sark, and R. Koole, "Fabrication and full characterization of state-of-the-art quantum dot luminescent solar concentrators," Solar Energy Materials and Solar Cells **95**, 2087–2094 (2011).

[23] F. Meinardi, A. Colombo, K. A. Velizhanin, R. Simonutti, M. Lorenzon, L. Beverina, R. Viswanatha, V. I. Klimov, and S. Brovelli, "Large-area luminescent solar concentrators based on 'Stokes-shift-engineered' nanocrystals in a mass-polymerized PMMA matrix," Nature Photonics **8**, 392–399 (2014).

[24] I. Coropceanu and M. G. Bawendi, "Core/Shell Quantum Dot Based Luminescent Solar Concentrators with Reduced Reabsorption and Enhanced Efficiency," Nano Letters **14**, 4097–4101 (2014).

[25] N. D. Bronstein, Y. Yao, L. Xu, E. O'Brien, A. S. Powers, V. E. Ferry, A. P. Alivisatos, and R. G. Nuzzo, "Quantum Dot Luminescent Concentrator Cavity Exhibiting 30-fold Concentration," ACS Photonics **2**, 1576–1583 (2015).

[26] G. Zaiats, D. Yanover, R. Vaxenburg, J. Tilchin, A. Sashchiuk, and E. Lifshitz, "PbSe-Based Colloidal Core/Shell Heterostructures for Optoelectronic Applications," Materials **7**, 7243–7275 (2014).

[27] B. Rowan, L. Wilson, and B. Richards, "Advanced Material Concepts for Luminescent Solar Concentrators," IEEE Journal of Selected Topics in Quantum Electronics **14**, 1312–1322 (2008).

[28] I. Papakonstantinou and C. Tummeltshammer, "Fundamental limits of concentration in luminescent solar concentrators revised: the effect of reabsorption and nonunity quantum yield," Optica **2**, 841 (2015).

[29] K. W. Boer, "The physics of solar cells," Journal of Applied Physics **50**, 5356 (1979).

[30] W. Shockley and H. J. Queisser, "Detailed Balance Limit of Efficiency of p-n Junction Solar Cells," Journal of Applied Physics **32**, 510 (1961).

[31] A. D. Vos, "Detailed balance limit of the efficiency of tandem solar cells," Journal of Physics D: Applied Physics **13**, 839–846 (1980).

[32] T. Trupke, M. a. Green, and P. Wurfel, "Improving solar cell efficiencies by down-conversion of high-energy photons," Journal of Applied Physics **92**, 1668 (2002).

[33] I. M. Slauch, M. G. Deceglie, T. J. Silverman, and V. E. Ferry, "Spectrally Selective Mirrors with Combined Optical and Thermal Benefit for Photovoltaic Module Thermal Management," ACS Photonics **5**, 1528–1538 (2018).

[34] D. Dirnberger, G. Blackburn, B. Müller, and C. Reise, "On the impact of solar spectral irradiance on the yield of different PV technologies," Solar Energy Materials and Solar Cells **132**, 431–442 (2015).

[35] F. Meinardi, F. Bruni, and S. Brovelli, "Luminescent solar concentrators for building-integrated photovoltaics," Nature Reviews Materials **2**, 17072 (2017).

[36] M. G. Debije and V. A. Rajkumar, "Direct versus indirect illumination of a prototype luminescent solar concentrator," Solar Energy **122**, 334–340 (2015).

[37] W. van Sark, P. Moraitis, C. Aalberts, M. Drent, T. Grasso, Y. L'Ortije, M. Visschers, M. Westra, R. Plas, and W. Planje, "The Electric Mondrian as a Luminescent Solar Concentrator Demonstrator Case Study," Solar RRL **1**, 1600015 (2017).

[38] N. Aste, L. Tagliabue, C. Del Pero, D. Testa, and R. Fusco, "Performance analysis of a large-area luminescent solar concentrator module," Renewable Energy **76**, 330–337 (2015).

[39] M. Kanellis, M. M. de Jong, L. Slooff, and M. G. Debije, "The solar noise barrier project: 1. Effect of incident light orientation on the performance of a large-scale luminescent solar concentrator noise barrier," Renewable Energy **103**, 647–652 (2017).

[40] U. Energy Information Administration, "Monthly Energy Review March 2019," Tech. rep. (2019).

[41] J. Ingle and S. Crouch, *Spectrochemical Analysis* (Prentice Hall, New Jersey, 1988).

[42] X. Huang, S. Han, W. Huang, and X. Liu, "Enhancing solar cell efficiency: the search for luminescent materials as spectral converters." Chemical Society reviews **42**, 173–201 (2013).

[43] A. Jablonski, "Efficiency of Anti-Stokes Fluorescence in Dyes," Nature **131**, 839–840 (1933).

[44] V. I. Klimov, T. A. Baker, J. Lim, K. A. Velizhanin, and H. McDaniel, "Quality Factor of Luminescent Solar Concentrators and Practical Concentration Limits Attainable with Semiconductor Quantum Dots," ACS Photonics **3**, 1138–1148 (2016).

[45] E. Hecht, *Optics* (Dorling Kindersley, New Delhi, 2001), 4th ed.

[46] J. H. Lambert and D. DiLaura, *Photometria,* (Illuminating Engineering Society of North America, Boulder, 2001).

[47] W. G. J. H. M. van Sark, K. W. J. Barnham, L. H. Slooff, A. J. Chatten, A. Büchtemann, A. Meyer, S. J. McCormack, R. Koole, D. J. Farrell, R. Bose, E. E. Bende, A. R. Burgers, T. Budel, J. Quilitz, M. Kennedy, T. Meyer, C. D. M. Donegá, A. Meijerink, and D. Vanmaekelbergh, "Luminescent Solar Concentrators–a review of recent results." Optics express **16**, 21773–92 (2008).

[48] A. Al Salman, A. Tortschanoff, G. van der Zwan, F. van Mourik, and M. Chergui, "A model for the multi-exponential excited-state decay of CdSe nanocrystals," Chemical Physics **357**, 96–101 (2009).

[49] M. Zettl, O. Mayer, E. Klampaftis, and B. S. Richards, "Investigation of Host Polymers for Luminescent Solar Concentrators," Energy Technology **5**, 1037–1044 (2017).

[50] M. J. Kastelijn, C. W. Bastiaansen, and M. G. Debije, "Influence of waveguide material on light emission in luminescent solar concentrators," Optical Materials **31**, 1720–1722 (2009).

[51] N. Tanio and Y. Koike, "What Is the Most Transparent Polymer?" Polymer Journal **32**, 43–50 (2000).

[52] Y. Koike, N. Tanio, and Y. Ohtsuka, "Light scattering and heterogeneities in low-loss poly(methyl methacrylate) glasses," Macromolecules **22**, 1367–1373 (1989).

[53] J. D. Joannopoulos, S. G. Johnson, J. N. Winn, and R. D. Meade, *Photonic Crystals* (Princeton University Press, Princeton, 2007), 2nd ed.

[54] J. C. Goldschmidt, M. Peters, L. Prönneke, L. Steidl, R. Zentel, B. Bläsi, A. Gombert, S. Glunz, G. Willeke, and U. Rau, "Theoretical and experimental analysis of photonic structures for fluorescent concentrators with increased efficiencies," Physica Status Solidi (a) **205**, 2811–2821 (2008).

[55] U. Rau, F. Einsele, and G. C. Glaeser, "Efficiency limits of photovoltaic fluorescent collectors," Applied Physics Letters **87**, 171101 (2005).

[56] J. C. Goldschmidt, M. Peters, A. Bösch, H. Helmers, F. Dimroth, S. W. Glunz, and G. Willeke, "Increasing the efficiency of fluorescent concentrator systems," Solar Energy Materials and Solar Cells **93**, 176–182 (2009).

[57] N. D. Bronstein, L. Li, L. Xu, Y. Yao, V. E. Ferry, a. P. Alivisatos, and R. G. Nuzzo, "Luminescent solar concentration with semiconductor nanorods and transfer-printed micro-silicon solar cells." ACS nano **8**, 44–53 (2014).

[58] L. Xu, Y. Yao, N. D. Bronstein, L. Li, A. P. Alivisatos, and R. G. Nuzzo, "Enhanced Photon Collection in Luminescent Solar Concentrators with Distributed Bragg Reflectors," ACS Photonics **3**, 278–285 (2016).

[59] E. Yablonovitch, "Inhibited Spontaneous Emission in Solid-State Physics and Electronics," Physical Review Letters **58**, 2059–2062 (1987).

[60] V. P. Bykov, "Spontaneous Emission in a Periodic Structure," Soviet Journal of Experimental and Theoretical Physics **35** (1972).

[61] I. Rousseau and V. Wood, "Nanophotonic luminescent solar concentrators," Applied Physics Letters **103**, 131113 (2013).

[62] J. M. Drake, M. L. Lesiecki, J. Sansregret, and W. R. L. Thomas, "Organic dyes in PMMA in a planar luminescent solar collector: a performance evaluation," Applied Optics **21**, 2945–2952 (1982).

[63] A. Zastrow, "Physics and applications of fluorescent concentrators: a review," (International Society for Optics and Photonics, 1994), vol. 2255, pp. 534–547.

[64] G. Seybold and G. Wagenblast, "New perylene and violanthrone dyestuffs for fluorescent collectors," Dyes and Pigments **11**, 303–317 (1989).

[65] M. El-Shahawy and A. Mansour, "Optical properties of some luminescent solar concentrators," Journal of Materials Science: Materials in Electronics **7**, 171–174 (1996).

[66] M. G. Debije, M.-P. Van, P. P. C. Verbunt, M. J. Kastelijn, R. H. L. van der Blom, D. J. Broer, and C. W. M. Bastiaansen, "Effect on the output of a luminescent solar concentrator on application of organic wavelength-selective mirrors." Applied optics **49**, 745–51 (2010).

[67] M. G. Debije, J.-P. Teunissen, M. J. Kastelijn, P. P. Verbunt, and C. W. Bastiaansen, "The effect of a scattering layer on the edge output of a luminescent solar concentrator," Solar Energy Materials and Solar Cells **93**, 1345–1350 (2009).

[68] M. G. Debije, P. P. C. Verbunt, B. C. Rowan, B. S. Richards, and T. L. Hoeks, "Measured surface loss from luminescent solar concentrator waveguides," Applied Optics **47**, 6763–6768 (2008).

[69] "Collector dyes Technical Information Lumogen F Colorants and Graphic Systems," Tech. rep.

[70] X. Tong, X.-T. Kong, Y. Zhou, F. Navarro-Pardo, G. S. Selopal, S. Sun, A. O. Govorov, H. Zhao, Z. M. Wang, and F. Rosei, "Near-Infrared, Heavy Metal-Free Colloidal Giant Core/Shell Quantum Dots," Advanced Energy Materials **8**, 1701432 (2018).

[71] Z.-C. Yang, M. Wang, A. M. Yong, S. Y. Wong, X.-H. Zhang, H. Tan, A. Y. Chang, X. Li, and J. Wang, "Intrinsically fluorescent carbon dots with tunable emission derived from hydrothermal treatment of glucose in the presence of monopotassium phosphate," Chemical Communications **47**, 11615–11617 (2011).

[72] Z. A. Peng and X. Peng, "Formation of High-Quality CdTe, CdSe, and CdS Nanocrystals Using CdO as Precursor," Journal of the American Chemical Society **123**, 183–184 (2001).

[73] Sungjee Kim, Brent Fisher, Hans-Jürgen Eisler, and M. Bawendi, "Type-II Quantum Dots: CdTe/CdSe(Core/Shell) and CdSe/ZnTe(Core/Shell) Heterostructures," Journal of the American Chemical Society **125**, 11466–11467 (2003).

[74] C.-T. Cheng, C.-Y. Chen, C.-W. Lai, W.-H. Liu, S.-C. Pu, P.-T. Chou, Y.-H. Chou, and H.-T. Chiu, "Syntheses and photophysical properties of type-II CdSe/ZnTe/ZnS (core/shell/shell) quantum dots," Journal of Materials Chemistry **15**, 3409–3414 (2005).

[75] M. Brumer, A. Kigel, L. Amirav, A. Sashchiuk, O. Solomesch, N. Tessler, and E. Lifshitz, "PbSe/PbS and PbSe/PbSexS1-x Core/Shell Nanocrystals," Advanced Functional Materials **15**, 1111–1116 (2005).

[76] E. Lifshitz, M. Brumer, A. Kigel, A. Sashchiuk, M. Bashouti, M. Sirota, E. Galun, Z. Burshtein, A. Q. Le Quang, I. Ledoux-Rak, and J. Zyss, "Air-Stable PbSe/PbS and PbSe/PbSexS1-x CoreShell Nanocrystal Quantum Dots and Their Applications," Journal of Physical Chemistry B **110**, 25356–25365 (2006).

[77] P. Reiss, M. Protière, and L. Li, "Core/Shell semiconductor nanocrystals." Small (Weinheim an der Bergstrasse, Germany) **5**, 154–68 (2009).

[78] Y. Chen, J. Vela, H. Htoon, J. L. Casson, D. J. Werder, D. A. Bussian, V. I. Klimov, and J. A. Hollingsworth, "Giant Multishell CdSe Nanocrystal Quantum Dots with Suppressed Blinking," Journal of the American Chemical Society **130**, 5026–5027 (2008).

[79] D. A. Hanifi, N. D. Bronstein, B. A. Koscher, Z. Nett, J. K. Swabeck, K. Takano, A. M. Schwartzberg, L. Maserati, K. Vandewal, Y. van de Burgt, A. Salleo, and A. P. Alivisatos, "Redefining near-unity luminescence in quantum dots with photothermal threshold quantum yield." Science (New York, N.Y.) **363**, 1199–1202 (2019).

[80] Q. Li, T.-Y. Luo, M. Zhou, H. Abroshan, J. Huang, H. J. Kim, N. L. Rosi, Z. Shao, and R. Jin, "Silicon Nanoparticles with Surface Nitrogen: 90% Quantum Yield with Narrow Luminescence Bandwidth and the Ligand Structure Based Energy Law," ACS Nano **10**, 8385–8393 (2016).

[81] W.-S. Song and H. Yang, "Efficient White-Light-Emitting Diodes Fabricated from Highly Fluorescent Copper Indium Sulfide Core/Shell Quantum Dots," Chemistry of Materials **24**, 1961–1967 (2012).

[82] C. Li, W. Chen, D. Wu, D. Quan, Z. Zhou, J. Hao, J. Qin, Y. Li, Z. He, and K. Wang, "Large Stokes Shift and High Efficiency Luminescent Solar Concentrator Incorporated with CuInS 2 /ZnS Quantum Dots," Nature Publishing Group **5**, 17777 (2015).

[83] Y. Zhao and R. R. Lunt, "Transparent Luminescent Solar Concentrators for Large-Area Solar Windows Enabled by Massive Stokes-Shift Nanocluster Phosphors," Advanced Energy Materials **3**, 1143–1148 (2013).

[84] L. Tan, Y. Zhou, F. Ren, D. Benetti, F. Yang, H. Zhao, F. Rosei, M. Chaker, and D. Ma, "Ultrasmall PbS quantum dots: a facile and greener synthetic route and their high performance in luminescent solar concentrators," Journal of Materials Chemistry A **5**, 10250–10260 (2017).

[85] S. A. Ivanov, A. Piryatinski, J. Nanda, S. Tretiak, K. R. Zavadil, W. O. Wallace, D. Werder, and V. I. Klimov, "Type-II Core/Shell CdS/ZnSe Nanocrystals: Synthesis, Electronic Structures, and Spectroscopic Properties," Journal of the American Chemical Society **129**, 11708–11719 (2007).

[86] B. O. Dabbousi, J. Rodriguez-Viejo, F. V. Mikulec, J. R. Heine, H. Mattoussi, R. Ober, K. F. Jensen, and M. G. Bawendi, "(CdSe)ZnS CoreShell Quantum Dots: Synthesis and Characterization of a Size Series of Highly Luminescent Nanocrystallites," The Journal of Physical Chemistry B **101**, 9463–9475 (1997).

[87] O. Chen, X. Chen, Y. Yang, J. Lynch, H. Wu, J. Zhuang, and Y. Cao, "Synthesis of Metal-Selenide Nanocrystals Using Selenium Dioxide as the Selenium Precursor," Angewandte Chemie International Edition **47**, 8638–8641 (2008).

[88] C. Pu and X. Peng, "To Battle Surface Traps on CdSe/CdS Core/Shell Nanocrystals: Shell Isolation versus Surface Treatment," Journal of the American Chemical Society **138**, 8134–8142 (2016).

[89] R. Karel Čapek, I. Moreels, K. Lambert, D. De Muynck, Q. Zhao, A. Van Tomme, F. Vanhaecke, and Z. Hens, "Optical Properties of Zincblende Cadmium Selenide Quantum Dots," The Journal of Physical Chemistry C **114**, 6371–6376 (2010).

[90] R. J. Anthony, D. J. Rowe, M. Stein, J. Yang, and U. Kortshagen, "Routes to Achieving High Quantum Yield Luminescence from Gas-Phase-Produced Silicon Nanocrystals," Advanced Functional Materials **21**, 4042–4046 (2011).

[91] C. Meier, A. Gondorf, S. Lüttjohann, A. Lorke, and H. Wiggers, "Silicon nanoparticles: Absorption, emission, and the nature of the electronic bandgap," Journal of Applied Physics **101**, 103112 (2007).

[92] S. Pramanik, S. K. E. Hill, B. Zhi, N. V. Hudson-Smith, J. J. Wu, J. N. White, E. A. McIntire, V. S. S. K. Kondeti, A. L. Lee, P. J. Bruggeman, U. R. Kortshagen, and C. L. Haynes, "Comparative toxicity assessment of novel Si quantum dots and their traditional Cd-based counterparts using bacteria models Shewanella oneidensis and Bacillus subtilis," Environmental Science: Nano **5**, 1890–1901 (2018).

[93] K. Fujioka, M. Hiruoka, K. Sato, N. Manabe, R. Miyasaka, S. Hanada, A. Hoshino, R. D. Tilley, Y. Manome, K. Hirakuri, and K. Yamamoto, "Luminescent passive-oxidized silicon quantum dots as biological staining labels and their cytotoxicity effects at high concentration," Nanotechnology **19**, 415102 (2008).

[94] D. Sahin, B. Ilan, and D. F. Kelley, "Monte-Carlo simulations of light propagation in luminescent solar concentrators based on semiconductor nanoparticles," Journal of Applied Physics **110**, 033108 (2011).

[95] W. Schmidt, *Optical Spectroscopy in Chemistry and Life Sciences* (betz-druck GmbH, Darmstadt, Konstanz, 2005), 1st ed.

[96] J. R. Lakowicz, ed., *Principles of Fluorescence Spectroscopy* (Springer US, Boston, MA, 2006).

[97] S. Fery-Forgues and D. Lavabre, "Are Fluorescence Quantum Yields So Tricky to Measure? A Demonstration Using Familiar Stationery Products," Journal of Chemical Education **76**, 1260 (1999).

[98] C. Scott, *Introduction to Optics and Optical Imaging* (IEEE Press, Piscataway, 1998).

[99] A. Taflove, *Computational Electrodynamics* (Artech House, Northwood, 1995).

[100] D. K. G. de Boer, D. J. Broer, M. G. Debije, W. Keur, A. Meijerink, C. R. Ronda, and P. P. C. Verbunt, "Progress in phosphors and filters for luminescent solar concentrators." Optics express **20**, A395–405 (2012).

[101] D. K. G. de Boer, C.-W. Lin, M. P. Giesbers, H. J. Cornelissen, M. G. Debije, P. P. C. Verbunt, and D. J. Broer, "Polarization-independent filters for luminescent solar concentrators," Applied Physics Letters **98**, 021111 (2011).

[102] T. Markvart, "Detailed balance method for ideal single-stage fluorescent collectors," Journal of Applied Physics **99**, 026101 (2006).

[103] P. P. C. Verbunt, S. Tsoi, M. G. Debije, D. J. Boer, C. W. Bastiaansen, C.-W. Lin, and D. K. G. de Boer, "Increased efficiency of luminescent solar concentrators after application of organic wavelength selective mirrors," Optics Express **20**, A655–A668 (2012).

[104] R. Connell and V. E. Ferry, "Integrating Photonics with Luminescent Solar Concentrators: Optical Transport in the Presence of Photonic Mirrors," The Journal of Physical Chemistry C **120**, 20991–20997 (2016).

[105] J. C. Goldschmidt, M. Peters, M. Hermle, and S. W. Glunz, "Characterizing the light guiding of fluorescent concentrators," Journal of Applied Physics **105**, 114911 (2009).

[106] A. Bozzola, V. Robbiano, K. Sparnacci, G. Aprile, L. Boarino, A. Proto, R. Fusco, M. Laus, L. C. Andreani, and D. Comoretto, "A Multi-optical Collector of Sunlight Employing Luminescent Materials and Photonic Nanostructures," Advanced Optical Materials **4**, 147–155 (2016).

[107] C. Bronnbauer, J. Hornich, N. Gasparini, F. Guo, B. Hartmeier, N. A. Luechinger, C. Pflaum, C. J. Brabec, and K. Forberich, "Printable Dielectric Mirrors with Easily Adjustable and Well-Defined Reflection Maxima for Semitransparent Organic Solar Cells," Advanced Optical Materials **3**, 1424–1430 (2015).

[108] M. Anaya, A. Rubino, M. E. Calvo, and H. Míguez, "Solution processed high refractive index contrast distributed Bragg reflectors," Journal of Materials Chemistry C **4**, 4532–4537 (2016).

[109] D. Norris and M. Bawendi, "Measurement and assignment of the size-dependent optical spectrum in CdSe quantum dots," Physical Review B **53**, 16338–16346 (1996).

[110] D. V. Talapin, J. H. Nelson, E. V. Shevchenko, S. Aloni, B. Sadtler, and a. P. Alivisatos, "Seeded growth of highly luminescent CdSe/CdS nanoheterostructures with rod and tetrapod morphologies." Nano letters **7**, 2951–9 (2007).

[111] J. Bomm, A. Büchtemann, A. Fiore, L. Manna, J. H. Nelson, D. Hill, and W. G. J. H. M. van Sark, "Fabrication and spectroscopic studies on highly luminescent CdSe/CdS nanorod polymer composites." Beilstein journal of nanotechnology **1**, 94–100 (2010).

[112] O. Chen, J. Zhao, V. P. Chauhan, J. Cui, C. Wong, D. K. Harris, H. Wei, H.-S. Han, D. Fukumura, R. K. Jain, and M. G. Bawendi, "Compact high-quality CdSe-CdS core-shell nanocrystals with narrow emission linewidths and suppressed blinking." Nature materials **12**, 445–51 (2013).

[113] C. Yang and R. R. Lunt, "Limits of Visibly Transparent Luminescent Solar Concentrators," Advanced Optical Materials **5**, 1600851 (2017).

[114] C. Wang, L. S. Hirst, and R. Winston, "Optical design and efficiency improvement for organic luminescent solar concentrators," (International Society for Optics and Photonics, 2011), vol. 8124, p. 81240O.

[115] S. J. Gallagher, P. C. Eames, and B. Norton, "Quantum dot solar concentrator behaviour, predicted using a ray trace approach," International Journal of Ambient Energy **25**, 47–56 (2004).

[116] M. Carrascosa, S. Unamuno, and F. Agullo-Lopez, "Monte Carlo simulation of the performance of PMMA luminescent solar collectors," Applied Optics **22**, 3236–3241 (1983).

[117] D. F. Swinehart, "The Beer-Lambert Law," Journal of Chemical Education **39**, 333 (1962).

[118] L. Wind and W. W. Szymanski, "Quantification of scattering corrections to the Beer-Lambert law for transmittance measurements in turbid media," Measurement Science and Technology **13**, 270–275 (2002).

[119] S. Larouche and L. Martinu, "OpenFilters: open-source software for the design, optimization, and synthesis of optical filters." Applied optics **47**, C219–30 (2008).

[120] J. Roncali and F. Garnier, "New luminescent back reflectors for the improvement of the spectral response and efficiency of luminescent solar concentrators," Solar Cells **13**, 133–143 (1984).

[121] B. N. Pal, Y. Ghosh, S. Brovelli, R. Laocharoensuk, V. I. Klimov, J. A. Hollingsworth, and H. Htoon, "Giant' CdSe/CdS Core/Shell Nanocrystal Quantum Dots As Efficient Electroluminescent Materials: Strong Influence of Shell Thickness on Light-Emitting Diode Performance," Nano Letters **12**, 331–336 (2012).

[122] Q. A. Akkerman, A. Genovese, C. George, M. Prato, I. Moreels, A. Casu, S. Marras, A. Curcio, A. Scarpellini, T. Pellegrino, L. Manna, and V. Lesnyak, "From Binary Cu2S to Ternary CuInS and Quaternary CuInZnS Nanocrystals with Tunable Composition via Partial Cation Exchange," ACS Nano **9**, 521–531 (2015).

[123] N. C. Giebink, G. P. Wiederrecht, and M. R. Wasielewski, "Resonance-shifting to circumvent reabsorption loss in luminescent solar concentrators," Nature Photonics **5**, 694–701 (2011).

[124] C. L. Mulder, P. D. Reusswig, a. M. Velázquez, H. Kim, C. Rotschild, and M. a. Baldo, "Dye alignment in luminescent solar concentrators: I. Vertical alignment for improved waveguide coupling." Optics express **18**, A79–90 (2010).

[125] C. L. Mulder, P. D. Reusswig, a. P. Beyler, H. Kim, C. Rotschild, and M. a. Baldo, "Dye alignment in luminescent solar concentrators: II. Horizontal alignment for energy harvesting in linear polarizers." Optics express **18**, A91–9 (2010).

[126] J. C. Goldschmidt, M. Peters, J. Gutmann, L. Steidl, R. Zentel, B. Bläsi, and M. Hermle, "Increasing Fluorescent Concentrator Light Collection Efficiency by Restricting the Angular Emission Characteristic of the Incorporated Luminescent Material - the "Nano-Fluko" Concept," **7725**, 77250S (2010).

[127] H. Hernandez-Noyola, D. H. Potterveld, R. J. Holt, and S. B. Darling, "Optimizing luminescent solar concentrator design," Energy & Environmental Science **5**, 5798–5802 (2012).

[128] A. Pors, O. Albrektsen, I. P. Radko, and S. I. Bozhevolnyi, "Gap plasmon-based metasurfaces for total control of reflected light," Scientific Reports **3**, 2155 (2013).

[129] S. Sun, K.-Y. Yang, W. T. Chen, C. Y. Liao, G.-Y. Guo, D. P. Tsai, C.-M. Wang, T.-K. Juan, W.-T. Kung, Q. He, S. Xiao, and L. Zhou, "Highly efficient anomalous reflection by an optical metasurface," SPIE Newsroom (2013).

[130] M. R. Khan, X. Wang, P. Bermel, and M. A. Alam, "Enhanced light trapping in solar cells with a meta-mirror following generalized Snell's law," Optics Express **22**, A973–A985 (2014).

[131] M. Esfandyarpour, E. C. Garnett, Y. Cui, M. D. McGehee, and M. L. Brongersma, "Metamaterial mirrors in optoelectronic devices," Nature Nanotechnology **9**, 542–547 (2014).

[132] L. Zou, M. López-García, W. Withayachumnankul, C. M. Shah, A. Mitchell, M. Bhaskaran, S. Sriram, R. Oulton, M. Klemm, and C. Fumeaux, "Spectral and angular characteristics of dielectric resonator metasurface at optical frequencies," Applied Physics Letters **105**, 191109 (2014).

[133] S. Jahani and Z. Jacob, "All-dielectric metamaterials," Nature Nanotechnology **11**, 23–36 (2016).

[134] W. G. van Sark, "Luminescent solar concentrators A low cost photovoltaics alternative," Renewable Energy **49**, 207–210 (2013).

[135] F. Meinardi, A. Colombo, K. A. Velizhanin, R. Simonutti, M. Lorenzon, L. Beverina, R. Viswanatha, V. I. Klimov, and S. Brovelli, "Large-area luminescent solar concentrators based on Stokes-shift-engineered' nanocrystals in a mass-polymerized PMMA matrix," Nature Photonics **8**, 392–399 (2014).

[136] L. J. Brennan, F. Purcell-Milton, B. McKenna, T. M. Watson, Y. K. Gun'ko, and R. C. Evans, "Large area quantum dot luminescent solar concentrators for use with dye-sensitised solar cells," Journal of Materials Chemistry A **6**, 2671–2680 (2018).

[137] G. Liu, H. Zhao, F. Diao, Z. Ling, and Y. Wang, "Stable tandem luminescent solar concentrators based on CdSe/CdS quantum dots and carbon dots," Journal of Materials Chemistry C **6**, 10059–10066 (2018).

[138] D. R. Needell, O. Ilic, C. R. Bukowsky, Z. Nett, L. Xu, J. He, H. Bauser, B. G. Lee, J. F. Geisz, R. G. Nuzzo, A. P. Alivisatos, and H. A. Atwater, "Design Criteria for Micro-Optical Tandem Luminescent Solar Concentrators," IEEE Journal of Photovoltaics **8**, 1560–1567 (2018).

[139] J. G. Kennemur, L. Yao, F. S. Bates, and M. A. Hillmyer, "Sub-5 nm Domains in Ordered Poly(cyclohexylethylene)-block-poly(methyl methacrylate) Block Polymers for Lithography," Macromolecules **47**, 1411–1418 (2014).

[140] D. L. Anderson, "Chemical Composition of the Mantle," Tech. rep. (1983).

[141] M. Dasog, J. Kehrle, B. Rieger, and J. G. C. Veinot, "Silicon Nanocrystals and Silicon-Polymer Hybrids: Synthesis, Surface Engineering, and Applications," Angewandte Chemie International Edition **55**, 2322–2339 (2016).

[142] Y. Li, S. Yu, J. G. C. Veinot, J. Linnros, L. Berglund, and I. Sychugov, "Luminescent Transparent Wood," Advanced Optical Materials **5**, 1600834 (2017).

[143] A. Marinins, Z. Yang, H. Chen, J. Linnros, J. G. C. Veinot, S. Popov, and I. Sychugov, "Photostable Polymer/Si Nanocrystal Bulk Hybrids with Tunable Photoluminescence," ACS Photonics **3**, 1575–1580 (2016).

[144] D. Chen, W. Sun, C. Qian, A. P. Y. Wong, L. M. Reyes, and G. A. Ozin, "UV-Blocking Photoluminescent Silicon Nanocrystal/Polydimethylsiloxane Composites," Advanced Optical Materials **5**, 1700237 (2017).

[145] A. Marinins, R. Zandi Shafagh, W. van der Wijngaart, T. Haraldsson, J. Linnros, J. G. C. Veinot, S. Popov, and I. Sychugov, "Light-Converting Polymer/Si Nanocrystal Composites with Stable 60-70% Quantum Efficiency and Their Glass Laminates," ACS Applied Materials & Interfaces **9**, 30267–30272 (2017).

[146] K. Sato, N. Fukata, K. Hirakuri, M. Murakami, T. Shimizu, and Y. Yamauchi, "Flexible and Transparent Silicon Nanoparticle/Polymer Composites with Stable Luminescence," Chemistry - An Asian Journal **5**, 50–55 (2010).

[147] Z. Yang, M. Dasog, A. R. Dobbie, R. Lockwood, Y. Zhi, A. Meldrum, and J. G. C. Veinot, "Highly Luminescent Covalently Linked Silicon Nanocrystal/Polystyrene Hybrid Functional Materials: Synthesis, Properties, and Processability," Advanced Functional Materials **24**, 1345–1353 (2014).

[148] M. Aghajamali, M. Iqbal, T. K. Purkait, L. Hadidi, R. Sinelnikov, and J. G. C. Veinot, "Synthesis and Properties of Luminescent Silicon Nanocrystal/Silica Aerogel Hybrid Materials," Chemistry of Materials **28**, 3877–3886 (2016).

[149] U. Ali, K. J. B. A. Karim, and N. A. Buang, "A Review of the Properties and Applications of Poly (Methyl Methacrylate) (PMMA)," Polymer Reviews **55**, 678–705 (2015).

[150] S. Wilcox and W. Marion, "Innovation for Our Energy Future Users Manual for TMY3 Data Sets," Tech. rep. (1994).

[151] S. A. Maier, *Plasmonics: Fundamentals and Applications* (Springer US, New York, NY, 2007).

[152] Y. Yu, C. M. Hessel, T. D. Bogart, M. G. Panthani, M. R. Rasch, and B. A. Korgel, "Room Temperature Hydrosilylation of Silicon Nanocrystals with Bifunctional Terminal Alkenes," Langmuir **29**, 1533–1540 (2013).

[153] X. Li, Y. He, and M. T. Swihart, "Surface Functionalization of Silicon Nanoparticles Produced by Laser-Driven Pyrolysis of Silane followed by HFHNO3 Etching," Langmuir **20**, 4720–4727 (2004).

[154] A. G173-03, "Standard Tables for Reference Solar Spectral Irradiances: Direct Normal and Hemispherical on 37 Tilted Surface," Tech. rep., ASTM International, West Conshohocken, PA (2012).

[155] K. Wu, H. Li, and V. I. Klimov, "Tandem luminescent solar concentrators based on engineered quantum dots," Nature Photonics **12**, 105–110 (2018).

[156] M. J. Currie, J. K. Mapel, T. D. Heidel, S. Goffri, and M. A. Baldo, "High-efficiency organic solar concentrators for photovoltaics." Science (New York, N.Y.) **321**, 226–8 (2008).

[157] T. A. Cohen, T. J. Milstein, D. M. Kroupa, J. D. MacKenzie, C. K. Luscombe, and D. R. Gamelin, "Quantum-cutting Yb3+-doped perovskite nanocrystals for monolithic bilayer luminescent solar concentrators," Journal of Materials Chemistry A **7**, 9279–9288 (2019).

Appendices

A Attenuation Measurement Setup

In the current iteration of the photoluminescence attenuation experiment the sample is excited by a high power fiber-coupled LED light source at 400 nm. The optical fiber is attached by Thor labs posts to a 50 mm compact motorized translation stage from Thor-Labs. The emitted light from the LSC that is guided to the edge enters a 1.25" x 4 mm hole in an integrating sphere for collection. The collected light passes through a 405 low pass filter and into an optical fiber for an OceanOptics Flame spectrometer to measure the photoluminescence. A photograph of the attenuation experiment is shown in Figure 1.

When performing the measurement the sample is scanned from approximately 3.5 mm away from the integrating sphere port (see Figure 2) to the edge of the sample. Prior to the measurement, the photoluminescence spectrum is collected at a few locations near the far edge of the sample to determine an integration time required to observe the photoluminescence at all excitation locations and figure out how far out to scan on the sample. If the excitation source overlaps with the edge of the sample too much then the intensity of the photoluminescence spectrum will increase due to scattering effects at the edge, which will give unphysical results. When the bounds of the experiment are determined a LabView program is used to perform the measurement. For most measurements I use a step size of 0.5 mm, 5 sweeps forwards and backwards, and a wait time of 5 seconds between each measurement. The wait time is important to ensure that the measurement is not taken while the stage is moving, which will cause the spectra to be a combination of multiple different

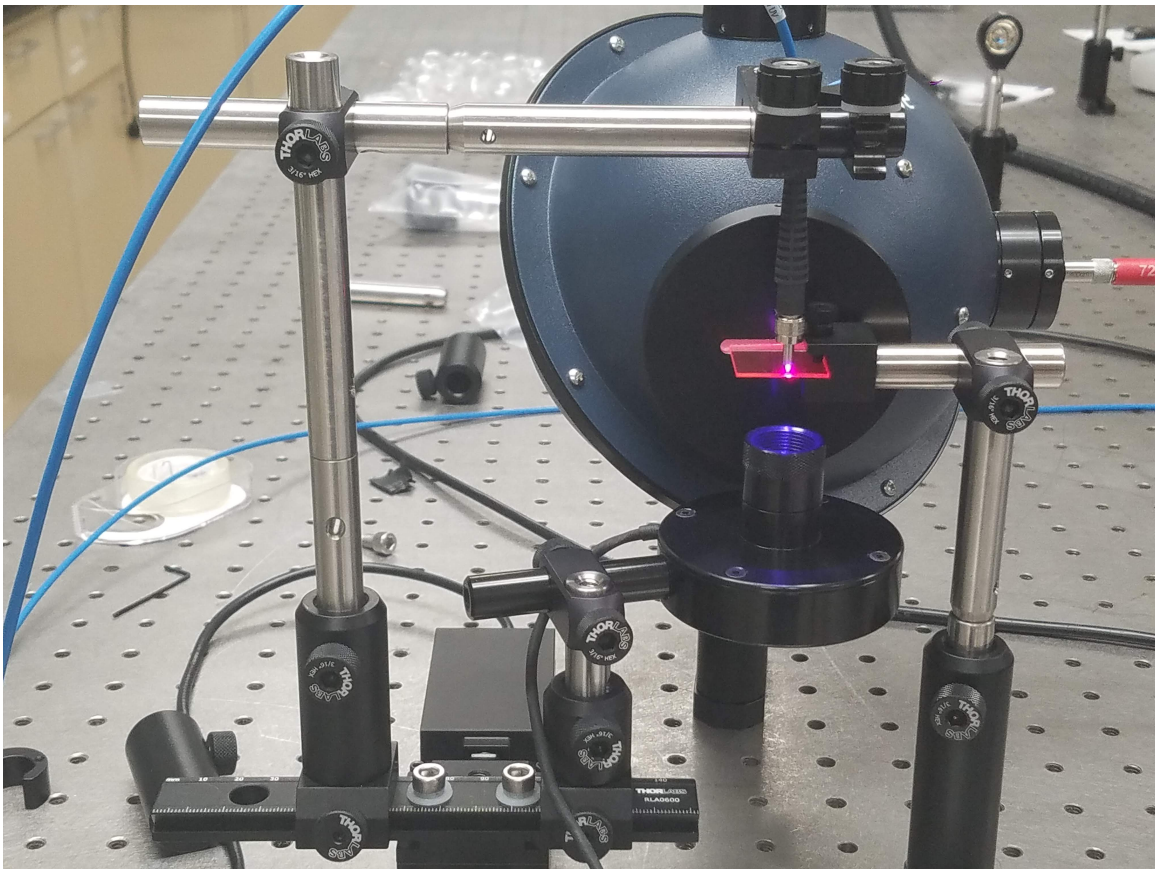

Figure 1: Photograph of attenuation experiment.

excitation locations.

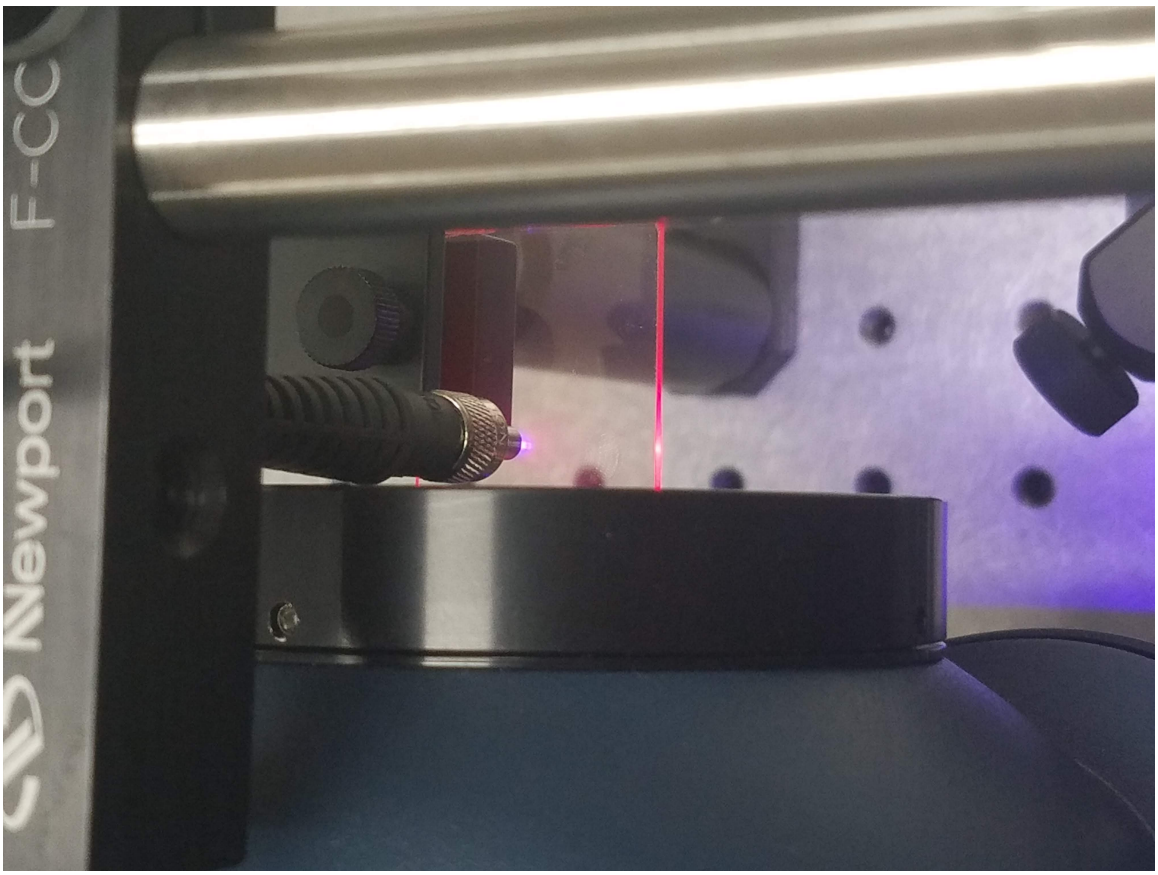

Figure 2: Photograph of attenuation experiment showing how close the the excitation source can approach the integrating sphere.

B Ellipsometry Raw Data

PCHE Film and 0.75 mg/mL QD/PCHE

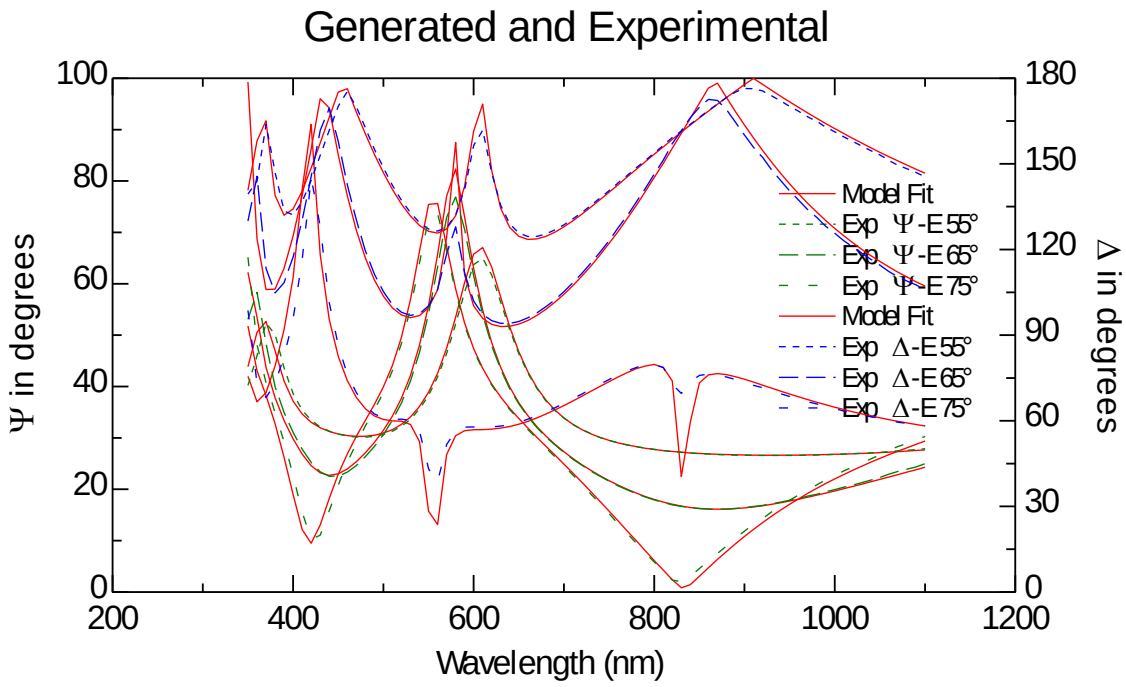

1	genosc	358.320 nm
0	si_jell	1 mm

MSE=33.02

Amp1.1	0.55353±0.00309
Wvl01.1	1.5224±0.00436

nm	n	k
350	1.51094573	0
360	1.51094529	0
370	1.51094488	0
380	1.51094451	0
390	1.51094416	0
400	1.51094385	0
410	1.51094355	0
420	1.51094327	0
430	1.51094302	0
440	1.51094278	0
450	1.51094255	0
460	1.51094235	0
470	1.51094215	0
480	1.51094197	0
490	1.51094179	0
500	1.51094163	0
510	1.51094148	0
520	1.51094133	0
530	1.5109412	0
540	1.51094107	0
550	1.51094095	0
560	1.51094083	0
570	1.51094072	0
580	1.51094062	0
590	1.51094052	0
600	1.51094043	0
610	1.51094034	0
620	1.51094026	0
630	1.51094017	0
640	1.5109401	0
650	1.51094002	0
660	1.51093995	0
670	1.51093989	0
680	1.51093982	0
690	1.51093976	0

700	1.5109397	0
710	1.51093965	0
720	1.51093959	0
730	1.51093954	0
740	1.51093949	0
750	1.51093944	0
760	1.5109394	0
770	1.51093936	0
780	1.51093931	0
790	1.51093927	0
800	1.51093923	0
810	1.5109392	0
820	1.51093916	0
830	1.51093912	0
840	1.51093909	0
850	1.51093906	0
860	1.51093903	0
870	1.510939	0
880	1.51093897	0
890	1.51093894	0
900	1.51093891	0
910	1.51093888	0
920	1.51093886	0
930	1.51093883	0
940	1.51093881	0
950	1.51093879	0
960	1.51093876	0
970	1.51093874	0
980	1.51093872	0
990	1.5109387	0
1000	1.51093868	0
1010	1.51093866	0
1020	1.51093864	0
1030	1.51093862	0
1040	1.51093861	0
1050	1.51093859	0
1060	1.51093857	0
1070	1.51093855	0
1080	1.51093854	0
1090	1.51093852	0
1100	1.51093851	0

Loading Fraction 2.5 mg/mL

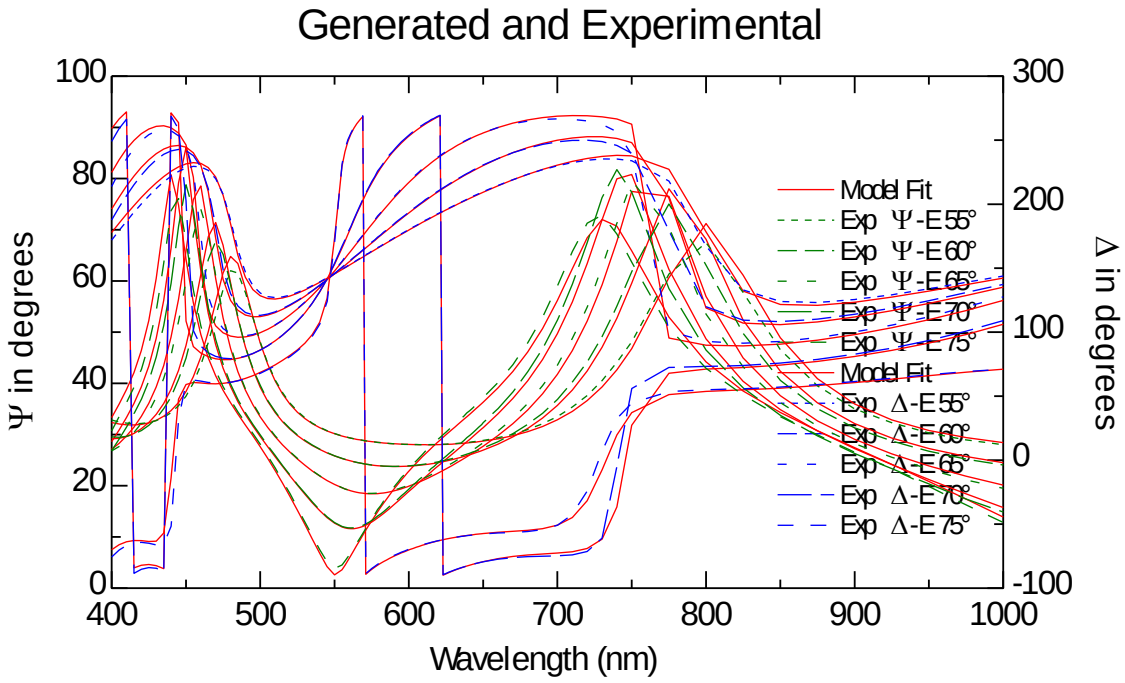

1 ema pche/1.03% cdse7cds_nk_extract	469.323 nm
0 si_jell	1 mm

MSE=15.77

Thick.1	469.323±0.415
EMA2.1	1.03±0.103

nm	n	k
400	1.5195844	0.00310514006
405	1.51959008	0.00303526452
410	1.51959795	0.00296711071
415	1.51961179	0.00289951917
420	1.51962991	0.00283149522
425	1.51965362	0.00275987783
430	1.51967964	0.00268383909
435	1.5197068	0.00260791334
440	1.51973638	0.00252629485
445	1.51976939	0.00244142978
450	1.51980627	0.00235318349
455	1.51984664	0.00225395729
460	1.51988547	0.00214306582
465	1.51992212	0.00202265609
470	1.5199559	0.00188969528
475	1.51998334	0.00173914012
480	1.51999299	0.0015659289
485	1.51997104	0.00137834326
490	1.51991564	0.00119462293
495	1.51982938	0.00102520897
500	1.51972095	0.00088178058
505	1.51959916	0.000772583217
510	1.51948061	0.000697615551
515	1.51937751	0.000647405702
520	1.51929325	0.000606223022
525	1.51922014	0.000560936155
530	1.51915068	0.000514729432
535	1.51908188	0.000467139235
540	1.51901083	0.000423499413
545	1.51894077	0.000384058807
550	1.51887023	0.0003466627
555	1.51879644	0.000313280887
557	1.51876593	0.000302799573
559	1.51873562	0.000294518062
561	1.51870523	0.000286674033

563	1.51867455	0.000281563178	629	1.51830936	0.000274349912
565	1.51864504	0.000280601102	631	1.51831423	0.000245506955
567	1.51861742	0.000281638259	633	1.51831449	0.0002140273
569	1.51859197	0.000284731187	635	1.51831014	0.000180386508
571	1.51856933	0.000289982399	637	1.51829725	0.000147269403
573	1.51854978	0.000295825859	639	1.51828056	0.000118453306
575	1.5185333	0.000301231322	641	1.51826085	9.2849919e-005
577	1.51851994	0.000307262887	643	1.51823747	7.01953036e-005
579	1.51851016	0.000309719038	645	1.51821292	5.37470942e-005
581	1.51850222	0.000309337185	647	1.51818791	4.11787984e-005
583	1.51849509	0.00030519535	649	1.51816382	3.18426882e-005
585	1.51848778	0.000297320245	650	1.51815197	2.7701365e-005
587	1.51847926	0.000285970926	660	1.51804847	1.17692135e-005
589	1.51846797	0.000270742384	670	1.51797011	9.59766535e-006
591	1.5184524	0.000254935279	680	1.51790515	8.52055083e-006
593	1.51843387	0.000240291731	690	1.51784899	8.69551881e-006
595	1.51841281	0.000227317495	700	1.51779884	8.88469808e-006
597	1.5183895	0.000216286593	710	1.51775315	8.83811357e-006
599	1.51836348	0.000207655918	720	1.5177121	9.26574828e-006
601	1.51833635	0.000205825749	730	1.5176747	8.74876135e-006
603	1.51831004	0.000209126062	740	1.51763953	8.55592607e-006
605	1.51828569	0.00021721608	750	1.51760487	8.25749299e-006
607	1.51826485	0.000230219402	775	1.51753213	1.05069721e-005
609	1.51824917	0.000245014725	800	1.51747326	7.98003254e-006
611	1.51823778	0.000261842796	825	1.51741372	3.21675278e-006
613	1.51823098	0.000279691873	850	1.51736343	2.06903633e-006
615	1.51822987	0.000296767203	875	1.5173192	2.41939636e-006
617	1.5182351	0.000310537931	900	1.51727859	1.17585042e-006
619	1.51824399	0.000320181253	925	1.51723798	9.64768226e-007
621	1.51825589	0.000325181128	950	1.51719716	7.52645763e-007
623	1.51827026	0.000322665033	975	1.51715636	5.39482615e-007
625	1.51828485	0.000313130309	1000	1.51711534	3.25278183e-007
627	1.51829825	0.000297377437			

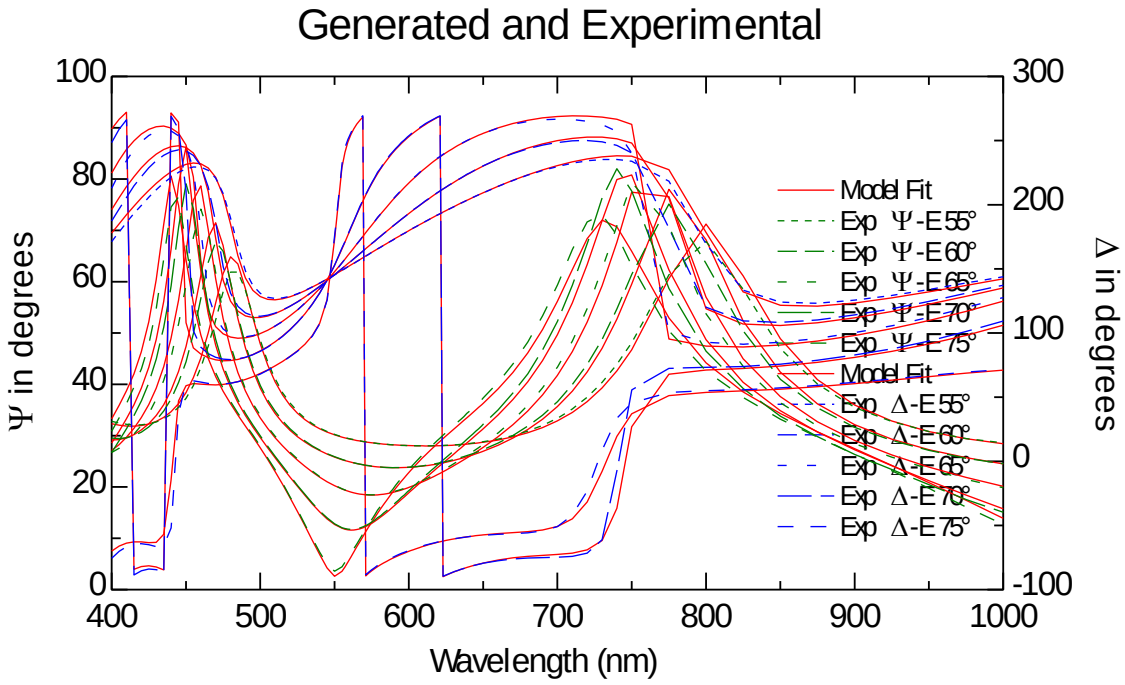

1 ema pche/1.05% cdse7cds_nk_extract469.273 nm	
0 si_jell	1 mm

MSE=16.12

Thick.1 469.273±0.415

EMA2.1 1.0535±0.104

nm	n	k
400	1.51978171	0.00317612704
405	1.51978752	0.00310465416
410	1.51979558	0.00303494242
415	1.51980974	0.00296580589
420	1.51982827	0.0028962271
425	1.51985253	0.0028229728
430	1.51987915	0.00274519608
435	1.51990693	0.00266753494
440	1.51993719	0.00258405092
445	1.51997097	0.00249724611
450	1.52000869	0.00240698279
455	1.52004999	0.00230548856
460	1.52008971	0.00219206228
465	1.5201272	0.00206890005
470	1.52016176	0.00193289971
475	1.52018982	0.00177890265
480	1.52019971	0.00160173133
485	1.52017725	0.00140985668
490	1.52012059	0.00122193556
495	1.52003236	0.00104864781
500	1.51992145	0.000901939774
505	1.51979688	0.000790245442
510	1.51967563	0.000713563474
515	1.51957017	0.000662205435
520	1.51948399	0.000620081041
525	1.51940921	0.000573758713
530	1.51933816	0.000526495548
535	1.51926779	0.000477817321
540	1.51919511	0.000433179798
545	1.51912346	0.00039283751
550	1.5190513	0.000354586482
555	1.51897583	0.000320441526
557	1.51894462	0.000309720591
559	1.51891362	0.000301249744
561	1.51888254	0.00029322638
563	1.51885115	0.000287998663
565	1.51882097	0.000287014553
567	1.51879272	0.000288075373
569	1.51876669	0.000291238954

571	1.51874354	0.000296610152	633	1.51848288	0.000218918752
573	1.51872354	0.000302587136	635	1.51847843	0.000184509118
575	1.51870668	0.000308116118	637	1.51846525	0.000150635134
577	1.51869302	0.000314285515	639	1.51844818	0.000121160456
579	1.51868301	0.000316797787	641	1.51842801	9.49719157e-005
581	1.51867489	0.000316407193	643	1.5184041	7.17995418e-005
583	1.51866759	0.000312170683	645	1.51837899	5.49754191e-005
585	1.51866012	0.000304115578	647	1.51835341	4.21198846e-005
587	1.5186514	0.000292506855	649	1.51832877	3.2570406e-005
589	1.51863986	0.000276930245	650	1.51831664	2.83344372e-005
591	1.51862393	0.000260761845	660	1.51821079	1.20381743e-005
593	1.51860498	0.000245783593	670	1.51813064	9.81699591e-006
595	1.51858344	0.000232512805	680	1.5180642	8.71526367e-006
597	1.5185596	0.000221229767	690	1.51800675	8.89422743e-006
599	1.51853298	0.000212401811	700	1.51795546	9.08772741e-006
601	1.51850523	0.000210529784	710	1.51790872	9.04007621e-006
603	1.51847833	0.000213905495	720	1.51786674	9.4774809e-006
605	1.51845342	0.000222180376	730	1.51782849	8.94867849e-006
607	1.5184321	0.000235480852	740	1.51779251	8.75143514e-006
609	1.51841607	0.000250614288	750	1.51775706	8.44618113e-006
611	1.51840442	0.000267826931	775	1.51768267	1.07470579e-005
613	1.51839746	0.000286083919	800	1.51762245	8.16237495e-006
615	1.51839632	0.000303549486	825	1.51756156	3.29025402e-006
617	1.51840167	0.000317634937	850	1.51751011	2.11631225e-006
619	1.51841077	0.000327498662	875	1.51746488	2.47467717e-006
621	1.51842293	0.000332612825	900	1.51742334	1.20271718e-006
623	1.51843763	0.000330039252	925	1.5173818	9.86811806e-007
625	1.51845256	0.000320286644	950	1.51734005	7.69842483e-007
627	1.51846627	0.000304173775	975	1.51729832	5.51808789e-007
629	1.51847764	0.00028061999	1000	1.51725636	3.32710113e-007
631	1.51848261	0.000251117854			

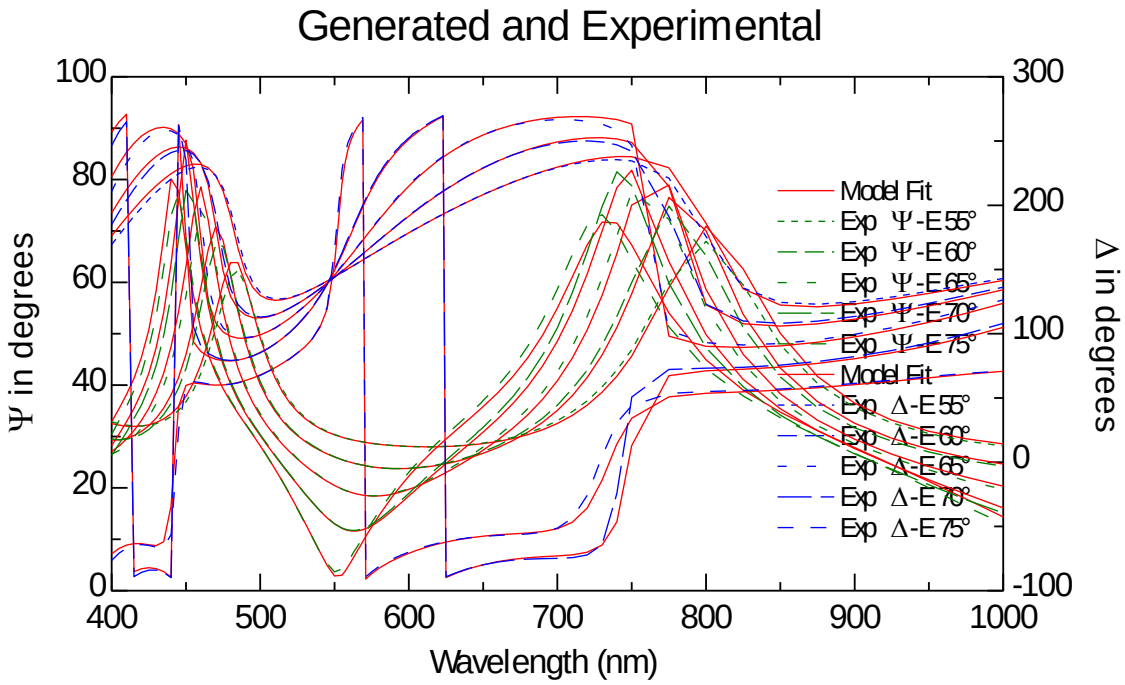

1	ema pche/0.787% cdse7cds_nk_extra	471.610 nm
0	si_jell	1 mm

MSE=16.57

Thick.1 471.610±0.383

EMA2.1 0.78651±0.0962

nm	n	k
400	1.5175405	0.00236999981
405	1.51754477	0.00231666648
410	1.51755073	0.00226464703
415	1.51756126	0.00221305607
420	1.51757505	0.00216113465
425	1.51759311	0.00210647001
430	1.51761294	0.00204843067
435	1.51763363	0.00199047762
440	1.51765617	0.00192817953
445	1.51768133	0.00186340337
450	1.51770944	0.00179604637
455	1.51774021	0.00172030903
460	1.51776981	0.00163566878
465	1.51779774	0.00154376439
470	1.51782349	0.00144228118
475	1.5178444	0.00132737022
480	1.51785175	0.00119516893
485	1.51783495	0.00105199856
490	1.51779263	0.00091177968
495	1.51772677	0.000782480446
500	1.51764399	0.000673014141
505	1.51755102	0.000589673767
510	1.51746052	0.000532458167
515	1.51738181	0.000494138047
520	1.51731749	0.000462707127
525	1.51726165	0.000428143071
530	1.51720861	0.000392876566
535	1.51715608	0.000356553818
540	1.51710183	0.000323246055
545	1.51704834	0.000293143183
550	1.51699448	0.000264600614
555	1.51693815	0.00023912191
557	1.51691486	0.000231122085
559	1.51689171	0.00022480131
561	1.51686851	0.000218814438
563	1.51684509	0.000214913749
565	1.51682256	0.00021417975
567	1.51680147	0.000214971723
569	1.51678204	0.000217332824

571	1.51676476	0.0002213413	633	1.51657012	0.000163367617
573	1.51674984	0.000225801806	635	1.51656679	0.000137689541
575	1.51673725	0.000229927964	637	1.51655695	0.000112411238
577	1.51672706	0.000234531989	639	1.5165442	9.0415894e-005
579	1.5167196	0.00023640688	641	1.51652915	7.08727996e-005
581	1.51671353	0.000236115515	643	1.51651131	5.35804881e-005
583	1.51670808	0.000232954163	645	1.51649257	4.10255276e-005
585	1.5167025	0.000226943222	647	1.51647347	3.14321033e-005
587	1.51669598	0.000218280438	649	1.51645509	2.43058081e-005
589	1.51668736	0.00020665668	650	1.51644604	2.11447127e-005
591	1.51667547	0.000194591339	660	1.51636701	8.98360167e-006
593	1.51666132	0.000183414145	670	1.51630717	7.32606027e-006
595	1.51664525	0.000173511137	680	1.51625759	6.50390337e-006
597	1.51662745	0.000165091473	690	1.51621469	6.63747996e-006
599	1.51660758	0.000158503906	700	1.51617641	6.78190301e-006
601	1.51658686	0.000157107167	710	1.5161415	6.74636054e-006
603	1.51656678	0.000159626529	720	1.51611017	7.07280084e-006
605	1.51654819	0.000165801881	730	1.51608162	6.67818396e-006
607	1.51653227	0.000175727566	740	1.51605475	6.53099954e-006
609	1.5165203	0.000187021066	750	1.51602829	6.30320825e-006
611	1.5165116	0.000199866146	775	1.51597274	8.02033894e-006
613	1.51650641	0.00021349053	800	1.51592777	6.09145699e-006
615	1.51650556	0.000226524249	825	1.5158823	2.45547545e-006
617	1.51650956	0.000237035464	850	1.51584388	1.57938207e-006
619	1.51651634	0.000244396151	875	1.51581012	1.84683094e-006
621	1.51652542	0.000248212425	900	1.51577908	8.97579954e-007
623	1.51653638	0.000246291684	925	1.51574809	7.36452955e-007
625	1.51654752	0.000239013597	950	1.5157169	5.74531164e-007
627	1.51655774	0.000226989202	975	1.51568575	4.11814257e-007
629	1.51656622	0.000209412089	1000	1.51565441	2.4830177e-007
631	1.51656992	0.000187396126			

Loading Fraction 30 mg/mL Film Pt1

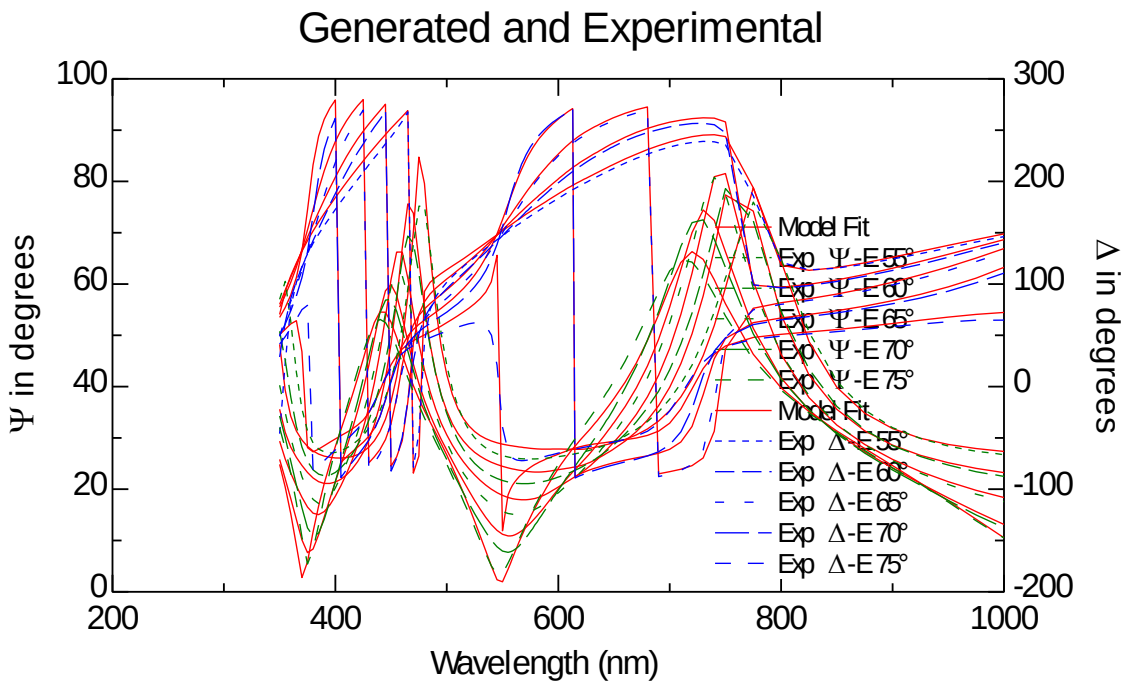

1 ema pche/10.9% cdse7cds_nk_extract	431.103 nm
0 si_jell	1 mm

MSE=47.35

Thick.1	431.103±0.844
EMA2.1	10.882±0.259

nm	n	k
350	1.60417511	0.0420820635
355	1.60383524	0.0410960571
360	1.60356459	0.0401555837
365	1.60334886	0.0392625717
370	1.60320258	0.0383967319
375	1.60307568	0.0375330746
380	1.60300636	0.0367035129
385	1.60296793	0.035887921
390	1.60295831	0.0350847919
395	1.6029768	0.0342852477
400	1.60301121	0.0334970892
405	1.60308048	0.0327440068
410	1.60317319	0.0320096507
415	1.60332952	0.0312818221
420	1.60353186	0.0305496204
425	1.60379474	0.0297790277
430	1.60408277	0.0289608063
435	1.60438289	0.0281437625
440	1.60470943	0.0272653374
445	1.60507315	0.0263519688
450	1.60547864	0.0254021969
455	1.60592233	0.024333929
460	1.60634999	0.0231393693
465	1.60675429	0.0218416281
470	1.607128	0.020407904
475	1.60743299	0.0187835354
480	1.60754646	0.0169133541
485	1.60731876	0.0148864788
490	1.60672871	0.0129003577

495	1.60580356	0.0110683305	613	1.58861211	0.00300664676
500	1.60463775	0.0095170475	615	1.58859995	0.00319019423
505	1.60332677	0.00833571567	617	1.58865611	0.00333827292
510	1.6020502	0.00752442993	619	1.58875162	0.00344201896
515	1.60093988	0.00698091342	621	1.58887954	0.00349587863
520	1.60003278	0.00653535107	623	1.58903428	0.00346896136
525	1.59924663	0.00604594411	625	1.58919151	0.00336658436
530	1.59849994	0.00554687445	627	1.58933593	0.00319733319
535	1.59775983	0.00503309527	629	1.58945585	0.00294983411
540	1.59699552	0.00456203441	631	1.58950858	0.00263974681
545	1.59624199	0.00413639202	633	1.58951186	0.00230127257
550	1.59548326	0.00373292146	635	1.58946553	0.00193953687
555	1.59468973	0.00337279357	637	1.58932732	0.00158340415
557	1.59436159	0.00325968504	639	1.58914824	0.00127352455
559	1.59403557	0.00317027611	641	1.58893647	0.000998203423
561	1.59370877	0.00308559	643	1.58868519	0.000754603392
563	1.59337884	0.0030303313	645	1.5884213	0.000577746761
565	1.59306153	0.00301973891	647	1.58815248	0.00044261642
567	1.59276451	0.00303067697	649	1.58789364	0.000342244105
569	1.59249084	0.00306375155	650	1.58776618	0.000297723995
571	1.59224736	0.00312006695	660	1.58665517	0.000126456707
573	1.59203694	0.00318277358	670	1.58581451	0.000103102872
575	1.59185956	0.00324078814	680	1.58511675	9.15163851e-005
577	1.59171585	0.00330556079	690	1.58451468	9.33819556e-005
579	1.59161061	0.00333189742	700	1.58397619	9.54010623e-005
581	1.59152529	0.00332771926	710	1.58348672	9.48895625e-005
583	1.59144882	0.0032831011	720	1.58304611	9.94701765e-005
585	1.59137055	0.00319832386	730	1.58264461	9.39110404e-005
587	1.59127915	0.00307616798	740	1.58226825	9.183273e-005
589	1.5911581	0.00291226876	750	1.58189625	8.86215935e-005
591	1.59099093	0.00274212488	775	1.58111686	0.000112742344
593	1.59079197	0.00258448962	800	1.58048635	8.56146394e-005
595	1.59056584	0.00244480709	825	1.5798488	3.4505975e-005
597	1.59031543	0.0023260257	850	1.57931047	2.21915917e-005
599	1.59003589	0.0022330543	875	1.57883617	2.59464423e-005
601	1.58974438	0.00221321427	900	1.57840177	1.26089104e-005
603	1.58946176	0.00224854544	925	1.57796637	1.03443473e-005
605	1.58920013	0.00233537962	950	1.57752985	8.06910346e-006
607	1.58897622	0.00247504716	975	1.57709243	5.78317877e-006
609	1.58880779	0.0026339997	1000	1.57665388	3.48657123e-006
611	1.58868534	0.00281482274			

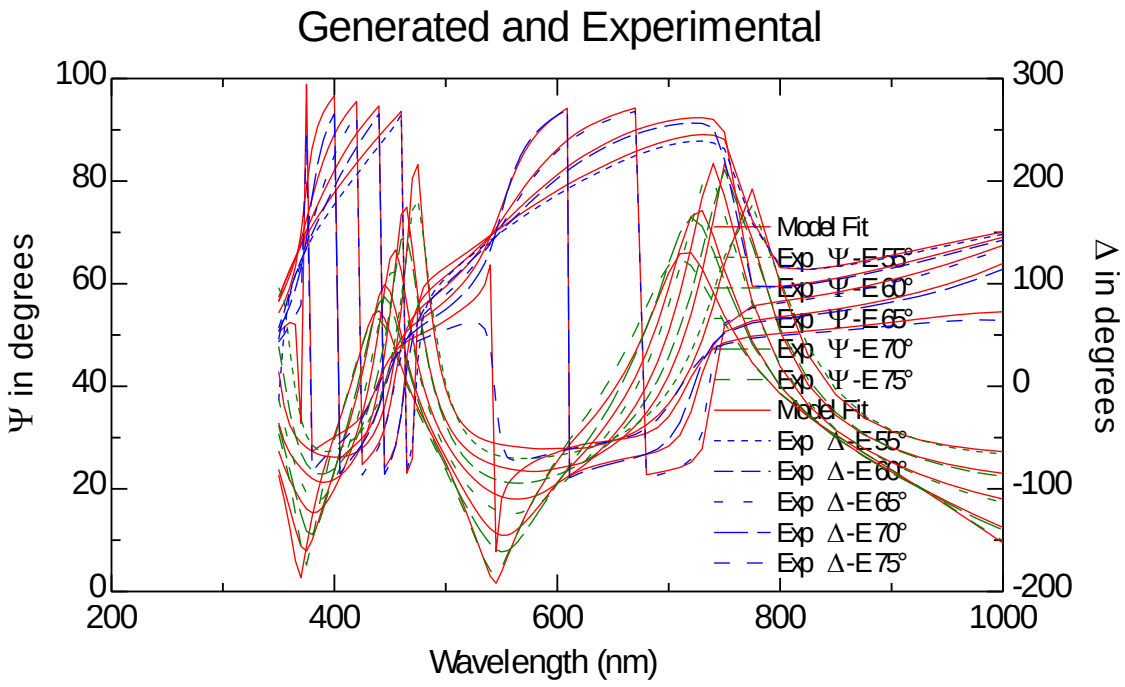

1 ema pche/10.8% cdse7cds_nk_extract428.005 nm	
0 si_jell	1 mm

MSE=46.19

Thick.1	428.005±0.786
EMA2.1	10.835±0.243

nm	n	k
350	1.60376886	0.0418956682
355	1.60343044	0.0409140465
360	1.60316093	0.0399777515
365	1.60294611	0.0390887041
370	1.60280043	0.0382267045
375	1.60267404	0.0373668765
380	1.60260498	0.0365409899
385	1.60256668	0.0357290096
390	1.60255706	0.0349294357
395	1.60257542	0.0341334295
400	1.60260964	0.0333487578
405	1.60267857	0.0325990057
410	1.60277083	0.0318678961
415	1.60292644	0.0311432825
420	1.60312785	0.0304143136
425	1.60338953	0.0296471215
430	1.60367625	0.0288325113
435	1.60397501	0.0280190738
440	1.60430007	0.0271445266
445	1.60466214	0.0262351903
450	1.60506579	0.0252896114
455	1.60550748	0.0242260616
460	1.6059332	0.0230367818
465	1.60633567	0.0217447802
470	1.60670768	0.0203174013
475	1.60701127	0.018700227
480	1.60712419	0.0168383367
485	1.60689745	0.0148204555
490	1.60630997	0.0128431535
495	1.60538889	0.0110192645
500	1.60422823	0.0094748741
505	1.60292304	0.0082987927
510	1.60165212	0.00749111418
515	1.60054671	0.00695001516
520	1.59964361	0.00650643329

525	1.59886094	0.00601919855	619	1.58841225	0.00342684241
530	1.59811754	0.00552234244	621	1.58853961	0.003480464
535	1.59738071	0.00501084076	623	1.58869367	0.00345366468
540	1.59661977	0.00454186763	625	1.58885021	0.0033517384
545	1.59586957	0.00411811117	627	1.58899399	0.00318323296
550	1.59511419	0.00371642769	629	1.58911338	0.00293682486
555	1.59432416	0.00335789472	631	1.58916587	0.00262810491
557	1.59399747	0.00324528732	633	1.58916914	0.0022911234
559	1.59367289	0.00315627473	635	1.58912301	0.00193098316
561	1.59334753	0.00307196403	637	1.58898541	0.00157642135
563	1.59301906	0.00301695074	639	1.58880712	0.00126790863
565	1.59270315	0.00300640644	641	1.58859628	0.000993801884
567	1.59240744	0.00301729745	643	1.58834611	0.000751276256
569	1.59213498	0.00305022717	645	1.58808338	0.000575199614
571	1.59189258	0.00310629502	647	1.58781574	0.000440665191
573	1.59168308	0.00316872579	649	1.58755805	0.000340735478
575	1.59150649	0.00322648508	650	1.58743116	0.000296411665
577	1.59136341	0.00329097251	660	1.58632504	0.000125899492
579	1.59125863	0.00331719339	670	1.58548808	0.000102648679
581	1.5911737	0.00331303406	680	1.58479339	9.11133194e-005
583	1.59109756	0.00326861316	690	1.58419398	9.29707486e-005
585	1.59101963	0.00318421037	700	1.58365785	9.4981033e-005
587	1.59092863	0.00306259392	710	1.58317054	9.44718471e-005
589	1.59080812	0.00289941841	720	1.58273187	9.90323551e-005
591	1.59064168	0.00273002591	730	1.58233214	9.3497738e-005
593	1.5904436	0.00257308688	740	1.58195743	9.142862e-005
595	1.59021847	0.00243402139	750	1.58158707	8.82316579e-005
597	1.58996917	0.00231576481	775	1.5808111	0.000112246393
599	1.58969086	0.00222320439	800	1.58018337	8.52380939e-005
601	1.58940063	0.00220345277	825	1.57954863	3.43542418e-005
603	1.58911926	0.00223862897	850	1.57901266	2.20940242e-005
605	1.58885878	0.00232508103	875	1.57854045	2.58323824e-005
607	1.58863586	0.00246413342	900	1.57810795	1.25534892e-005
609	1.58846818	0.00262238566	925	1.57767447	1.02988856e-005
611	1.58834627	0.00280241187	950	1.57723987	8.03364565e-006
613	1.58827336	0.00299339042	975	1.57680436	5.75776923e-006
615	1.58826126	0.00317612868	1000	1.57636774	3.47125428e-006
617	1.58831717	0.00332355424			

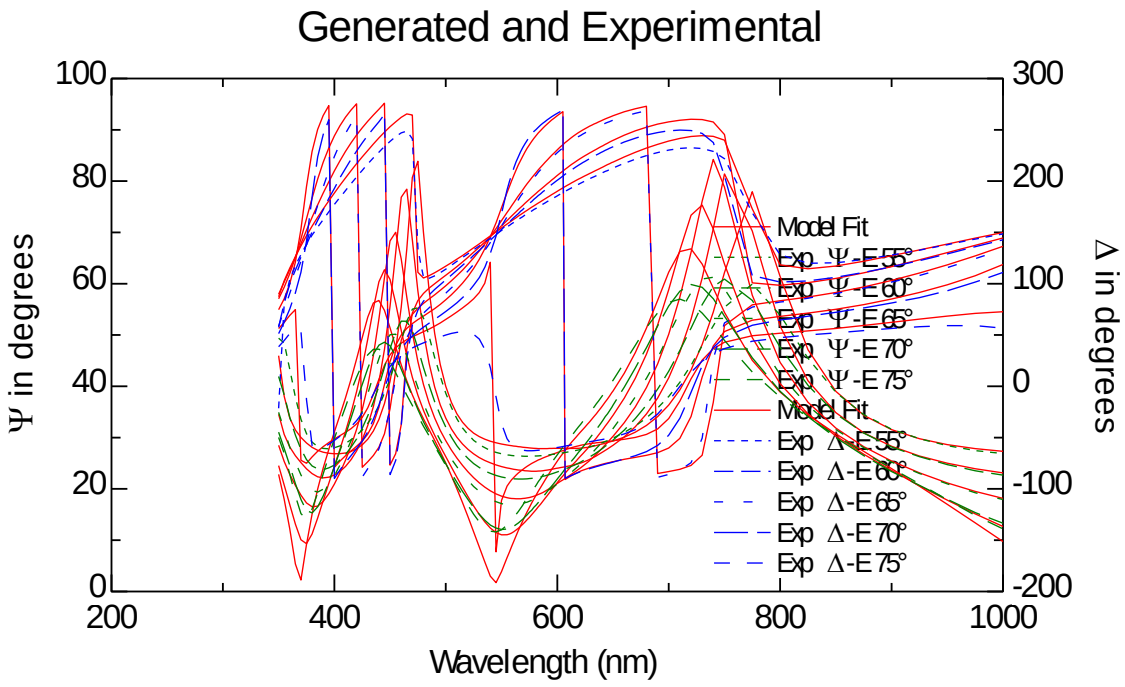

1 ema pche/9.67% cdse7cds_nk_extract431.909 nm	
0 si_jell	1 mm

MSE=59.71

Thick.1	431.909±1.5
EMA2.1	9.6688±0.449

nm	n	k
350	1.59369912	0.0372848686
355	1.59339663	0.036411657
360	1.59315555	0.0355786831
365	1.59296323	0.0347876811
370	1.5928325	0.0340206604
375	1.59271898	0.033255545
380	1.59265654	0.0325205685
385	1.59262152	0.0317979336
390	1.59261205	0.0310863096
395	1.59262752	0.0303778329
400	1.59265713	0.0296794307
405	1.59271769	0.0290120752
410	1.59279905	0.0283612935
415	1.59293681	0.0277162374
420	1.59311534	0.0270672703
425	1.5933475	0.0263842402
430	1.59360191	0.0256590013
435	1.59386706	0.0249348119
440	1.59415557	0.0241562331
445	1.59447701	0.0233466837
450	1.59483545	0.0225048713
455	1.59522766	0.0215580743
460	1.5956056	0.0204994371
465	1.59596282	0.0193494429
470	1.59629289	0.0180790399
475	1.59656203	0.0166398295
480	1.59666145	0.0149830039
485	1.59645867	0.0131875536
490	1.59593503	0.0114283356
495	1.59511471	0.00980568084
500	1.59408134	0.00843171956
505	1.59291949	0.00738545761
510	1.5917882	0.00666696475
515	1.59080426	0.00618563368
520	1.59000037	0.00579101952

525	1.58930364	0.00535750352	619	1.58000144	0.00305121122
530	1.58864186	0.00491539314	621	1.58011484	0.00309894192
535	1.58798591	0.0044602226	623	1.58025201	0.00307506443
540	1.5873085	0.00404288839	625	1.58039137	0.0029842959
545	1.58664065	0.00366578096	627	1.58051937	0.00283424956
550	1.58596818	0.00330830355	629	1.58062565	0.00261484507
555	1.58526485	0.00298922391	631	1.58067236	0.00233996754
557	1.58497401	0.00288901209	633	1.58067524	0.00203993136
559	1.58468506	0.00280980256	635	1.58063414	0.00171927845
561	1.5843954	0.00273477713	637	1.58051161	0.00140359571
563	1.58410296	0.00268583222	639	1.58035285	0.00112891246
565	1.58382173	0.0026764739	641	1.58016511	0.000884861271
567	1.58355847	0.00268619666	643	1.57994235	0.000668926908
569	1.5833159	0.00271553795	645	1.57970842	0.00051215498
571	1.5831001	0.00276547642	647	1.57947012	0.000392369681
573	1.5829136	0.00282107739	649	1.57924066	0.000303394556
575	1.58275638	0.00287251696	650	1.57912767	0.00026392927
577	1.58262901	0.00292994386	660	1.57814274	0.000112106868
579	1.58253573	0.0029532987	670	1.57739744	9.140578e-005
581	1.5824601	0.00294960411	680	1.57677884	8.11357283e-005
583	1.58239231	0.00291006351	690	1.57624505	8.27913917e-005
585	1.58232292	0.00283492668	700	1.57576762	8.45830631e-005
587	1.58224189	0.00272665897	710	1.57533364	8.41309667e-005
589	1.58213458	0.00258139257	720	1.57494298	8.8193551e-005
591	1.58198638	0.00243059366	730	1.574587	8.32657719e-005
593	1.58181001	0.00229088314	740	1.57425328	8.14240864e-005
595	1.58160956	0.00216708607	750	1.57392344	7.8577901e-005
597	1.58138758	0.00206181578	775	1.57323236	9.99676219e-005
599	1.58113978	0.00197942413	800	1.57267327	7.5915343e-005
601	1.58088138	0.00196185744	825	1.57210793	3.05974432e-005
603	1.58063085	0.00199319561	850	1.57163056	1.96782796e-005
605	1.58039894	0.00207018753	875	1.57120998	2.30082395e-005
607	1.58020046	0.00219401232	900	1.57082475	1.11812263e-005
609	1.58005116	0.0023349299	925	1.57043865	9.1732088e-006
611	1.57994263	0.00249523256	950	1.57005153	7.15566144e-006
613	1.57987773	0.00266528403	975	1.56966362	5.12858358e-006
615	1.57986697	0.00282799351	1000	1.5692747	3.09197296e-006
617	1.57991677	0.00295925429			